Department of Physics and Astronomy

University of Heidelberg

Master thesis

in Physics

submitted by

Nicolas ROTH

born in Tuttlingen

March, 2018

Visualization of Near-Surface Flow Patterns for Air-Water Gas Transfer

This Master thesis has been carried out by Nicolas ROTH

at the

Institute for Environmental Physics (IUP) &

Heidelberg Collaboratory for Image Processing (HCI)

under the supervision of

Prof. Dr. Bernd JÄHNE

Abstract

Near-surface flow patterns and their influence on local transport processes are investigated in a horizontal plane with visualization techniques. For this, a new method was developed that produces tracer particles with high effective Schmidt number ($Sc = \mathcal{O}(10^6)$) by chemical reaction directly at the water surface. While different chemical systems were tried, best results were achieved using the precipitate AgCl, formed by $AgNO_3$ in the water body and a controlled influx of HCl gas. Trace amounts of precipitate are made visible by scattering laser light. Using the new method, the influence of wind induced turbulences at the water interface can be investigated with previously unachieved sensitivity. Illumination of the wavy water surface leads to shadowing and lensing effects that become apparent in the image data and cannot fully be compensated for with image processing.

The results are qualitatively compared to data from active thermography (heat, $Pr \approx 7$) and boundary layer imaging (gas, $Sc \approx 600$), showing a close resemblance of the flow pattern. With higher Schmidt number of the tracer, the structure becomes more pronounced and higher sensitivity to surface convergence is observed. Experiments with glass spheres ($d = 70\,\mu\text{m-}2\,\text{mm}$, $Sc \to \infty$) were conducted for further comparison. Tracking of individual particles allows for a precise measurements of the surface velocity and investigations of the local momentum transfer.

Zusammenfassung

Strömungsmuster nahe der Wasseroberfläche und ihre Auswirkungen auf lokale Transportprozesse werden mit Visualisierungsmethoden in horizontaler Ebene untersucht. Dafür wurde eine neue Technik entwickelt, die Tracerpartikel mit hoher effektiver Schmidtzahl ($Sc = \mathcal{O}(10^6)$) direkt an der Wasseroberfläche durch chemische Reaktionen erzeugt. Unter verschiedenen getesteten chemischen Systemen ist eine Ausfällung von AgCl, erreicht durch in Wasser gelöstes $AgNO_3$ und kontrollierte Einfuhr von HCl in den Luftraum, am besten geeignet. Bereits geringe Teilchenkonzentrationen können durch die Streuung von Laserlicht sichtbar gemacht werden. Mit der neuen Methode kann der Einfluss von windinduzierten Turbulenzen an der Oberfläche mit bisher unerreichter Empfindlichkeit nachgewiesen und untersucht werden. Für höhere Windbedingungen führen Abschattungen und Reflektionen der Beleuchtung an der Wasseroberfläche zu Störungen, welche auch mit aufwändigen Bildverarbeitungsmethoden nicht hinreichend behoben werden können.

Die Resultate werden qualitativ mit Daten aus der Thermographie (Wärme, $Pr \approx 7$) sowie der Grenzschichtdickenvisualisierung (Gas, $Sc \approx 600$) verglichen, wobei eine starke Ähnlichkeit der Strömungsmuster beobachtet wird. Mit ansteigender Schmidtzahl der Tracer wird eine klarere Struktur und größere Empfindlichkeit für Oberflächenkonvergenz beobachtet. Zum weiteren Vergleich wurden Experimente mit Glaskugeln ($d = 70\,\mu\text{m-}2\,\text{mm}$, $Sc \to \infty$) durchgeführt. Tracking der einzelnen Partikel erlaubt eine präzise Bestimmung der Oberflächengeschwindigkeit und eine Vermessung des lokalen Impulstransfers.

Contents

Chapter 1

Introduction

Visualization and imaging techniques are of outstanding importance for the investigations of spatially and temporally variable structures. With the rise of powerful computers and digital image sensors, large amounts of data can be recorded and analysed with ever-growing sensitivity and precision. This makes the analysis of digital image data to a key technology for further scientific progress. Image processing at the University of Heidelberg started with the investigation of wave dynamics for air-water exchange processes. Figure [1.1] is an example for the gain of information associated with this technique. Other research areas followed to benefit from the manifold opportunities of quantitative image analysis to study dynamic processes and successfully established it in applications from the movement of motor proteins up to global gas emissions. The development of new methods and further research in image processing has therefore high potential to find applications in other fields. An in many ways challenging problem for image analysis remains to be the transfer processes between ocean and atmosphere.

The exchange of climate active gases is hereby of special interest for research as well as for politics and the society. Over the years 2007-2016, the oceans were a sink for $(2.4 \pm 0.5)\mathrm{Gt/yr}$ of CO_2, corresponding to a quarter of anthropogenic emissions (Le Quéré et al., 2017). The *Fifth Assessment Report of the IPCC* shows that the oceans' heat uptake of accounts for ca. 93% of the increase in the earths energy inventory for 1971-2010 (Rhein et al., 2013). This shows that a profound theory of the exchange mechanisms between ocean and atmosphere is necessary for understanding and modelling the earth climate. The influence of various parameters makes meaningful measurement on the ocean extremely difficult (compare e.g. Garbe et al., 2014).

Laboratory studies try to split up these complex dependencies and determine

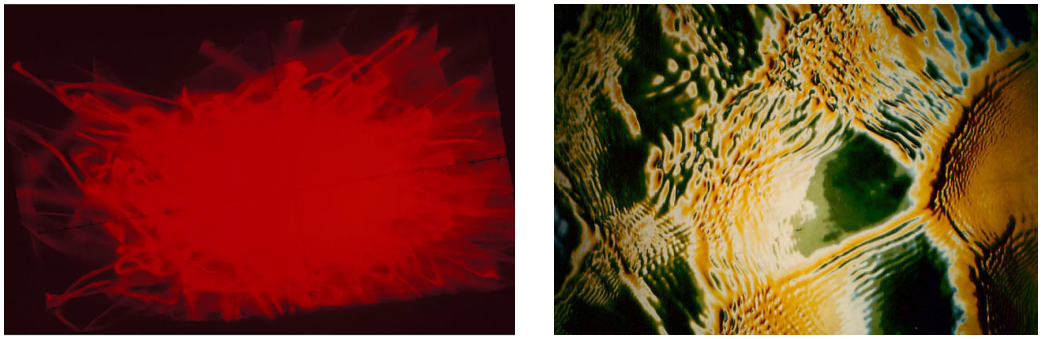

FIGURE 1.1: Comparison of different measurement techniques for slopes of water waves; *left*: optical point measurement of the diffraction pattern of a laser beam (cf. Jähne, 1983b) and *right*: imaging of the water surface (Jähne, 1986)

the effect of isolated factors. In this way, the transfer process is parametrized and exchange constants can be determined. Within the last years, many imaging techniques were developed, providing further insights into small-scale air-sea interaction. One important focus was on the high-speed measurement of slope and height of short wind waves (Huhn, 2008; Kiefhaber et al., 2014; Rocholz et al., 2011). Special emphasis was also on the realization and improvement of tools to measure the concentration of gas within the top layer, around 100 µm thick, of the moving water surface. The boundary layer visualization technique called laser-induced fluorescence (LIF), established by Münsterer and Jähne (1998), measures the vertical concentration profile via chemical reactions in water by observing from the side. The fluorescence can be induced by dyes that are either sensitive to a change in pH-value (Herzog, 2010) or quenching effects (Friedl, 2013) due to a tracer gas. Other developed LIF-based techniques use different optical setups or measure in the air-sided boundary layer (Krah, 2014; Trofimova, 2015). Conceptual disadvantages of the LIF method in general, are the movement of the water surface (up and down with waves) and the need for very high spatial resolutions to actually visualize the gradient in the thin boundary layer. Jähne (1986, 1983a, 1985) already proposed methods to make the horizontal concentration field of gases visible from aerial view. Yet it took almost 30 years until Kräuter et al. (2014) overcame the experimental difficulties and developed a fluorescence technique to visualize the thickness of the mass boundary layer for surface patches. With this boundary layer imaging technique (BLI), flow patterns and wave breaking events are made visible and their influence on mechanisms of air-sea gas transfer can be studied directly. Unfortunately, susceptible pH-value settings make this method experimentally demanding and it could not yet be applied outside Heidelberg's wind-wave facilities.

Alternative approaches use camera imaging of flow tracers (e.g. Banner and Peirson, 1998; Rashidi and Banerjee, 1990; Turney and Banerjee, 2013) and temperature patterns near the air-water interface (e.g. Jessup et al., 1997; Schimpf, Garbe, and Jähne, 2004; Schnieders et al., 2013). These measurements showed how important it is to investigate the turbulent near-surface flow patterns and already contributed a lot to our understanding of the underlying processes. Especially thermography, the optical investigation of heat transfer, has been proven to be a powerful tool that can even be applied in field measurements (Nagel, 2014; Schimpf, Nagel, and Jähne, 2011). This provides an important link and indicates to what extend laboratory experiments match the actual conditions on the ocean.

How well the implications and findings between the results of thermography and BLI translate, and what that means for the relation of the two tracer-species gas and momentum, is still an open research question. The crucial difference between the methods is the diffusivity of the tracer. The main objective of this work is to develop a new visualization method that extends this comparison.

Chapter 2

Theory

Investigations of gas transfer at the water surface are under the influence of multifarious processes. The aim of this chapter is to provide an understandable mathematical background for the natural phenomenons and laboratory observations investigated in this thesis. Basic quantities and conceptual models for the description of air-sea gas transfer are introduced. Special emphasis is on the importance of the Schmidt number as well as the relevance and interpretation of chemical reactions at the interface. To conclude, an overview is given on the turbulent flow patterns at the water surface that are crucial for transport mechanisms and are closely investigated within this work.

2.1 Transport at the Air-Water Interface

Basic transport processes are introduced and it is shown that the transport of momentum, which introduces turbulence into the water body, is inextricably linked with the transport of mass (i.e. gas) and heat. For simplification, the water surface is set in the x-y-plane with the main flow direction x. Hence, u is the stream-wise and w the vertical component of the velocity field $\vec{u} = (u, v, w)$. Flux densities $\vec{j}$ are assumed to be constant across the surface.

2.1.1 Molecular and Turbulent Transfer Mechanisms

Molecular and turbulent diffusion are the two major transport mechanisms by which exchange processes at the water surface are governed. The former process is caused by the random, undirected motion of particles as a consequence of their thermal energy. The velocity in this stochastic process follows the Boltzmann distribution and the motion is described by the random walk model (Pearson, 1905). The other decisive process is turbulent flow, characterized by chaotic changes in flow velocity which is described by Kolmogorov (1941, 1962). Since the length scales of turbulent eddies are typically much larger than the mean free path of the particles, this is the dominant mixing process. These eddies cannot penetrate the air-water interface due to the discontinuity in density, and therefore their size is limited to the distance to the surface. Consequently, turbulent mixing becomes more and more ineffective for smaller depths (compare Prandtl, 1957). The region, where molecular transport is the dominant mechanism is called the boundary layer.

These considerations hold regardless of the transported quantity. Therefore, the flux of mass, heat, as well as momentum can all be described within the same conceptual framework. Whereas a more detailed analysis is provided later in this chapter, their transport in the upper most layer consequently follows Fick's first law (Fick,

1855; Jähne and Haussecker, 1998):

$$\text{Gas:} \quad \vec{j_c} = D\nabla c \tag{2.1}$$

$$\text{Heat:} \quad \vec{j_h} = D_h\nabla(\rho c_p T) \tag{2.2}$$

$$\text{Momentum:} \quad \vec{j_m} = \nu\nabla(\rho u) \equiv \tau \tag{2.3}$$

where $\vec{j}$ denotes the flux densities, τ is the shear stress at the interface; c is the gas concentration, c_p the specific heat at constant pressure with temperature T, ρ the density of the medium; D is the diffusion coefficient and D_h, ν its analogues for heat and momentum. Given that, the dimensionless **Schmidt number** is defined for characterization of fluid flows as the ratio of kinematic viscosity and mass diffusivity:

$$Sc = \frac{\nu}{D}. \tag{2.4}$$

Heat flow is described in terms of the equivalent **Prandtl number**:

$$Pr = \frac{\nu}{D_h}. \tag{2.5}$$

While Prandtl and Schmidt number in the air are typically close to one, they differ by about two orders of magnitude in water (detailed discussion in section 2.3).

Under the consideration of advective transport in the velocity field $\vec{u} = (u, v, w)$, the change of concentration with time is predicted by Fick's second law:

$$\frac{\partial c}{\partial t} + \vec{u} \cdot \nabla c = D\Delta c. \tag{2.6}$$

Again, an analogue description can be found for momentum transport by considering the **Navier-Stokes equation** for incompressible fluids:

$$\frac{\partial \vec{u}}{\partial t} + (\vec{u} \cdot \nabla)\vec{u} = -\frac{1}{\rho}\nabla p + \nu\Delta\vec{u} + \vec{f}. \tag{2.7}$$

Assuming no external accelerations $\vec{f}$ and no pressure gradient ∇p, this reduces to:

$$\frac{\partial \vec{u}}{\partial t} + (\vec{u} \cdot \nabla)\vec{u} = \nu\Delta\vec{u}. \tag{2.8}$$

By applying the **Reynolds decomposition** of a quantity x to separate the expectation value $\bar{x}$ from its fluctuation x', a consistent notation for both diffusive transport mechanisms can be found. Following the derivation in Pope (2009), the transport equations (2.6) and (2.8) yield the differential equations:

$$\frac{\partial \bar{\xi}}{\partial t} = \frac{\partial}{\partial z}\left(D\frac{\partial \bar{\xi}}{\partial z} - \overline{\xi' w'}\right) \quad \text{with } \xi \in \{c, u\}. \tag{2.9}$$

Integrating these equations and combining them with the continuity equation leads to constant flux densities:

$$j_c = -D\frac{\partial \bar{c}}{\partial z} + \overline{c'w'} \tag{2.10}$$

$$j_m = \left(-\nu\frac{\partial \bar{u}}{\partial z} + \overline{u'w'}\right) \cdot \rho. \tag{2.11}$$

By comparing these results with equations (2.1) and (2.3), it seems natural to define turbulent equivalents to diffusivity K_c and viscosity K_m:

$$K_c := -\overline{c'w'} \Big/ \frac{\partial \overline{c}}{\partial z} \tag{2.12}$$

$$K_m := -\overline{u'w'} \Big/ \frac{\partial \overline{u}}{\partial z}. \tag{2.13}$$

Thereby, the equations for the density fluxes can be rewritten to:

$$j_c = -\left(D + K_c(z)\right) \frac{\partial \overline{c}}{\partial z} \tag{2.14}$$

$$j_m = -\left(\nu + K_m(z)\right) \frac{\partial \overline{u}}{\partial z} \cdot \rho. \tag{2.15}$$

These definitions consequently give rise to the turbulent Schmidt number:

$$Sc_t = \frac{K_m}{K_c}. \tag{2.16}$$

2.1.2 Parametrization of the Transport Process

To introduce suitable parameters for quantifying the transport mechanism, (2.10) can be integrated to obtain:

$$\int_{z_1}^{z_2} \frac{\partial \overline{c}}{\partial z}\, dz = -\int_{z_1}^{z_2} \frac{j_c}{K_c(z) + D}\, dz \tag{2.17}$$

$$\Rightarrow R_{2,1} := \frac{c(z_2) - c(z_1)}{-j_c} = \int_{z_1}^{z_2} \frac{1}{K_c(z) + D}\, dz. \tag{2.18}$$

This quantity R gives a measure for renitency at the air-water interface to gas transfer and is therefore called the **transfer resistance**. Most commonly, its inverse value, the **transfer velocity** k is used:

$$k_{2,1} := \frac{1}{R_{2,1}} = \frac{-j_c}{c(z_2) - c(z_1)}, \quad k \equiv \frac{j}{\Delta c}. \tag{2.19}$$

It is important to note that this concept of a transfer velocity is universally applicable, not just to the transport of gas through the surface but also to heat and momentum. In these cases the foregoing concentration difference there corresponds to a difference in thermal energy or momentum.

Analogous to the electrical resistance, the total resistance for gas transfer is the sum of its parts of multiple levels:

$$R_{3,1} = \frac{(c(z_3) - c(z_2)) + (c(z_2) - c(z_1))}{-j_c} = R_{3,2} + R_{2,1}. \tag{2.20}$$

Accordingly, transfer velocities add up reciprocally, so that the smallest rate determines the overall effectiveness of the process. For most gases, this bottleneck lies in the aqueous **boundary layer**.

By extrapolating the linear approximation for the concentration profile at the water surface, where no turbulent mixing occurs, one obtains a length scale z_* that

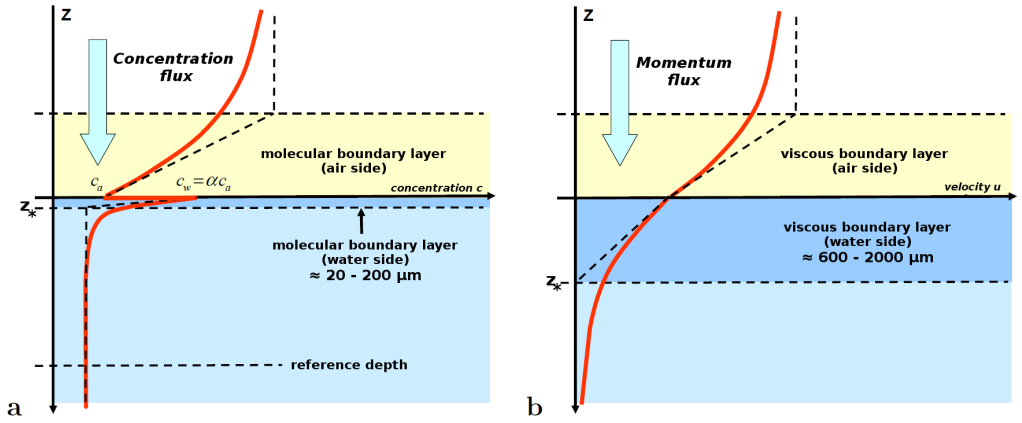

FIGURE 2.1: Schematic illustration of molecular and viscous boundary layer at the water surface (modified after Degreif, 2006). **a** Concentration profile; discontinuity at the interface due to solubility α **b** Velocity profile; u is continuous at the surface, meaning that momentum is discontinuous due to $\rho_w \ll \rho_a$.

is defined as the boundary layer thickness:

$$z_* := \Delta c \Big/ \frac{\partial \bar{c}}{\partial z}\Big|_{z=0} = \frac{D\Delta c}{j} = \frac{D}{k}. \tag{2.21}$$

The thickness of the viscous boundary layer is defined analogously as seen in figure [2.1]. Directly at the interface, the concentration of a tracer follows **Henry's Law**,

$$c_w = \alpha c_a, \tag{2.22}$$

with the tracer specific solubility constant α. This is equivalent to the no-slip condition for momentum transfer at the surface which results in a smooth velocity gradient. There, an analogous quantity for the solubility of momentum can be formulated:

$$\alpha_m = \frac{\rho_w}{\rho_a} = 828.9. \tag{2.23}$$

for $T = 20\,^{\circ}\mathrm{C}$ and $p = 1\,\mathrm{bar}$ (Haynes, 2016).

2.1.3 Wind and Shear Stress

Experiments by Peirson (1997) and numerical studies by Tsai, Chen, and Moeng (2005) are in agreement that wind stress does - not directly, but through production of small-scaled turbulences - control the transport processes.
Figure [2.1] and the equations (2.14) and (2.15) illustrate the already discussed analogy between gas and momentum transfer. The momentum flux is by definition equal to the surface shear stress in the water $\tau := j_m$. This tangential forcing forms shear layers with vertical momentum transport towards the water-body. As a measure for turbulent momentum transport at the air-water interface, the so called **friction velocity** (since it has the dimensions $[\frac{m}{s}]$) is introduced:

$$u_* = \sqrt{\frac{|\,\tau\,|}{\rho}}, \quad \text{with } u_* \equiv u_{*w} = \sqrt{\frac{\rho_a}{\rho_w}}\,u_{*a}, \tag{2.24}$$

where $u_{*\{a,w\}}$ corresponds to the air and water side, respectively. In the turbulent regime, this formulation is equivalent to:

$$u_* = \sqrt{\overline{u'w'}}. \tag{2.25}$$

As already discussed for the water side, the viscosity term in (2.15) gets negligible for greater distance to the surface. The wind profile is therefore only dependent on z and a measure for turbulence. With that, dimensional analysis leads to:

$$\frac{du}{dz} = C\frac{u_*}{z} \tag{2.26}$$

$$\overset{\text{int.}}{\Rightarrow} \quad u(z) = \frac{u_*}{\kappa}\ln(\frac{z}{z_0}), \tag{2.27}$$

where the reference hight z_0 is called the roughness length, correction for surface properties, and $C^{-1} \equiv \kappa \approx 0.41$ is the *von Kármán constant*. This well known **logarithmic wind profile** (for details see e.g. Roedel, 2000) can be verified in linear wind-wave facilities. A popular choice as a reference wind speed is $u(z = 10\text{m}) := u_{10}$. For annular channels like the *Aeolotron* (description in section 4.1.3) however, drifting effects interfere and the logarithmic profile does not build up. To have an alignment of measurement conditions, one has to compare the friction velocities u_*.

The wind induced shear stress leads to a difference between the velocity in the water bulk u_b and directly at the air-water interface u_{surf}. This is described by the introduction of a dimensionless scaling factor β that can be interpreted as momentum resistance in the water. Following equation (2.24), the shear stress can thus be expressed as:

$$\tau = \rho_w u_*^2 = \rho_w \left(\frac{\Delta u}{\beta}\right)^2. \tag{2.28}$$

Under the assumption of a constant β and the system being in equilibrium, this can be used to predict the surface velocity in a wind-wave tunnel. Equilibrium in this case means that the same amount of momentum that is transferred to the water by the wind is dissipated due to friction at the walls:

$$A_{surf} \cdot \tau_{surf} = A_{wall} \cdot \tau_{wall} \tag{2.29}$$

$$A_{surf} \cdot \rho_w \left(\frac{u_{surf} - u_b}{\beta}\right)^2 = A_{wall} \cdot \rho_w \left(\frac{u_b - 0}{\beta}\right)^2 \tag{2.30}$$

$$\Rightarrow \quad u_{surf} = u_b \left(1 + \sqrt{\frac{A_{wall}}{A_{surf}}}\right). \tag{2.31}$$

With the assumption that the momentum transfer at the interface is of the same nature as at the wall β cancels out. The velocity at the wall is set to zero according to the no slip condition. Hence, the surface velocity is only dependent on the bulk velocity and the ratio between the area of the water surface A_{surf} to the combined area of the walls A_{wall}. The subtractive solution of the quadratic equation is physically not meaningful.

2.2 Gas Exchange Models

Conceptual models for the transport processes at the air-water interface provide an intuitive understanding of the underlying principles. In this section, semi-empirical models of turbulent gas exchange are presented and discussed. Thereby will be assumed that the dominant transfer resistance lies on the water-side of the interface.

2.2.1 Film Model

As the simplest case, Whitman (1923) divided the water body in two zones. Below the boundary layer at $z = z_*$, the water is well mixed by turbulence, the zone above is purely governed by molecular diffusion. This assumption of an immediate switch of regimes is clearly oversimplified, it is however still useful for approximations. Since it ignores the contribution of small eddies to the mixing in the boundary layer, it provides a lower limit for the transfer velocity. Integration of equation (2.18) for $K_c(z < z_*) = 0$ leads to an inversely proportional relationship of transfer velocity and Schmidt number:

$$k = \frac{D}{z_*} \quad \Rightarrow \quad k \propto Sc^{-1}. \tag{2.32}$$

2.2.2 Diffusion Model

Following the idea proposed in section 2.1.1, Deacon (1977) assumed a continuously decreasing eddy size towards the water surface with $K(z = 0) = 0$. He proposed a behaviour of K based on the velocity profile by Reichardt (1951) for a smooth water surface (for simplicity, assume $Sc_t \equiv 1$):

$$K(z) = Sc\, D\kappa z_l \left(\frac{z_+}{z_l} - \tanh \frac{z_+}{z_l} \right), \tag{2.33}$$

with the von Kármán constant κ, the dimensionless thickness of a smooth wall $z_+ = \frac{u_* z}{\nu}$, and a constant dimensionless depth $z_l \equiv 11.7$ (determined so that (2.33) is in accordance with a logarithmic velocity profile). With that, the integral for the transfer resistance of equation (2.18) can be approximated numerically. Integration from the surface until a reference depth $z_r \equiv 50\frac{\nu}{u_*}$ yields:

$$R = \int_0^{50\frac{\nu}{u_*}} \frac{dz}{K(z) + D} = \frac{Sc}{u_*} \int_0^{50} \frac{dz_+}{1 + \frac{K(z)}{D}}. \tag{2.34}$$

For small Schmidt numbers and therefore air-sided control (in greater detail in section 2.3), this leads to a dimensionless transfer resistance ($R_+ = u_* \cdot R$) of:

$$R_{+,a} = 15.2\, Sc^{0.61} \quad \text{for: } 0.6 < Sc < 10. \tag{2.35}$$

For water-sided control, i.e. higher Schmidt numbers the result reads:

$$R_{+,w} = 12.1\, Sc^{2/3} + 2.7 \log_{10}(Sc) + 2.90 \quad \text{for: } Sc > 10 \tag{2.36}$$

$$\Rightarrow \quad k_+ := \frac{k}{u*} \approx \frac{1}{12.1}\, Sc^{-2/3} \quad \text{for: } Sc > 100. \tag{2.37}$$

Thus, the transfer velocity of heat (with a Prandtl or Schmidt number of 7 at 20°C,) is in a different regime than most gases.
This model is in good agreement with empirical measurements for low wind speeds.

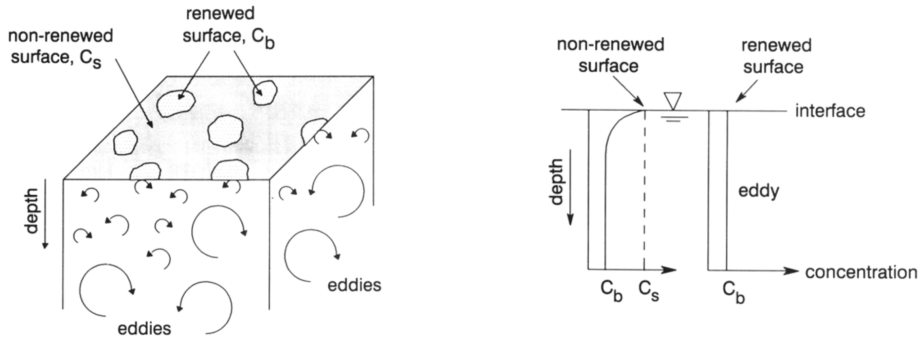

FIGURE 2.2: Drawing of the surface renewal and concentration profiles before and after a surface renewal event (from Asher and Pankow, 1991)

For higher values, the assumption of a smooth surface is not valid anymore and the model systematically underestimates measured values.

2.2.3 Surface Renewal Model

In the surface renewal model, first proposed by Higbie (1935), gas transport is assumed to be a mainly statistical process. With some probability, turbulent eddies reach into the boundary layer and transport the surface concentration c_s into the bulk (c_b). While it was first assumed, that the renewal rate is periodic, Harriott (1962) proposed it to be a random process. Jähne (1985) generalized this by also allowing for a dependence to the depth z to obtain a renewal rate $\lambda = \gamma_p z^p$ with the exponent $p \in \{0, 1\}$ and the associated constant of proportionality γ_p. In this model, that expression is responsible for turbulent transport. Inserting it in the averaged turbulent transport equation leads to:

$$0 = \frac{\partial \overline{c}}{\partial t} \overset{(2.9)}{=} D\frac{\partial^2 \overline{c}}{\partial z^2} + \frac{\partial}{\partial z}\overline{c'w'} \tag{2.38}$$

$$0 = D\frac{\partial^2 \overline{c}}{\partial z^2} - \lambda c. \tag{2.39}$$

Solving this differential equation for the depth independent case of $p = 0$ leads to

$$c(z) = c_b + (c_s - c_b)\exp\left(-\frac{z}{z_*}\right), \tag{2.40}$$

with the effective thickness $z_* = \sqrt{\frac{D}{\lambda}}$. Directly at the surface, only molecular diffusion contributes to the transport velocity $k = \sqrt{\lambda D}$. Dimensional analysis shows $[\lambda] = \frac{1}{\mathrm{s}} = [\frac{u_*^2}{\nu}]$ and by introducing the dimensionless scaling factor β (as described in section 2.1.3), one obtains:

$$k = \frac{u_*}{\beta} Sc^{-1/2}. \tag{2.41}$$

This relation however only holds for $p = 0$ which is equivalent to a free (or wavy) water surface. The general relation for p is given by Jähne et al. (1989) to be:

$$k = \frac{u_*}{\beta_p} Sc^{-\frac{p+1}{p+2}}. \tag{2.42}$$

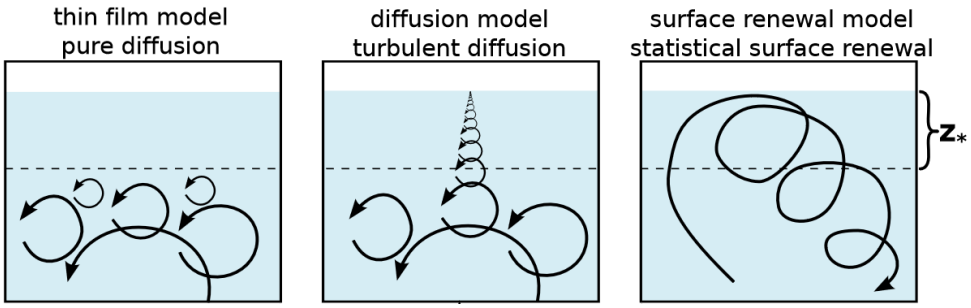

FIGURE 2.3: Schematic illustration of the discussed models (modified after Schimpf, 2000)

The other important case of a smooth water surface is described by $p = 1$ and therefore results in a Schmidt number dependency of $k \propto Sc^{-2/3}$.

One of the motivations for developing a new visualization method for gas transfer was to directly capture these renewal events on the air-water interface. It was presumed that evenly distributed particles on the surface should show areas of renewed surface as illustrated in figure [2.2].

2.2.4 Summary and Facet Model

As an overview, figure [2.3] provides an intuitive image of the models discussed so far. Their predictions for the concentration profile in the boundary layer vary with the different assumptions and can be investigated with laser induced fluorescence (LIF) techniques as for instance by Münsterer, Mayer, and Jähne (1995).

For the transfer velocity, though, they all lead to the following general form:

$$k_{bc} = \frac{u_*}{\beta_{bc}} Sc^{-n_{bc}}, \tag{2.43}$$

where the subscript $bc \in \{w, s\}$ indicates the dependency on boundary conditions (wavy or smooth) and the Schmidt number exponent n is introduced. Consequently, under the same boundary conditions two tracers (A&B) can be - independently from the assumed model - compared by Schmidt number scaling:

$$\frac{k_A}{k_B} = \left(\frac{Sc_A}{Sc_B}\right)^{-n} \quad \Rightarrow \quad n = -\frac{\ln(\frac{k_A}{k_B})}{\ln(\frac{Sc_A}{Sc_B})}. \tag{2.44}$$

As already stated in section 2.2.3, $n = 1/2$ corresponds here to a wavy, and $n = 2/3$ to a smooth water surface. This allows to measure the transition from the air-water interface from a rigid wall to a free surface. With known Schmidt numbers, the transfer velocities of two tracers can be measured simultaneously to directly obtain n. The binary classification of the water surface as rigid wall on the one hand and free interface on the other is however not an accurate description of the reality. In fact, the transition from a smooth to a wavy surface is gradual (compare Jähne et al., 1987) and the wavy fraction is denoted as $a_w \in [0, 1]$ with $a_w + a_s = 1$. Combining these two states of changing boundary conditions in a closed form reads:

$$k = (1 - a_w)\frac{u_*}{\beta_s} Sc^{-n_s} + a_w \frac{u_*}{\beta_w} Sc^{-n_w}. \tag{2.45}$$

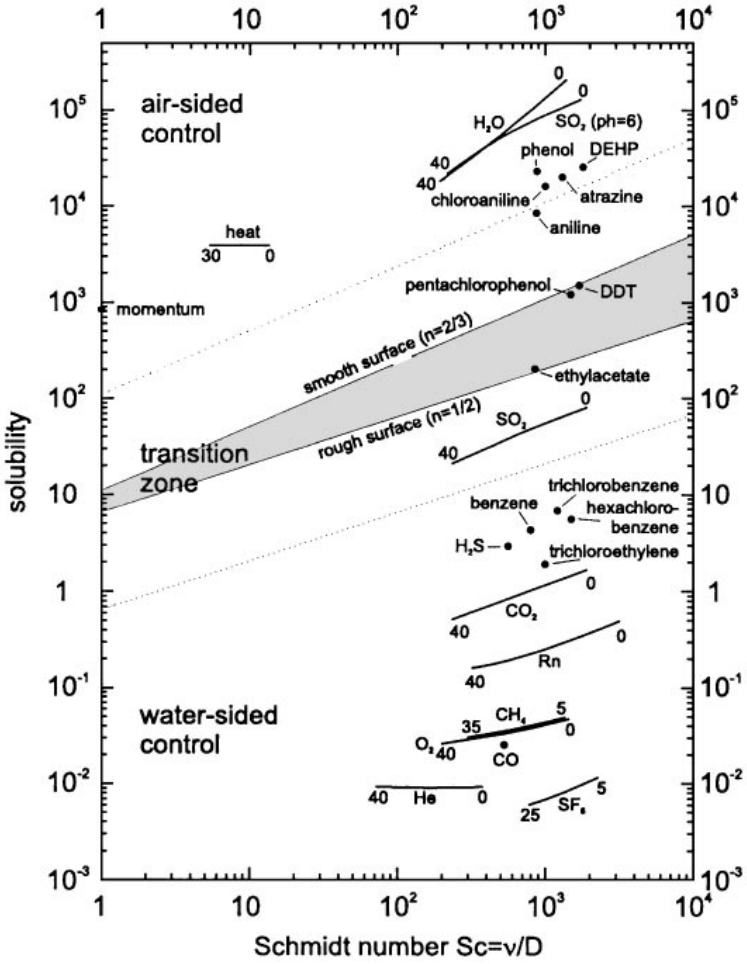

FIGURE 2.4: Diagram showing the Schmidt numbers of momentum, heat and gases with their solubility. Lines indicate temperature ranges [°C], filled circles: 20°C (from Jähne and Haussecker, 1998)

This is the so called **Facet Model** as described in further detail by Jähne et al. (2007). Despite the profound theory backing up this model, its predictions for the transfer velocity are in poor agreement with experimental data (cf. Krall, 2013).

2.3 Influence of the Schmidt Number

The Schmidt number is the only tracer-specific quantity that plays a role for the transfer velocity (cf. equation (2.43)). Together with the solubility of a tracer, it determines the control regime of the exchange process as seen in figure [2.4]. By splitting up the transfer resistance at the surface as proposed by Liss and Slater (1974):

$$R_{total} = R_w + \alpha R_a, \tag{2.46}$$

the regimes are either **air-** ($\alpha \frac{1}{k_a} \gg \frac{1}{k_w}$) or **water-sided** ($\alpha \frac{1}{k_a} \ll \frac{1}{k_w}$) or in a transition zone where none of the resistances is dominant.

A strong dependency of the Schmidt number on temperature is apparent in figure [2.4]. Since the temperature dependence of kinematic viscosity and mass diffusivity have opposite signs, this was found to be as high as (4-6)% per K (Jähne, Heinz, and Dietrich, 1987).

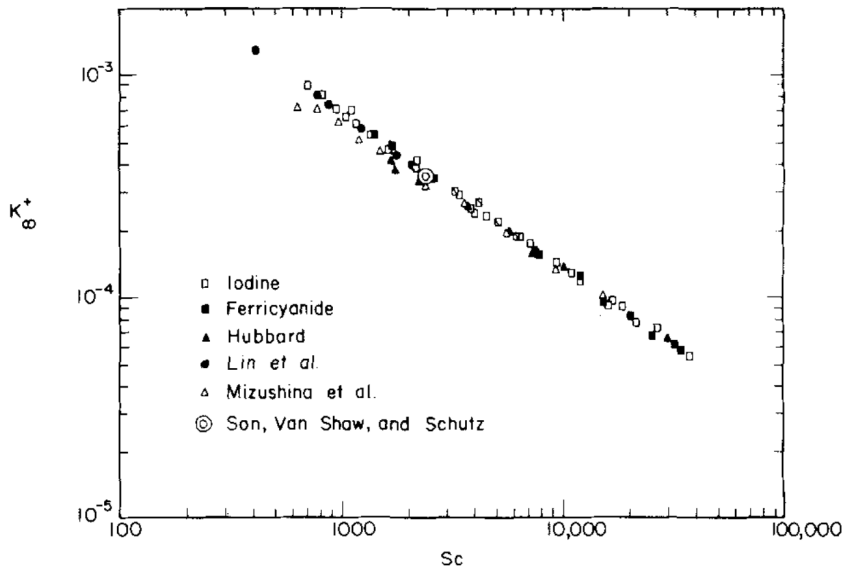

FIGURE 2.5: Comparison of electrochemical transfer velocity measurements for high Schmidt numbers by Shaw and Hanratty (1977) (notation: $K_\infty^+ \equiv k_+$)

Detailed experiments by Shaw and Hanratty (1977) measure mass transfer for a smooth surface with electrochemical methods, covering a Schmidt number range from 630-37000. Results are shown in figure [2.5] and the dependency is described by:

$$k_+ = 0.0889\, Sc^{-0.704}. \tag{2.47}$$

This is in close agreement with the theoretical prediction by Deacon (1977), in equation (2.37). The deviation in the exponent n means that for $Sc \to \infty$, the analogy between momentum and mass transfer does not hold anymore. More detailed calculations by (Campbell and Hanratty, 1983), based on a non-linear model result in $n = 0.7$.

To calculate the Schmidt number for a specific tracer, one needs to know its diffusion constant. In liquids, it can be determined via the **Stokes-Einstein equation** (see Einstein (1905) with proof for the general case in Kubo (1966)):

$$D = \frac{k_B T}{6\pi\eta r}, \tag{2.48}$$

with the thermal energy $k_b T$ and the dynamic viscosity η. Consequently, the Schmidt number of particles is determined by:

$$Sc = \frac{\eta}{\rho D} = r \cdot \frac{6\pi\eta^2}{\rho k_B T} \tag{2.49}$$

$$\approx r \cdot (3.6 \cdot 10^{12} m^{-1}) \quad \text{for water at } 25°C. \tag{2.50}$$

At a given temperature, the Schmidt number of a tracer in water is therefore solely dependent on the radius r. For a rough estimate, the particles in this work (see for example in figure [2.6]) are assumed to be circular with a radius of $1 - 2\mu m$. With (2.50), this leads to Schmidt numbers of $Sc \approx 5 \cdot 10^6$.

The larger the tracer particles get, the less their transport is hence governed by

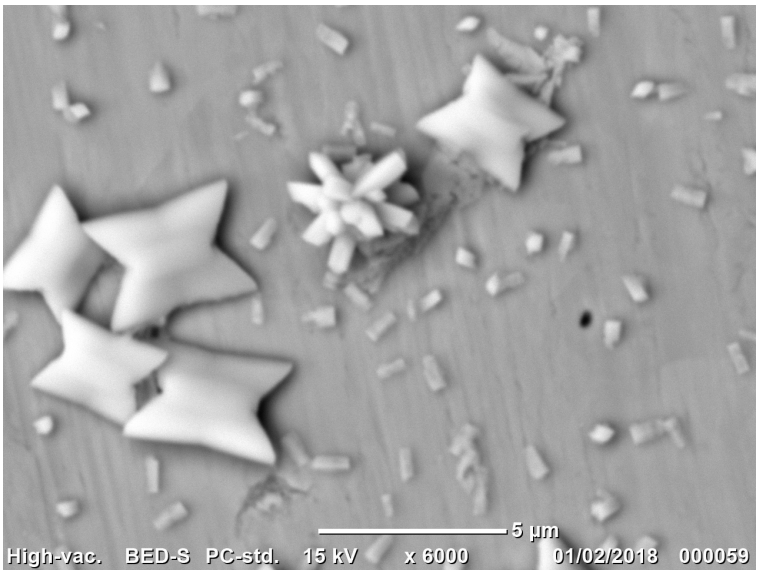

FIGURE 2.6: View on the reaction product $BaSO_3$ for the precipitate reaction imaging method developed in this work. Captured with a scanning electron microscope. More details in section 3.2.2 and A.

TABLE 2.1: Comparison of Schmidt numbers for different tracers

	Heat	**Gases**	**Precipitates**
Schmidt number	$\mathcal{O}(10)$	$\mathcal{O}(10^3)$	$\mathcal{O}(10^6)$
Visualization via	*Thermography* (see 3.1.1)	*BLI* (see 3.1.2)	*PRIM* (this work, see 3.2)

Brownian motion. This makes the bottleneck for mass transport even smaller and the transfer velocity sinks according to equation (2.47). On the other hand, for larger particles with larger mass, gravitational influence has to be taken into account. This leads to a sedimentation process where suspended particles fall/sink through the liquid. The sinkage velocity corresponds then to an additional transfer velocity k_{sed} through the mass boundary layer. By considering the extreme cases of high transfer velocity and fast settling, there has to be a minimum for the transport velocity where the diffusion is small enough and the sedimentation not that strong yet. The analogous process of particle deposition (out of the air onto surfaces) is of high interest in aerosol physics. Möller and Schumann (1970) measured the deposition velocity from air on water for a large range of (air-) diffusion coefficients and observed a minimum in deposition velocity at a particle radius of $r_{min} \approx (0.1\text{-}1)\mu m$. Model estimations for aerosol particle deposition on natural water surfaces by Williams (1982) are consistent with this order of magnitude. This suggests that the produced particles still have a high *effective* Schmidt number, if sedimentation is taken into account.

2.4 Influence of Chemical Reactions

The concentration profile of a tracer can also be influenced by its reactivity. One prominent example is the green house gas CO_2 that occurs in the ocean to 91% in form of hydrogen carbonate HCO_3^- (Rhein et al., 2013). Chemical reactions act as an additional contribution to the transfer velocity of a tracer. It provides a sink in

the boundary layer in the respect that concentration does not decrease by diffusion but through conversion. In this thesis, a visualization technique is developed that uses a reaction product on the water surface as tracer. The following considerations provide a framework on which such a method can be built upon.

The influence of chemical reactions on the transfer velocity is calculated for the example of a tracer A and reaction partner B following Cussler (2009, chap. 17):

$$\mathrm{A} + \mathrm{B} \longrightarrow \mathrm{P} \tag{2.51}$$

$$\frac{\partial[\mathrm{A}]}{\partial t} = -r_1 \cdot [\mathrm{A}] \equiv -r_1 \cdot c \qquad \text{(first order)} \tag{2.52}$$

$$= -r_2 \cdot [\mathrm{A}] \cdot [\mathrm{B}] \equiv -r_2 \cdot c \cdot h \quad \text{(second order)}, \tag{2.53}$$

with the reaction rates of first r_1 or second order r_2 reactions, and the concentrations c and h. The system is described adapting the simple film model[1].

If one reagent, B in this example, is present in excess, the reaction can be approximated to be of first order, i.e. only dependent on the concentration of the absorbed gas. The transport equation (2.9) can then be formulated to:

$$0 = D\frac{\partial^2 c}{\partial z^2} - r_1 \cdot c \tag{2.54}$$

$$\Rightarrow \quad c(z) = \gamma_1 \exp^{\sqrt{\frac{r_1}{D}}z} + \gamma_2 \exp^{-\sqrt{\frac{r_1}{D}}z}. \tag{2.55}$$

The integration constants $\gamma_{1,2}$ have to be chosen in accordance to Henry's Law (2.22) and the assumption, that the concentration of the absorbed gas in the bulk is zero. This can be expressed through the following boundary conditions:

$$c(z = 0) = c_{w,s} = \alpha c_{a,s} \tag{2.56}$$

$$c(z = z_*) = 0. \tag{2.57}$$

Integration consequently leads to following concentration profile in the film:

$$c(z) = c_{w,s}\frac{\sinh\left(\sqrt{\frac{r_1}{D}}(z_* - z)\right)}{\sinh\left(\sqrt{\frac{r_1}{D}}z_*\right)}. \tag{2.58}$$

It is important to note that for an inert gas with $r_1 \to 0$, this preserves the linear profile of the film model. The flux at the interface is calculated by:

$$j_c = -D\frac{\partial c}{\partial z}\Big|_{z=0} \tag{2.59}$$

$$= c_{w,s} \cdot \sqrt{r_1 D}\frac{\cosh\left(\sqrt{\frac{r_1}{D}}(z_* - z)\right)}{\sinh\left(\sqrt{\frac{r_1}{D}}z_*\right)}\Big|_{z=0} \tag{2.60}$$

$$\Rightarrow \quad k_{chem} = \sqrt{r_1 D}\coth\left(\sqrt{\frac{r_1}{D}}z_*\right). \tag{2.61}$$

This closed form reduces, like expected, to $k = \frac{D}{z_*}$ for $r_1 \to 0$ and for fast reactions it becomes $\sqrt{D \cdot r_1}$ as illustrated in figure [2.7].

[1] The following results can be extended to gas exchange models other than the film model (Astarita, Bisio, and Savage, 1983) but do not provide significant improvements (Cussler, 2009).

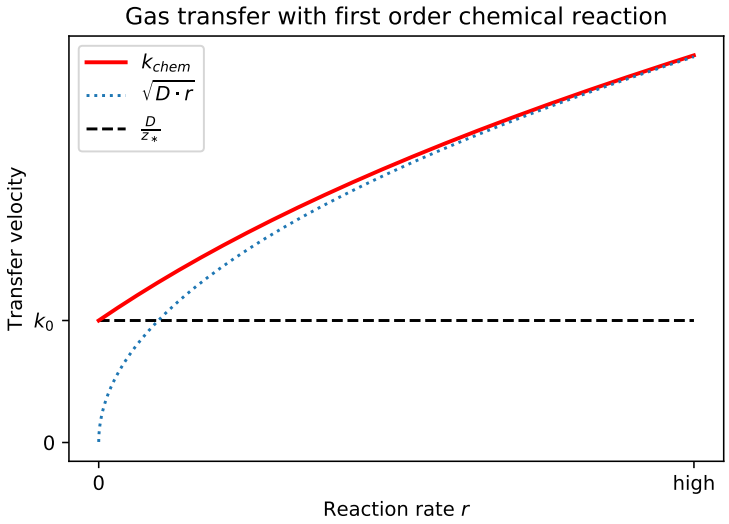

FIGURE 2.7: Behaviour of the transfer velocity of a (hypothetical) first order reaction with faster reaction rates.

Most processes however are not adequately described with first order reactions and the concentration h of the reactant B has to be considered, too. The mass balance then has to be formulated for both reagents:

$$0 = D_A \cdot \frac{\partial^2 c}{\partial z^2} - r_2 \cdot c \cdot h \tag{2.62}$$

$$0 = D_B \cdot \frac{\partial^2 h}{\partial z^2} - r_2 \cdot c \cdot h, \tag{2.63}$$

with boundary conditions similar to (2.57):

$$c(z = 0) = c_{w,s} \quad \text{and} \quad \frac{\partial h}{\partial z}\Big|_{z=0} = 0 \tag{2.64}$$

$$c(z = z_*) = 0 \quad \text{and} \quad h(z = z_*) = h_b, \tag{2.65}$$

with h_b as the bulk concentration of the water-sided reagent. Whereas the general equations have to be solved numerically, important special cases can be derived analytically. For a high, and therefore approximately unchanging, concentration of the solute reagent B, the reaction can be considered to be of first order and is solved by equation (2.61). Another interesting limiting case, illustrated in figure [2.8] appears when the reaction is instantaneous and non-reversible. This has as a consequence, that A and B cannot coexist and the reaction has no leftover reactants. The stoichiometric ratio $\nu_A n_A + \nu_B n_B = \nu_P n_P$, with the amounts of moles n and the stoichiometric coefficient $\nu := \frac{\nu_A}{\nu_B}$ is then equivalent to a balance in fluxes at the reaction front z_R:

$$\nu j_A + j_B = 0. \tag{2.66}$$

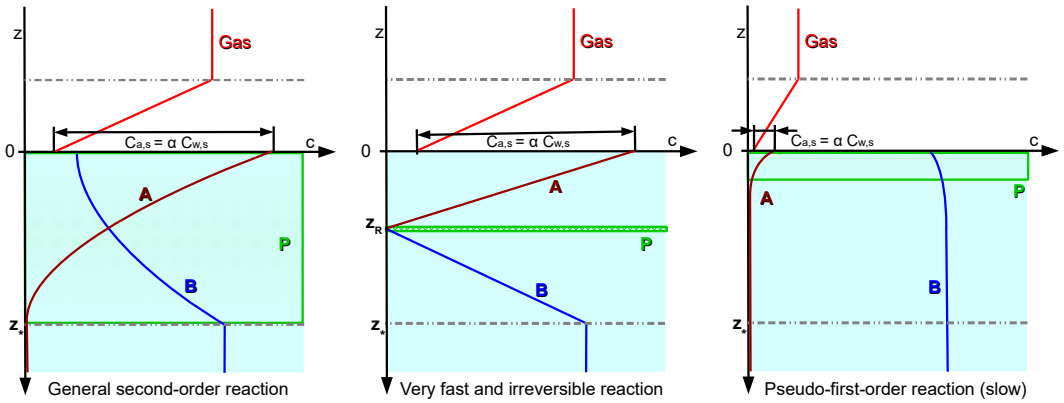

FIGURE 2.8: Sketches of concentration profiles for a second order chemical reaction in the film model and the limiting cases where reactants cannot coexist (*middle*) or B is present in excess (*right*)(modified after Cussler, 2009).

With diffusion as the only possible transport process, this is equivalent to two films with the thickness z_R and $(z_* - z_R)$, respectively. The fluxes are accordingly given by:

$$j_A = c_{w,s} \frac{D_A}{z_R} \tag{2.67}$$

$$j_B = -h_b \frac{D_B}{z_* - z_R} \tag{2.68}$$

$$\Rightarrow \quad z_R = \frac{D_A c_{w,s}}{j_A} = z_* - \frac{D_B h_b}{\nu j_A}. \tag{2.69}$$

Solving the last equation and reordering the terms appropriately yields:

$$j_A = c_{w,s} \cdot \frac{D_A}{z_*} \left(1 + \frac{D_B h_b}{\nu D_A c_{w,s}}\right) \tag{2.70}$$

$$\Rightarrow \quad k_{chem} = k' \left(1 + \frac{D_B h_b}{\nu D_A c_{w,s}}\right) \tag{2.71}$$

$$\Rightarrow \quad z_R = \frac{z_*}{1 + \frac{D_B h_b}{\nu D_A c_{w,s}}}. \tag{2.72}$$

The transport velocity was identified according to equation (2.19) and the transfer rate without reaction $k' = \frac{D_A}{z_*}$.

Considering these limiting cases provides powerful tools to estimate the influence of chemical reactions to the transport process. The bottom line for this work is the finding that for fast, irreversible reactions with B being present in excess, the production of P can be assumed to be directly at the interface.

2.5 Near-Surface Flow

For an incompressible Newtonian fluid, the continuity equation at the water surface means that horizontal velocity gradients have to be compensated by vertical flow:

$$\nabla \cdot \vec{u} = 0 \quad \Leftrightarrow \quad \frac{\partial u}{\partial x}|_{z=0} + \frac{\partial v}{\partial y}|_{z=0} = -\frac{\partial w}{\partial z}|_{z=0}. \tag{2.73}$$

Convergence and divergence zones at the surface are therefore directly related to transport processes and the thickness of the aqueous boundary layer.

This section will sketch the further physical transport mechanisms of wind forcing (section 2.1.3) to near-surface turbulence, and therefore higher exchange rates.

2.5.1 Waves

Wind blowing over an area of water generates Kelvin-Helmholtz instabilities, resulting in surface displacements. The most influential variables under laboratory conditions are the wind speed and fetch, the length of water over which a given wind has blown. For a free surface, the dispersion relation between wave number $k := \frac{2\pi}{\lambda}$ and frequency ω is given by (details e.g. in Kundu, 2008):

$$\omega = \sqrt{k\left(g + \frac{\sigma k^2}{\rho}\right)\tanh(kh)} \tag{2.74}$$

$$\approx \sqrt{k\left(g + \frac{\sigma k^2}{\rho}\right)}, \tag{2.75}$$

with the surface tension σ, gravitational acceleration g and an approximation for large water depth $h > \frac{\lambda}{2}$. Depending on whether the principal restoring force is gravity ($\omega \approx \sqrt{gk}$) or surface tension, they are called **gravity waves** (large wavelength) or **capillary waves** (high curvature), respectively. The phase velocity:

$$c(k) = \frac{\omega}{k} = \sqrt{\frac{g}{k} + \frac{\sigma k}{\rho}}, \tag{2.76}$$

can therefore be approximated to $c_{cap} \propto \sqrt{k}$ for the small wavelength of capillary waves and to $c_{grav} \propto \frac{1}{\sqrt{k}}$ for gravity waves. In the transition range, both types have similar phase velocities and *parasitic capillaries* can form on the leeward faces of gravity waves. Within this linear wave theory, fluid parcels below the surface follow closed ellipses. Stokes (1847) provides a framework to describe more complex wave forms, resulting in spiral movement. This **Stokes drift** (details e.g. in Kundu, 2008) leads to a mean particle drift with $u_s = 2S_0 e^{2\beta z} \approx \mathcal{O}(1\%)$ of the linear wave speed (empirical constants S_0, β) (Thorpe, 2004).

There is a critical surface stress, where the speed of a portion of the fluid at the wave crest overtakes the rest of its form. As a result, large amounts of wave energy are transformed into turbulence. This is called wave breaking and can be an influential factor for the enhancement of gas transfer. For large wind speeds, this effect is accompanied with the production of droplets and bubbles, enhancing the transport mechanisms substantially (cf. Flothow, 2017; Mischler, Krall, and Jähne, 2015; Woolf and Monahan, 1993). Within the scope of this thesis, only small to moderate wind speeds are considered so that these large wave effects do not play a role.

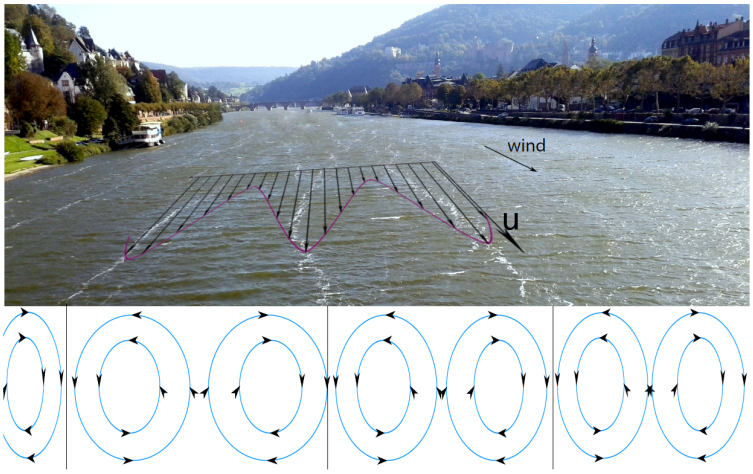

FIGURE 2.9: Langmuir circulations on the Neckar in Heidelberg with sketches of the surface velocity u and Langmuir cells (modified after Kräuter, 2015)

2.5.2 Microscale Breaking

Waves can however also break without air entrainment which is called **microscale breaking** and was first mentioned by Banner and Phillips (1974). Typically, microbreaking waves have an amplitude of $\mathcal{O}(1-10)$cm and a wavelength of $\mathcal{O}(0.1-1)$m (Zappa, Asher, and Jessup, 2001). Parasitic capillary waves ride on the forward face of a bore-like wave crest with a region of high vorticity underneath (Ebuchi, Kawamura, and Toba, 1987; Jessup et al., 1997). In contrast to whitecapping breakers, that occur not until way higher wind speeds (see Melville, 1996), wave crests of microbreakers can propagate for a noticeable distance. During the process, they dissipate energy and consequently their amplitude decreases significantly (Garbe et al., 2014). Models by Csanady (1990) show a significant enhancement of transport processes for moderate wind speeds due to the thinning of the aqueous boundary layer by generating surface divergence during breaking. Experimental data by Peirson and Banner (2003) shows that microscale breaking is a very efficient mechanism and the dominant process in enhancement of air-water exchange at moderate wind speeds (consistent with Bock et al., 1999; Jähne et al., 1987; Peirson, Walker, and Banner, 2014). Zappa, Asher, and Jessup (2001) show that the transfer velocity is linearly correlated with the area coverage of microscale breaking waves. Behind a microbreaking crest, turbulence is enhanced and the transport of heat and mass between the surface and water bulk is therefore more efficient.

2.5.3 Langmuir Circulation

When wind is steadily blowing over water bodies, one is likely to observe narrow bands of foam, bubbles or aquatic plants. These windrows were first described by Langmuir (1938), who reported on the accumulation of seaweed parallel to the wind.

Langmuir circulations are generated through a coupling of surface waves and wind induced shear stress (Garrett and Smith, 1976). The vorticity $\vec{\omega} = \nabla \times \vec{u}$ is stretched and tilted as a consequence of the Stokes drift interacting with wind-driven shear current. This process is described by following equations of motion

(Leibovich, 1983; Thorpe, 2004):

$$\frac{\partial u}{\partial t} + v\frac{\partial u}{\partial y} + w\frac{\partial u}{\partial z} = La\,\nabla^2 u \tag{2.77}$$

$$\frac{\partial \Omega}{\partial t} + v\frac{\partial \Omega}{\partial y} + w\frac{\partial \Omega}{\partial z} = La\,\nabla^2 \Omega - \frac{du_s}{dz}\frac{\partial u}{\partial y}, \tag{2.78}$$

with the dimensionless Langmuir number La, a measure for the balance of diffusion of downwind vorticity and vorticity production through the Stokes shift, governing the flow. Solving these equations leads to patterns of mean flow as sketched in figure [2.9]. Counter-rotating vortices are generated, resulting in regions of convergence and divergence at the surface.

A dominant characteristic at higher wind speeds are instabilities in the parallel streak pattern by the formation of Y junctions. These junctions preferably point downwind with an angle of about 30° between the two side branches (Farmer and Li, 1995).

Whereas this process is long known on the ocean, rivers and lakes with distances between streaks of $\mathcal{O}$(1-100)m, laboratory investigations observed these patterns also at scales of $\mathcal{O}$(1-10)cm (Caulliez, 1998). Melville, Shear, and Veron (1998) showed that the these smaller structures are in fact caused by the same mechanism and are therefore called micro Langmuir, or just Langmuir cells. The onset of this process enhances the heat and gas transfer by a factor of 1.7-2 (Veron and Melville, 2001). This makes Langmuir circulation to a dominant factor in the regime where waves occur (Stokes drift is necessary for their formation) but are not turbulently breaking yet.

2.5.4 Shear Induced Surface Patterns

Numerical simulations (Handler, Smith, and Leighton, 2001; Tsai, Chen, and Moeng, 2005) and laboratory experiments (Rashidi and Banerjee, 1990) showed that coherent turbulent structures can also evolve without surface waves. Handler, Smith, and Leighton (2001) observed small scale heat patterns in thermal images (method described in section 3.1.1) and simulations, caused solely by shear turbulence. On the surface, they form overlapping laminae with a headtail structure and were named **fish scales**, accordingly. The correlation length perpendicular to the wind between these streaky patterns is consistently (Handler, Savelyev, and Lindsey, 2012; Handler, Smith, and Leighton, 2001; Schnieders et al., 2013; Scott, Handler, and Smith, 2008; Tsai, Chen, and Moeng, 2005) found to be log-normally distributed around:

$$l^+ := \frac{u_*}{\nu} l \approx 100, \tag{2.79}$$

with the **streak spacing** l, non-dimensionalized by the quotient of friction velocity and kinematic viscosity $\frac{u_*}{\nu}$ that corresponds to the thickness of the viscous boundary layer (Grassl, 1976).

Whereas it is generally agreed upon that streaky patterns are caused by shear induced turbulence, their nature and formation mechanism is not yet resolved. Tsai, Chen, and Moeng (2005) suggest a stretching of vortex lines by the flow, to form horse shoe vortices as illustrated in figure [2.10] and described in detail by Tsai (1998). They are found in simulations to imping on the surface, break, and appear as two vortex connections with opposite sign. This is thought to cause upwelling of

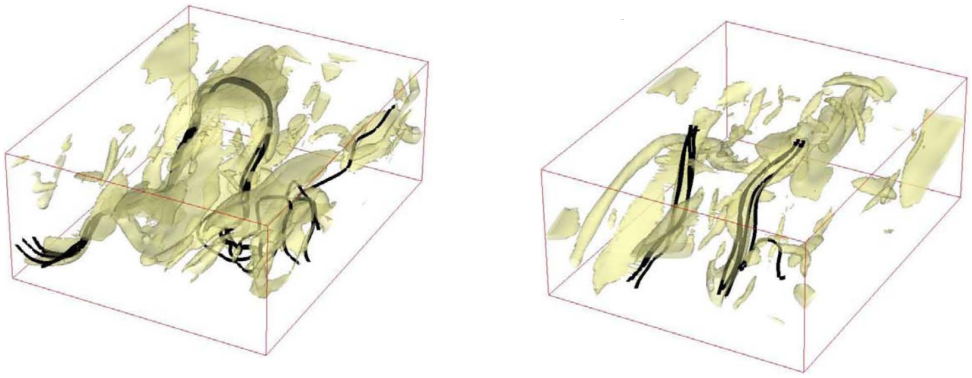

FIGURE 2.10: Illustration of a horse shoe vortex, moving upwards the surface. The head of the vortex lines breaks by bursting to the interface (from Tsai, 2007).

bulk-water and explain small scale convergence and divergence zones at the interface.

2.5.5 Summary and Characteristic Regimes

The types of coherent motion, populating the air-water interface are gravity waves, capillary ripples, Langmuir circulations and quasi-streamwise eddies. Recent progress in decomposition of thermal image data (Lu, Tsai, and Jähne, unpub.) attributes a similar contribution to these individual flow processes[2] of $\approx$ (20-30)% (under laboratory conditions at intermediate wind speed).

The results are in agreement with recent findings of Turney (2016) and can be summed up to the following[3]:
At low wind speeds of $u_* < 0.35\,\mathrm{cm/s}$, waves are not contributing yet and therefore streaky structures of shear induced turbulence dominate the transfer process.
For $0.35\,\mathrm{cm/s} < u_* < 0.74\,\mathrm{cm/s}$, surface waves and shear current grow, promoting the formation of Langmuir cells. They can be distinguished from solely shear induced streaks by a further longitudinal extend and longer persistence at the surface. Gravity waves, Langmuir cells and coherent turbulent vortices contribute about the same amount in this regime. Capillary waves are generating high near-surface velocity divergence but due to short lifetimes and small shear rates, their effective contribution is shown to be small (Turney, 2016).
At wind speeds of $u_* > 0.74\,\mathrm{cm/s}$, waves start to break turbulently and boundary layer disruptions as a consequence of microscale breaking events contribute most to the transport.
As the wind is increased further to values $u_* \sim 1.3\,\mathrm{cm/s}$, breaking waves lead to transverse turbulent eddies that dominate the transfer.

Measurements and observations within the scope of this thesis are conducted at low fetches of $F \sim 2\,\mathrm{m}$. The wave field is therefore to a lesser extend developed, resulting in systematic deviations of the u_* values provided in this section.

[2] The algorithm seems to overestimate the contributions of capillary waves, since surface signatures of strong turbulence of wave breaking events are attributed to their footprints.

[3] The reference wind speeds are for a fetch of $\sim 9\,\mathrm{m}$ and a tracer scaled to $Sc = 600$, following equation (2.44) with the assumption of $n = 0.5$. For consistency with this work, wind speeds are converted to u_{*w}.

Chapter 3

Methods

The main contribution of this thesis is the development of a new visualization technique of near-surface flow patterns for the investigation of transport processes. This chapter describes the conceptual ideas behind the experimental methods for horizontal imaging of the water surface.Analysing such image data seems to be the most promising approach to determine the individual contributions of characteristic flow processes to air-water gas transfer. At first, an overview of the two established techniques to visualize heat and gas transfer is provided. Results of these methods are later discussed in comparison to the newly developed techniques and are used to analyse the Schmidt number scalability. Focus is set on the description of the functioning principle of the precipitation reaction imaging method (PRIM) and the discussion of potential chemical systems. This work provides the first successful realization of this technique since its proposal by Jähne (1983a). While the main conceptual difference between active thermography and BLI is the diffusivity of the tracer ($\sim$100 times higher for heat), the diffusivity in the new method is again lower by almost three orders of magnitude. Additionally, the use of macroscopic tracer particles as further reference and for flow visualizations in the viscous boundary layer is discussed.

3.1 Established Visualization Methods

For a comparison of the experimental results of the different visualization methods, it is essential to know where the observed signals come from and what information they actually convey. Only by understanding the conceptual processes that the methods target to display, the grey values in the resulting image data can be compared and interpreted properly.

3.1.1 Thermography

Thermography is a way to visualize the temperature, and thus heat fluxes, at the water surface. There are three main passage ways for heat at the air-sea interface. Sensible heat flux is a consequence of a potential temperature difference between air and water according to the first law of thermodynamics. Following Planck's Law, radiative heat flux is due to electromagnetic radiation generated by thermal motion. During winter nights, when the air is far colder than the water, the ocean radiates up to $200\,\mathrm{W\,m^{-2}}$ into the atmosphere (Saunders, 1967), while during bright sunshine the flux can be with up to $500\,\mathrm{W\,m^{-2}}$ towards the water body (Fairall et al., 1996). The other important contribution is due to the enthalpy of water evaporation, known as latent heat flux. The energy needed for the phase transition of water molecules cools the water close to the interface. This process is dependent on the

air humidity φ and accounts at typical values of $\varphi = (60 - 80)\%$ for a flux of about $140\,\mathrm{W\,m^{-2}}$ (Garbe, 2001).

This effect causes the so-called *cool skin of the ocean*, meaning a typically negative net heat flux between air and ocean, with the surface temperature being below that of the water bulk. Transport processes at the interface are therefore associated with locally increased surface temperatures. This gives rise to distinct patterns at the interface that are observed with infrared cameras in **passive thermography**.

Active thermography on the other hand, uses additional heat sources, depositing a controlled amount of thermal energy onto the surface (*controlled flux*, Jähne et al., 1989). As described earlier, heat can be used as a proxy tracer for gas exchange by scaling the Schmidt (or in this case Prandtl) number according to equation (2.44). While this method was consequently used to determine transfer velocities (e.g. Garbe, Spies, and Jähne, 2003; Kunz, 2017; Nagel, 2014), the important aspect for this study is its potential to investigate near surface turbulence. High temporal and spacial resolutions made it possible to observe the thermal footprints of Langmuir circulations, streaky shear induced structures (fish scales) and surface disruptions attributed to microscale breaking (e.g. Handler, Savelyev, and Lindsey, 2012; Handler, Smith, and Leighton, 2001; Schnieders et al., 2013; Veron, Melville, and Lenain, 2011).

The heat exchange is found to be symmetric, i.e. active invasion and passive evasion experiments lead to analogous findings. Data from active thermography is better comparable with the other imaging techniques and therefore used in this study.

3.1.2 Boundary Layer Imaging

The boundary layer imaging method is inspired by the investigations of gas absorption of Hiby (1968) and Hiby, Braun, and Eickel (1967) and was proposed in this form by Jähne (1985). It was successfully implemented by Kräuter et al. (2014) and is since then actively used as a measurement technique. A detailed description of the method can be found in (Kräuter, 2015). The basic idea is to map the concentra-

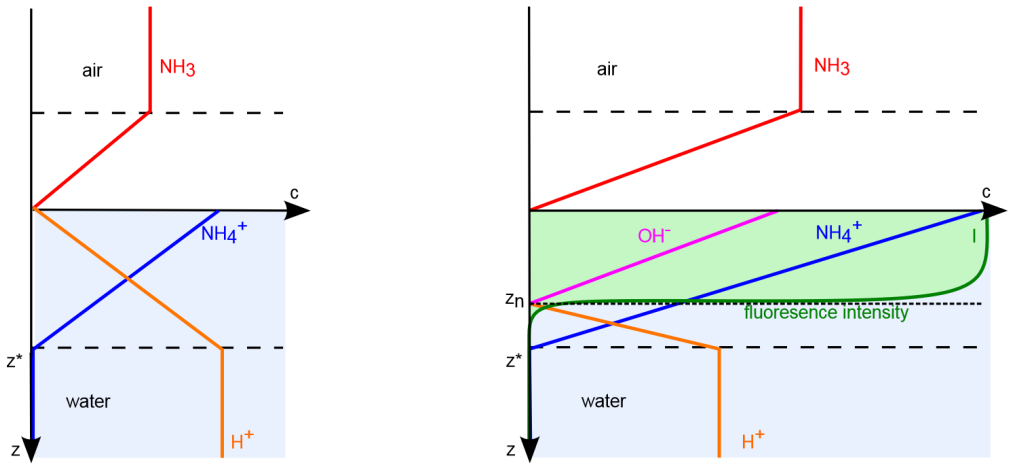

FIGURE 3.1: Schematic illustration of the concentration profile for the involved components of the BLI method (from Kräuter, 2015). The alkaline gas R reacts to RH^+ by increasing the pH value at the surface. For high concentrations in the air space, an alkaline layer with the thickness z_n (neutral) forms, inducing a fluorescence intensity I. The concentration of R is > 0, if pH(solution)>pK_a(R).

tion gradient of gas transfer onto a gradient of pH-values. A fluorescent indicator in the water-body makes high concentrations directly visible. For an alkaline tracer gas, the pH value in the water body has to be low to generate the reaction front described in section 2.4 and seen in figure [3.1].

With the use of suitable illumination sources, fluorescent light is observed as soon as the pH value reaches 7 while the pH value in the bulk is set to 4, meaning that influx of gas is not automatically entailing a signal but has to exceed this threshold. Streaks observed with BLI appear therefore to be thinner than they really are. The signal is integrated over the column of water below the surface and the depth of the signal cannot be measured. In convergence zones on the surface, the water enriched with alkaline gas is pushed together and fluorescence is high. In surface regions of divergence, acid bulk water is welling up, lowering the pH value below the threshold.

The concept is hence similar to active thermography. It is however important to stress that whereas in thermal imaging, grey values correspond to temperatures, in BLI they do *not* correspond to pH values as one might assume. Since fluorescence is a binary process in terms of acidity, signal strength solely depends on the *thickness* of the alkaline (i.e. the boundary-) layer. These effects have found to correlate strongly (Kräuter, 2015) as numerical simulations of wind waves suggest (Tsai et al., 2013).

3.2 Precipitation Reaction Imaging Method

The newly developed PRIM technique aims to make gas exchange directly visible. Tracer particles form by chemical reaction immediately at the interface and align in accordance to near surface flow patterns. One reagent is dissolved in the water-body in form of a salt and its reaction partner is provided by a gas in the air-space. The reactants form an insoluble salt at the interface and this reaction product is used as the tracer for gas exchange. The produced amount is made visible by scattered light from a suitable illumination source and captured on an image sensor.

Although this idea is not a new one (Jähne, 1983a), no experimental results on it have been published yet.

3.2.1 Basic Requirements

The desired chemical process is a precipitation reaction, as demonstrated in figure [3.2]. This is the combination of cations and anions in an aqueous solution to form an insoluble solid, called a precipitate. In the common example of a double replacement reaction, this means:

$$\mathrm{AB_{(aq)} + CD_{(aq)} \longrightarrow AD_{(aq)} + BC\downarrow}, \tag{3.1}$$

where BC, an insoluble salt, is designated as a solid. The complete ionic equation of this example is given by (electrical charge of ions $\equiv 1$ for simplicity):

$$\mathrm{A^+_{(aq)} + B^-_{(aq)} + C^+_{(aq)} + D^-_{(aq)} \longrightarrow A^+_{(aq)} + D^-_{(aq)} + BC\downarrow}. \tag{3.2}$$

The so-called spectator ions $\mathrm{A^+_{(aq)}}$ and $\mathrm{D^-_{(aq)}}$ do not contribute to the reaction and can therefore be left out. The net ionic reaction then reads:

$$\mathrm{B^-_{(aq)} + C^+_{(aq)} \longrightarrow BC\downarrow}. \tag{3.3}$$

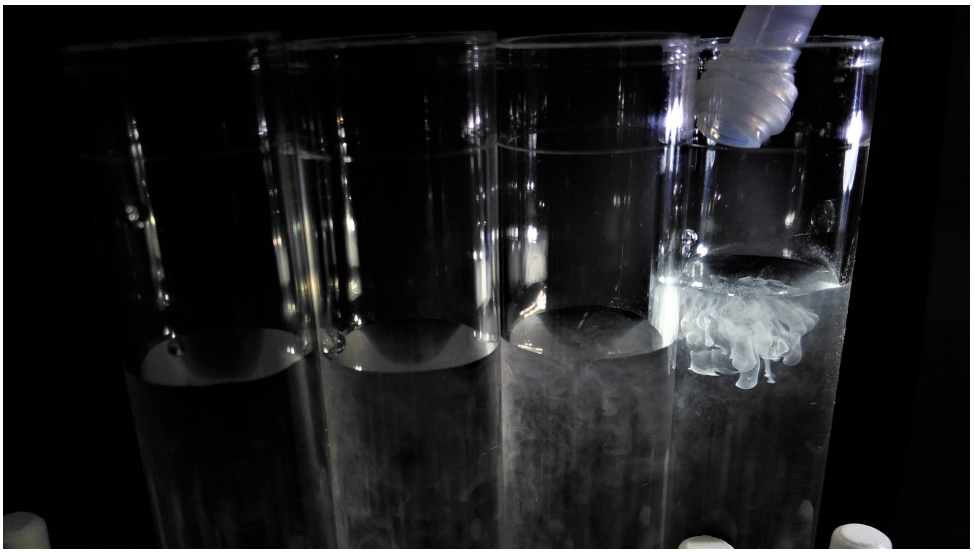

FIGURE 3.2: Image of preliminary tests of the reaction with different concentrations. In this example, precipitation of $BaSO_3$ is observed. The downwards facing 'fingers' are due to advection of the infusing gas.

For this process to occur, the product's solubility is assumed to be extremely small. The heterogeneous equilibrium between a salt and the dissolved ions in a saturated solution is described by the solubility product:

$$K_{sp} = [A^{q+}]^p [B^{p-}]^q \quad \text{for} \quad (A_p B_q)\downarrow \rightleftharpoons p\, A^{q+}_{(aq)} + q\, B^{p-}_{(aq)}. \tag{3.4}$$

Consequently, the reagents for this application should be chosen so that $K_{sp} \to 0$. This theoretical case can be conceived in a way that every ion pair reacts immediately upon contact. In this way, the precipitate can be observed as soon as the concentration fields of ions overlap. The overlapping area is getting infinitesimally small for $K_{sp} \to 0$.

If the concentration of the water-sided reagent is large enough, this means according to the preliminary considerations in section 2.4, that the precipitation reaction occurs at the very top of the boundary layer.

In the case of high air-sided concentrations, it can occur that not enough reaction partners are in the boundary layer. If at the surface the water-sided reagent is chemically used up completely, the reaction partners have to diffuse towards each other. This process is water-sided dominated and comparatively very slow. The precipitate is then produced at the reaction front within the boundary layer and not directly at the surface as desired. Hence, the concentration in the water h_b should be chosen much higher than the concentration of the gas at the surface due to Henry's law $c_{w,s}$. With this being the case, the chemical reaction takes place directly at the water surface and the amount of tracer particles is air-sided controlled. The observed grey values in the image data, i.e. the behaviour of the tracer, is then exclusively determined by the properties of the precipitate (not by the gas anymore).

This resulting tracer is desired to have a high effective Schmidt number. As discussed in section 2.3, the crucial factor for this purpose is the tracer's radius. This determines its properties in respect to diffusivity and sedimentation. More complex behaviour, like formation of particle clusters or interaction with the environment has also been taken into account.

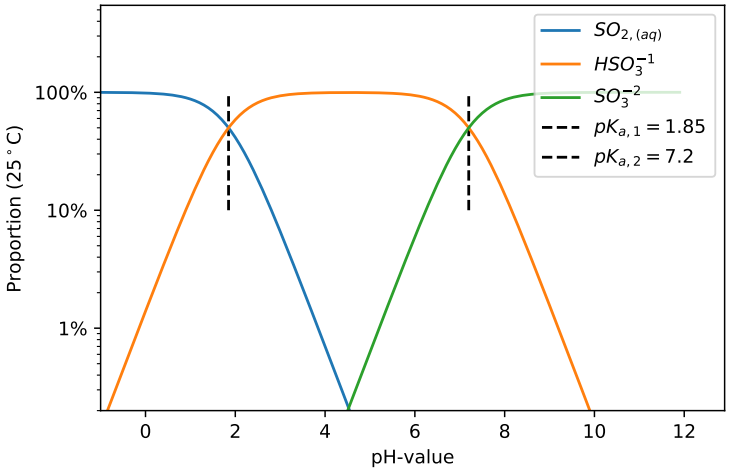

FIGURE 3.3: Ratio of ion species in aqueous solutions of sulfur dioxide (*sulfurous acid*) depending on the pH value. For pH= pK_a, the respective proportions are 50%.

The desired candidate for a long dwelling time in the boundary layer should therefore react fast, be chemically stable and have a (unchanging) size of $\approx 1\mu$m (cf. section 2.3) to diffuse slowly while not sinking.

3.2.2 Chemical System

To meet the above requirements on the experimental setup, three chemical systems were investigated. Their underlying reactions and conceptual pros and cons are listed here, and images of the tracer particles themselves, taken with a scanning electron microscope, are provided.

Barium Sulfite

The choice of the first chemical system was motivated by simultaneous measurements of air-sided laser induced fluorescence (LIF) of sulfur dioxide (SO_2). The natural occurring, toxic gas is highly soluble in water (cf. figure [2.4]) with $\alpha > 10^4$. It forms sulfurous acid, while H_2SO_3 is not found in solutions. The chemical equilibrium is determined by the reactions[1]:

$$SO_{2(aq)} + H_2O \rightleftharpoons {HSO_3}^-{}_{(aq)} + H^+ \tag{3.5}$$

$${HSO_3}^-{}_{(aq)} \rightleftharpoons {SO_3}^{2-}{}_{(aq)} + H^+, \tag{3.6}$$

with the acidities: ${HSO_3}^-$: $pK_{a1} = 1.85$ and ${SO_3}^{2-}$: $pK_{a2} = 6.99$ (Wiberg, Wiberg, and Holleman, 2007). The resulting proportions of the different species is hence dependent on the pH value and can be illustrated in a so-called *Bjerrum plot* in figure [3.3].

A suitable water-sided reaction partner was found with Barium (Ba) since the solubility product of the reaction product barium sulfite ($BaSO_3$) is sufficiently small: $K_{sp}^{BaSO_3} = 5.0 \times 10^{-10}$ (Haynes, 2016).

[1] Throughout this work, the aqueous cation hydronium H_3O^+ is (according to the literature) written as H^+ for simplicity.

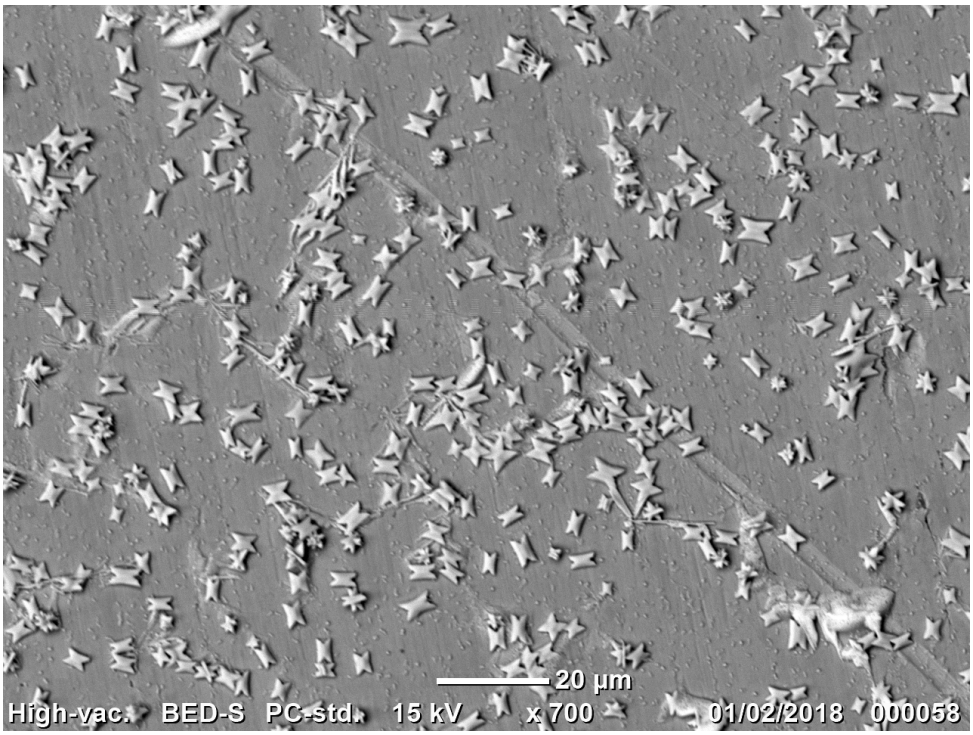

FIGURE 3.4: SEM image of the tracer $BaSO_3$. A picture with higher magnification is given figure [2.6], this view should emphasize the conformity of the particles. Figure [3.2] shows this tracer in water.

Barium in form of the salt barium chloride ($BaCl_2$) has a solubility in water of $\frac{35.8\,g}{100\,ml}$ at 20 °C (Haynes, 2016). The net ionic reaction of the desired precipitation is given by:

$$SO_3{}^{2-}{}_{(aq)} + Ba^{2+}{}_{(aq)} \longrightarrow BaSO_3\downarrow. \tag{3.7}$$

The uniform shape of the resulting salt seen in figure [3.4] reminds of the formation mechanism of hollow columns at snow flakes (Libbrecht, 2016). Spectroscopic analysis provided in appendix A confirms that indeed $BaSO_3$ is the precipitating reaction product.

Whereas the tracer itself fulfils the desired requirements, the chemical reaction turns out to be experimentally hard to control. To provide $SO_3{}^{2-}$ in excess at the water surface, it is not sufficient to set the pH value according to figure [3.3], since the intake of SO_2 in the boundary layer leads to locally higher concentrations of H^+ ions. With a lower pH value in the boundary layer, a significant amount of $HSO_3{}^-$ is present and not reacting, but getting transported to lower depth. In the more alkaline bulk, the ion is then likely to form $SO_3{}^{2-}$ and react to $BaSO_3$, leading to precipitate below the surface and hard to interpret results.

An additional complication is due to a possible transition of the system to a different reaction with atmospheric carbon dioxide.

Barium Carbonate

Carbon dioxide (CO_2) is also able to form a insoluble salt together with barium, namely barium carbonate ($BaCO_3$). Its solubility product is $K_{sp}^{BaCO_3} = 2.58 \times 10^{-9}$ (Haynes, 2016) and therefore still sufficient as precipitate. As seen in the Bjerrum

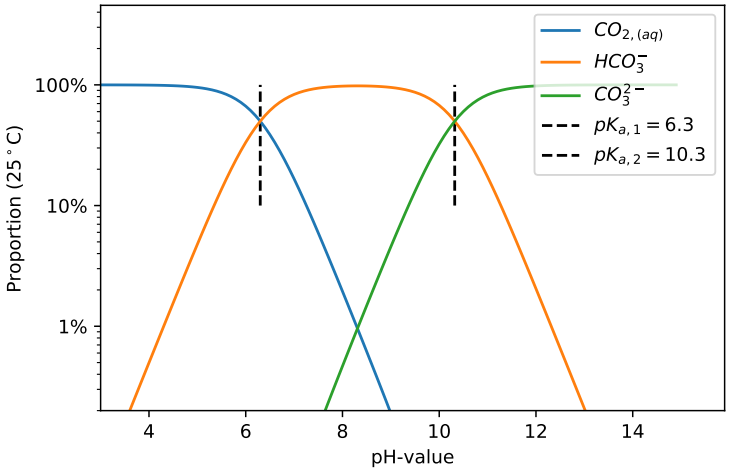

FIGURE 3.5: Ratio of ion species in aqueous solutions of carbon dioxide (*carbonic acid*) depending on the pH value, analogous to figure [3.3].

plot (figure [3.5]) for CO_2 in fresh water[2], ${CO_3}^{2-}$ is not present for neutral pH values. The acidities of carbonic acid are ${HCO_3}^-$: $pK_{a1} = 6.35$ and ${CO_3}^{2-}$: $pK_{a2} = 10.33$ (Wiberg, Wiberg, and Holleman, 2007).

To obtain the desired precipitation reaction:

$$ {CO_3}^{2-}{}_{(aq)} + {Ba}^{2+}{}_{(aq)} \longrightarrow BaCO_3 \downarrow, \tag{3.8} $$

it is therefore necessary to increase the pH value considerably. This was achieved by adding the strong lye sodium hydroxide (NaOH) to the system.

According to section 2.4, the reaction with the OH^- ions affects also the absorption rate of CO_2. Following the approximations of Jähne (1980) (neglecting the first term in equation (2.55)), the concentration profile for CO_2 has the form:

$$ c = \alpha c_a \exp(-\frac{z}{\bar{z}}), \quad \text{with:} \tag{3.9} $$

$$ \bar{z} = \sqrt{\frac{D}{r \cdot h}}, \tag{3.10} $$

where the penetration depth $\bar{z}$ depends on the concentration of OH^- h, the diffusion constant D and the reaction rate of CO_2 and OH^- $r = 6.9 \cdot 10^3 \frac{l}{\text{mol s}}$ (Kern, 1960). The penetration depth hence increases exponentially with lower concentrations of OH^- until it is transported in the bulk by turbulence.

CO_2 occurs with ∼400ppm in the atmosphere and is dissolved in purified water, where it causes the pH value to be acidic (∼ 5.5). This makes it hard to control the concentrations for triggering the precipitation reaction in a controlled way.

Silver Chloride

Subsequently to the experimental difficulties with the reviewed tracers, a new chemical system was tested. Silver chloride is well known for its low solubility and the precipitation reaction between silver nitrate ($AgNO_3$) and sodium chloride (NaCl) is

[2]While this assumed for any statement throughout this thesis, it is worth mentioning here since common illustrations use oceanic conditions, considering the buffering effect in the ocean.

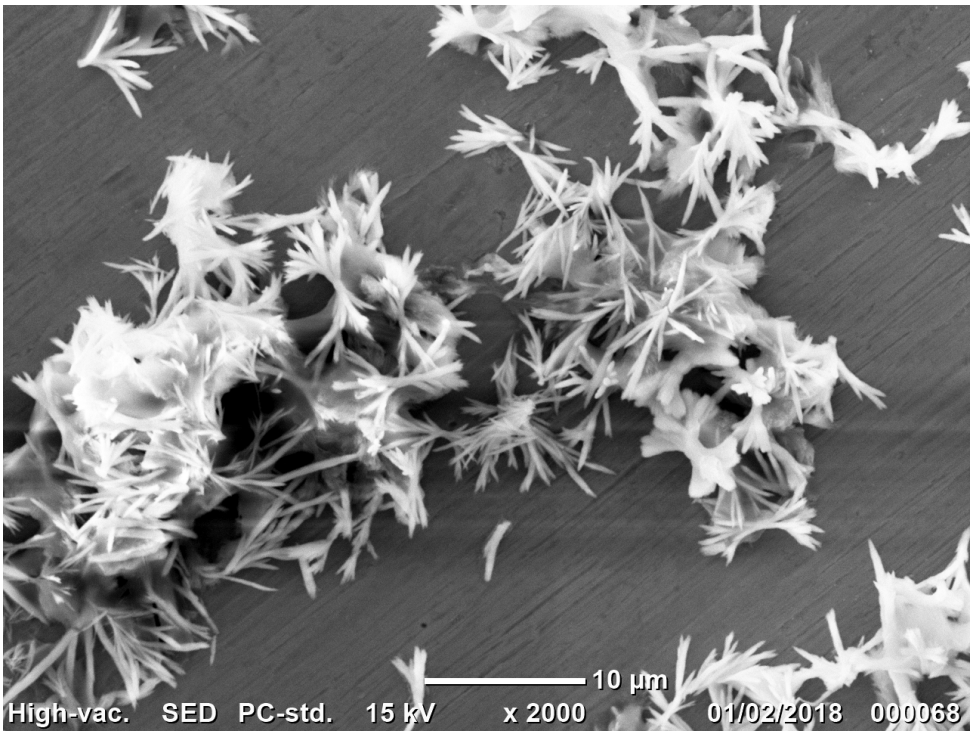

FIGURE 3.6: SEM image of the potential tracer $BaCO_3$. The picture shows the tendency of the crystals to cluster to larger compounds.

one of the most famous in chemistry. The solubility product is $K_{sp}^{AgCl} = 1.77 \times 10^{-10}$ (Haynes, 2016). $AgNO_3$ is with a solubility in water of $\frac{256\,g}{100\,ml}$ at 25 °C (Haynes, 2016) used to provide the water-sided reagent. Hydrogen chloride gas (HCl) is given in the air space. Upon contact with water, it forms the strong hydrochloric acid that dissolves instantaneously to H^+ and Cl^-. The precipitation reaction therefore reads:

$$Ag^+_{(aq)} + Cl^-_{(aq)} \longrightarrow AgCl\downarrow, \tag{3.11}$$

with the spectator ions H^+ and $NO_3{}^-$, lowering the pH value in the water over time. The reaction is effectively independent of the solution's pH value, it has merely an effect on the solubility of HCl. Since that is given with $K_H = 2.04 \cdot 10^6 \frac{mol^2}{atm\ kg^2}$ (Clegg and Brimblecombe, 1986; Sander, 2015) it is high enough and not relevant for the considerations in this work.

The major conceptual drawback of this method is the well-known photosensitivity of AgCl (cf. Gilleo, 1953):

$$2\,h\nu + 2\,AgCl \longrightarrow 2\,Ag + Cl_2\uparrow. \tag{3.12}$$

Whereas this is still used as a feature in analog photography and X-ray units, it is hard to quantify the influence of that effect in this framework. In the spectroscopic analysis with the SEM (cf. appendix A) can be seen that for the tracer particle in figure [3.7], the Cl_2 already dissipated.

This use of $AgNO_3$ and HCl has in preliminary experiments proven to be the best suitable chemical system available. Possible improvements could be achieved by using silver bromide (AgBr) with an even lower solubility of $K_{sp}^{AgBr} = 5.35 \times 10^{-13}$ (Haynes, 2016). This would provide the system with further sensitivity. Right now, a potential concentration of $h_{Ag+} = 10^{-3}$ and $c_{Cl-} = 1.77 \cdot 10^{-7}$ can coexist without

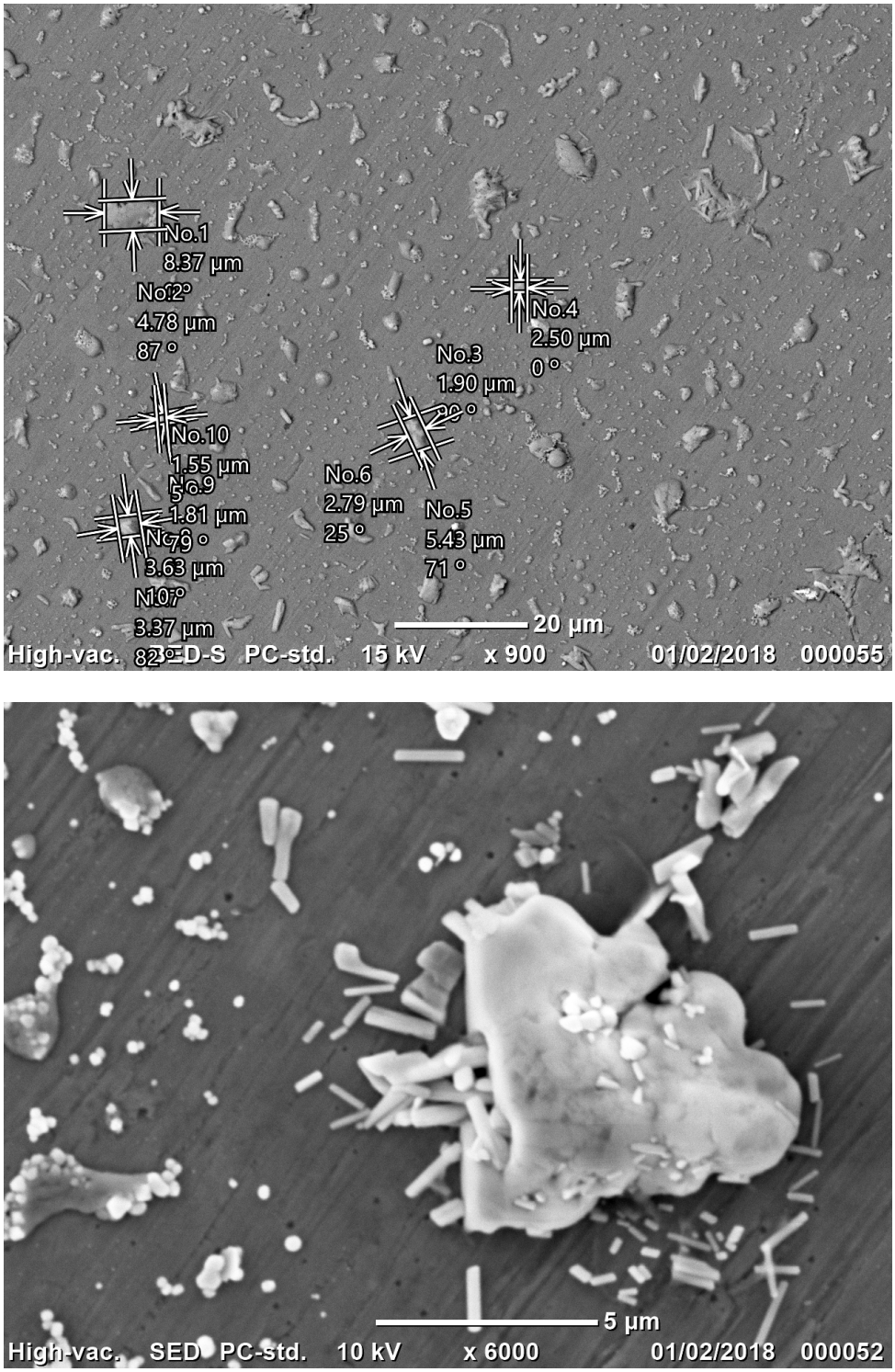

FIGURE 3.7: SEM images of the main tracer of this work, AgCl; *top:* overview of the particles and their different shapes; *bottom:* one example of the precipitate's shape.

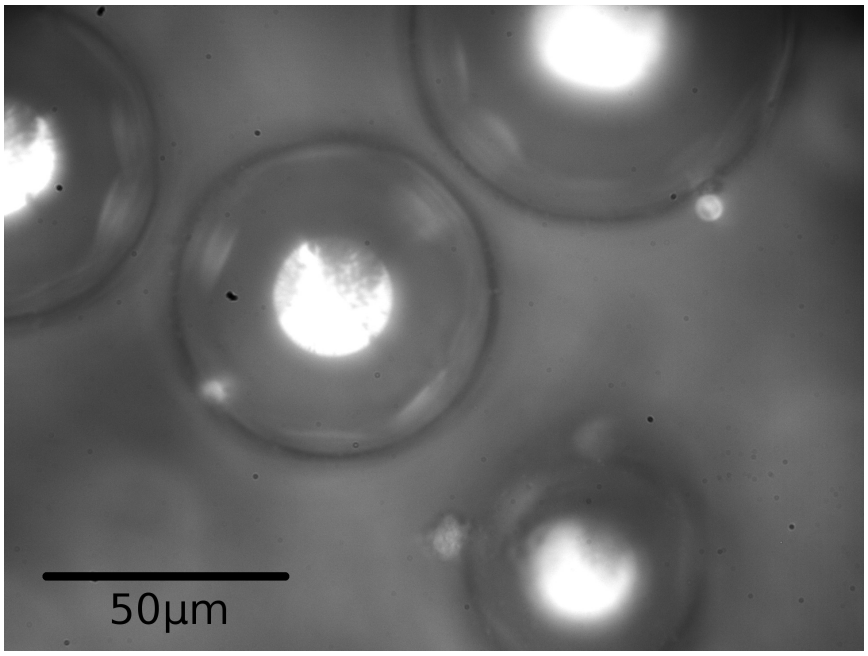

FIGURE 3.8: Small, hollow glass bubbles under an incident light microscope, recorded with a Basler ace camera.

any reaction being observable; that would consequently change to a value of $c_{Br-} = 5.35 \cdot 10^{-10}$.

3.3 Macroscopic Tracer

The search for tracers with high Schmidt numbers motivated experiments macroscopic tracer particles. Hollow glass spheres are expected to stay on the water surface and align in accordance to the near surface flow pattern. This is by construction not a technique that aims to visualize transport processes; of interest are the (two dimensional) flow patterns and especially convergence and divergence zones at the surface. This is in contrast to most comparable experiments that aim to observe 3D flow and vertical transport (Turney and Banerjee, 2013).

Different diameter were tested to find a suitable size for the tracer. As seeding particles, hollow micro glass balls with a density of $0.12\frac{\mathrm{g}}{\mathrm{cm}^3}$ and a diameter of 65-75μm are used (figure [3.8]). In addition, *Poraver* lightweight filler particles with diameters of 0.1 mm–2 mm and a particle density of $0.39\frac{\mathrm{g}}{\mathrm{cm}^3}$ are tested. The latter are not hollow but porous and have interesting surface properties as seen in figure [3.9]. Despite their big size and high buoyancy, they are found to immerse into the water and line up with the interface. This is attributed to their rough, porous surface and the surface tension of the water. By sticking out, the tracer directly provides the wind with a target and does not necessarily move with the velocity of the viscous boundary layer anymore. In this case however, the particle's diameter ideally determines its penetration depth in the viscous boundary layer. By using different tracer sizes, a velocity distribution as a function of penetration depth can be measured.

A conceptual disadvantage of this method however is the potential influence of the particles on the flow field. The glass bubbles may interact and collide among themselves, altering the observations.

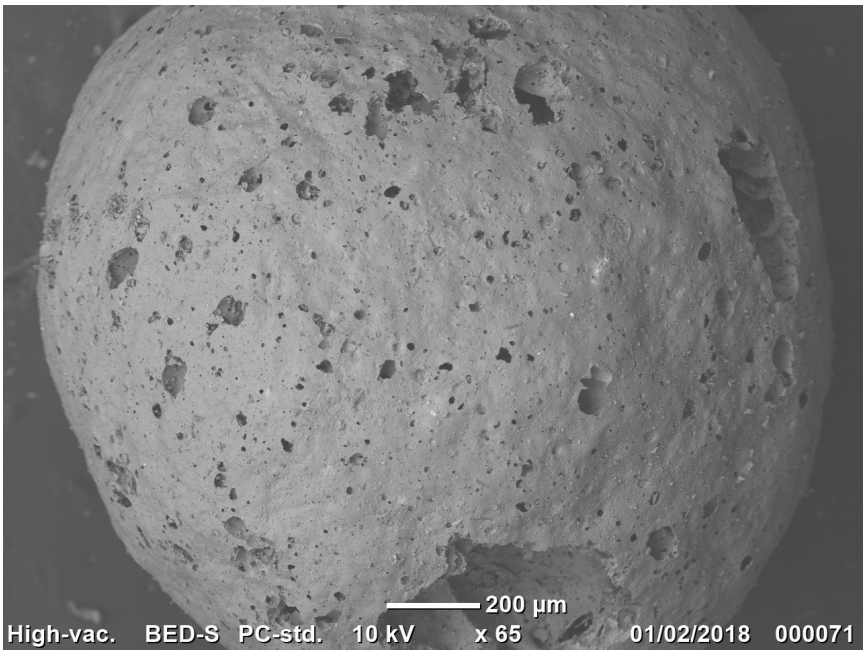

FIGURE 3.9: *Poraver* (size category: 1 mm–2 mm) glass bubble under the SEM for a better depth of field. The big indentation at the bottom is due to preparation with forceps.

In this work, the emphasis is on a comparison of the flow patterns of the different tracer. As long as no turbulent wave breaking occurs, these glass bubbles stay on the surface, showing the behaviour of $Sc \to \infty$. This basically expands table [2.1] by an additional column.

Chapter 4

Setup

With a clear conception of the visualization method, the major challenge is to develop a sensitive setup that is able to detect even minimal amounts of the precipitate. The implementation of PRIM's underlying idea (section 3.2) is described in detail. Focus is set on experimental challenges and on the individual components that were used to overcome them. In the course of this study, experiments were conducted in three different wind-wave channels at the *Institute of Environmental Physics Heidelberg* which are introduced shortly. For better comparability, the setups of other visualization approaches are also outlined.

4.1 Wind-Wave Facilities

Experiments were performed in three different wind-wave tunnels at the *Institute of Environmental Physics Heidelberg*. The Linear Visualization-Test Wind-Wave Tank (*Benjamin*) was used for preliminary tests and for a proof of concept. Subsequently, the setup for PRIM was developed at the more suitable *Heidelberg Linear Wind-Wave Tunnel*. The comparison data were obtained in the large annular wind-wave facility (*Aeolotron*). This is also where the measurements with glass bubbles were conducted. Wind speeds applied at the different channels can be compared by using the friction velocity u_* as described in 2.1.3.

4.1.1 The Linear Visualization-Test Wind-Wave Tank

The test wind-wave tunnel *Benjamin* was built by Warken (2010) and Winter (2011) and a more detailed description of the facility can be found in their theses. It is well suited for the tests of new measurement techniques because of good optical access and a small water (22l) and air (220l) volume. This allows for fast mixing times and experimentation with a large range of concentrations. The tank has a small total size with 4m in length, 1.5m in height and a width of 1m. An overview of the setup and geometry is given in figure [4.1]. The convenience for measurements at this tank comes with drawbacks in respect to unrealistic wave formation and non-optimized flow field. Mainly responsible is the low water depth and the deepening in the central section which introduces additional eddies.

4.1.2 The Heidelberg Linear Wind-Wave Tunnel

The larger linear tunnel satisfies experimental demands way better. A detailed description of this tank is provided by Herzog (2010), who built it in the framework of her thesis. It was designed for optimized optical access, chemical resistance and high quality of flow. Due to the linear shape, a logarithmic wind profile is present, allowing for u_* measurements. The dimensions and instrumentation of the facility

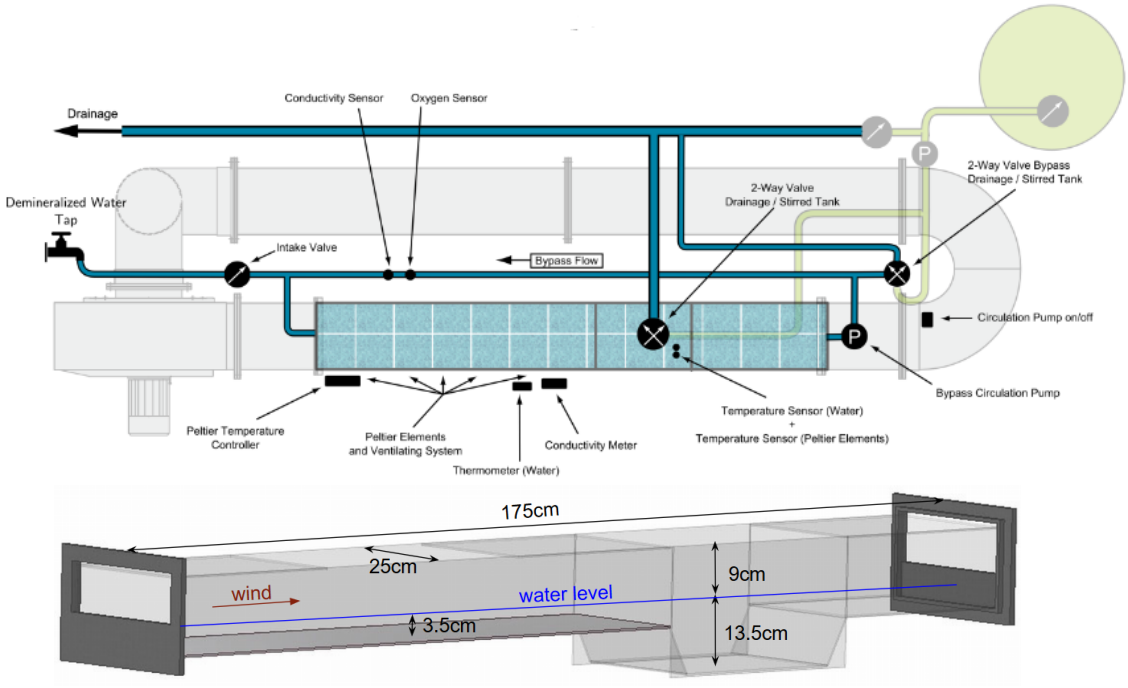

FIGURE 4.1: Schematic drawings of the setup (top view) and the water channel with all important dimensions of the *Benjamin* tank (modified after Winter, 2011).

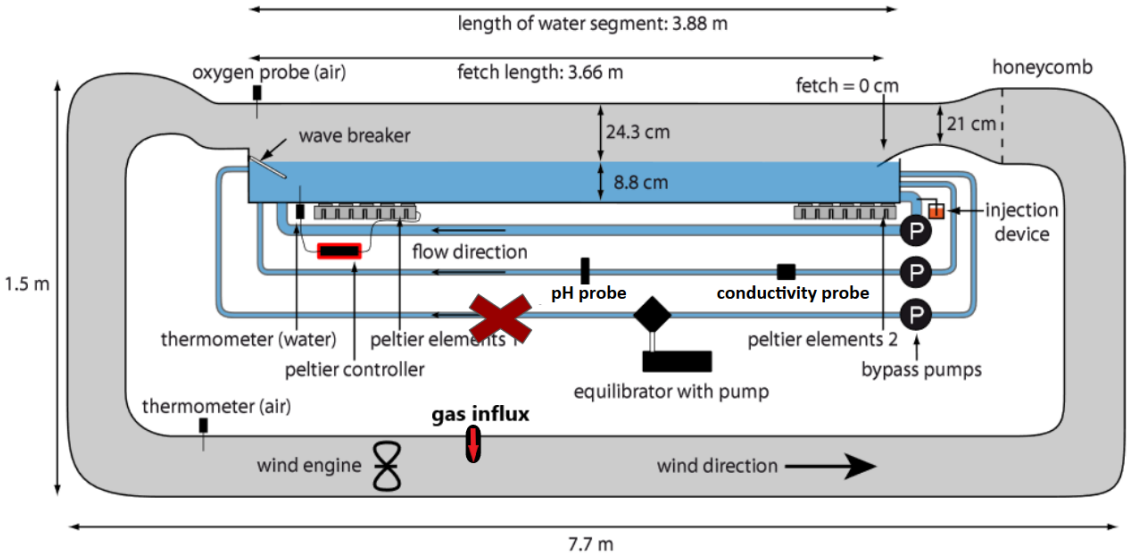

FIGURE 4.2: Sketch of the *Heidelberg Linear Wind-Wave Tunnel* from the side (modified after Friedl, 2013). The third bypass (red cross) was not used in this work.

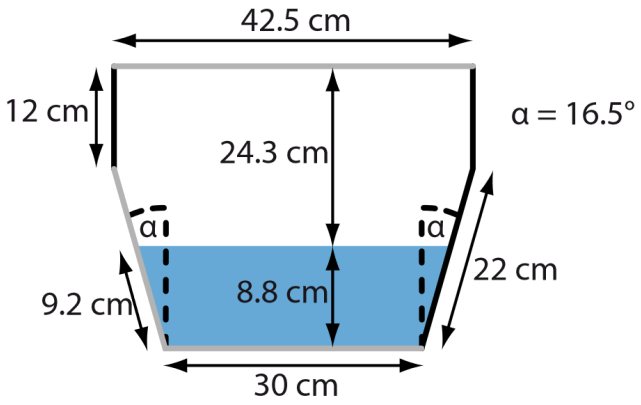

FIGURE 4.3: Cross section of the water segment, showing the tilted side window (glass in grey, black indicates non-transparent PCV) (Friedl, 2013). Experiments in this work were conducted with a water height of 9 cm.

are shown in figure [4.2]. Total air volume is $(3.3 \pm 0.3)\mathrm{m}^3$ with a water capacity of $(126 \pm 8)l$ and additional $24l$ in the tubes. The maximum fetch length is 3.66m with visual access from 35 cm to 255 cm and a water surface area of about 1.28 m^2. Wave reflections are suppressed by a 80 cm long wave breaker at the end. Pure water with a conductivity of less than 0.1 µS/cm is used for the experiments.

Optical access from the top, bottom as well as from the side (compare figure [4.3]) allows for manifold illumination angles and camera perspectives.

4.1.3 Aeolotron

With a circumference of 27.3 m at the inner wall, a width of 60 cm and 2.41 m in height, the annular *Aeolotron* far bigger than the described linear tanks. The water depth during experiments is set to 1.00 m, resulting in a water volume of 18.0 m^3 and 24.3 m^3 of air-space. Experiments are conducted with purified water and further detail is provided by Richter (2009). Recent modifications, including the installation of additional wind turbines, make a stronger and more homogeneous wind field possible. All measurements associated with this work were conducted after the installation of the two additional fans. The global friction velocity u_* is measured by impulse balance method as described by Bopp (2014). Local variations of the velocity field with the new axial fans are not yet determined but are assumed to be within the error range of ±10%. This means, the conditions are approximately the same everywhere in the tank and, due to the geometry, the fetch length is infinite. Since field measurements on the ocean also have approximately unlimited fetch, this models more realistic conditions than linear facilities. In addition, homogeneous flow conditions allow for better interpretations of integrated measurements, like mass balance for gas exchange. It can however still be desirable to measure at a certain fetch, for example to investigate the generation of waves and turbulence or to compare experimental findings with other facilities. Figure [4.4] shows the installation of a wave absorber that can be moved around to measure at fetches of any fraction of the channel's circumference. At the end of the absorber, waves are fully suppressed and have to rebuild.

Almost a third of the water surface is visible through a large window. Segment 13 has optical access from the top and the bottom, as well as a narrow window at the inner wall, allowing for measurements at varying water heights. A large,

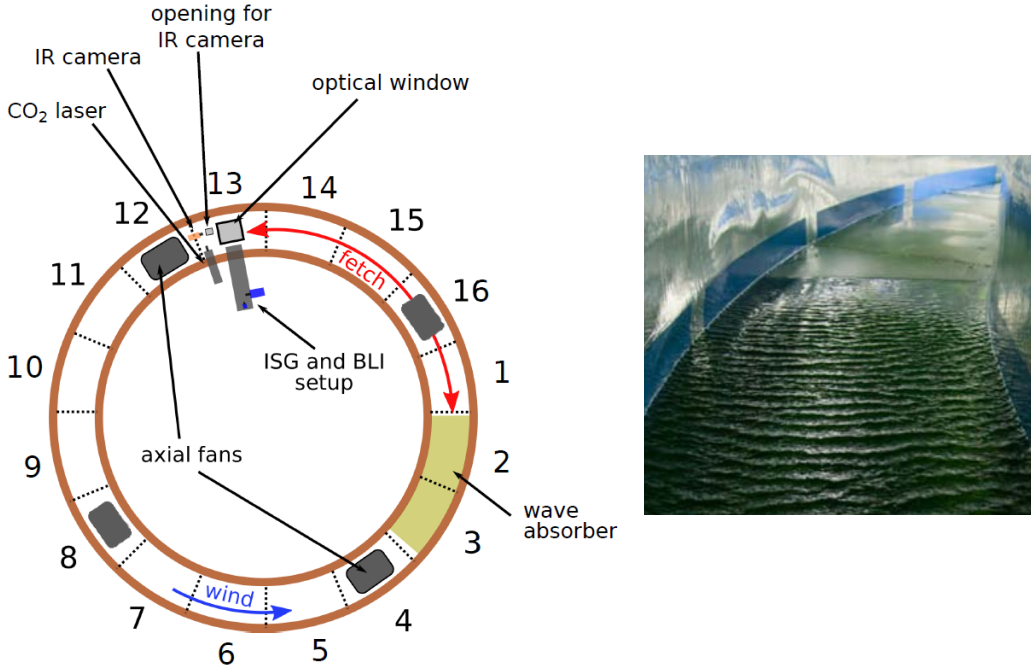

FIGURE 4.4: Schematic image of the *Aeolotron* (*left*, modified after Kunz, 2017) and a picture of the interior with installed wave absorber (*right*, from Kropp, 2015).

programmable LED light source is mounted underneath the water flume as part of the imaging slope gauge (ISG) measurement system. Together with a high-speed camera, wave slopes can be determined based on the shape from refraction principle (for details see Kiefhaber et al., 2014).

4.1.4 Surface Tracking Setup

The ISG setup, as seen in figure [4.5], is used in this work for the tracking of glass bubbles at the water surface . The light source was for this purpose programmed to emit a homogeneous illumination field, triggered by the frame rate of the camera. A high-speed, high-resolution *pco.dimax* camera (PCO AG) is used with a *NIKKOR* 200mm Nikon lens. The high focal length and frame rates of up to 800 Hz make it possible to track even the smallest glass bubbles with a diameter of 70 mm. The illumination is sufficient to measure with an aperture of $f = 11$. This provides a depth of field that is larger than the wave amplitudes for the wind speeds of interest.

With this setup, the camera does not obtain any depth information about the tracer particle. Therefore, an additional Basler camera (cf. section 4.2.3) is installed at the narrow window on the inner wall of the facility (segment 13). By recording the vertical water profile, the fraction of tracer particles that are transported from the interface to the water bulk can be observed. The wind is chosen to be small enough to make sure that the observed glass bubbles remain at the surface.

4.1.5 Thermography and BLI Setup

Since image data of active thermography and boundary layer imaging is taken as a comparison for PRIM data, their experimental setups are outlined. Detailed descriptions are provided by Kunz (2017) and Kräuter (2015). In the *Aeolotron*, it is possible

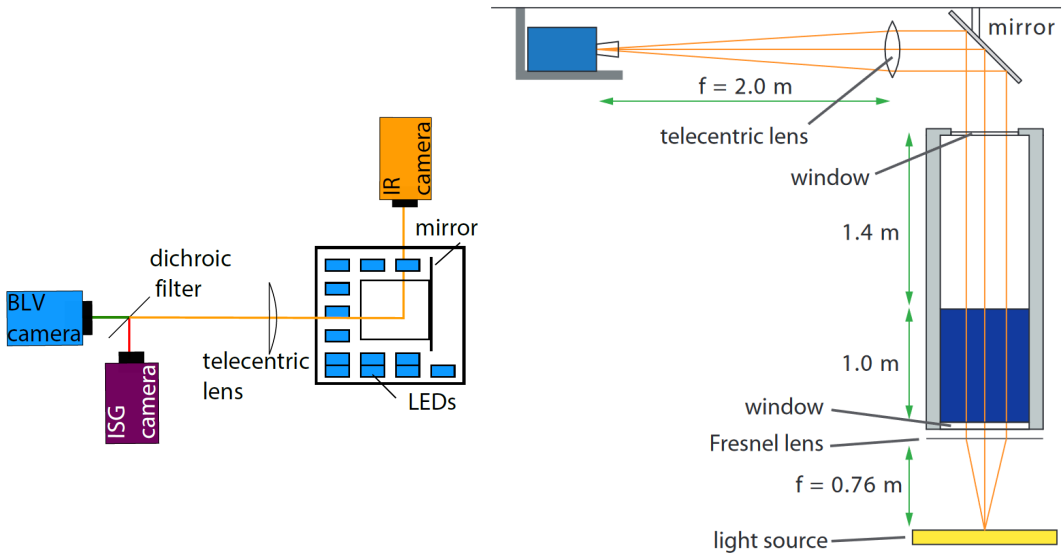

FIGURE 4.5: Sketches of the camera setup (*left*, from Kräuter, 2015) and the telecentric setup used for BLI, surface tracking and ISG measurements (*right*, from Kiefhaber et al., 2014) at segment 13.

to conduct both measurements, together with slope metering with the ISG setup, at the same surface patch.

The infrared camera is a *Velox 327k M* by IRcam with a thermal sensitivity of 200 mK, 640 × 512 pixel and maximum frame rate of 207 Hz. As heat source, a CO_2 infrared laser is used with diffractive beam shaping devices. Both are mounted next to the glass window at the top with an inclination angle of $\approx 15°$.

Figure [4.5] shows how the cameras for BLI and ISG share the telecentric setup. The large planoconvex lens allows for a constant magnification factor for varying water heights and avoid perspective projections. Blue LEDs, mounted above the window, are used as illumination source. Their emission spectrum with a peak around 455 nm fits the absorption maximum of the fluorescence dye. Optical filters are used in front of the camera as well as the LEDs to assure that only fluorescent light is seen by the camera. A low-noise, high-resolution *pco.edge* camera (PCO AG) with 5.5 mega pixel resolution and maximum frame rate of 100 Hz is used.

For the data used in this work, the wave absorber (in figure [4.4]) was used to limit the fetch to 2 m. In this way, the conditions in the *Aeolotron* become comparable to measurements in the *Heidelberg Linear Wind-Wave Tunnel*. Since the measurement of u_* relies on the global momentum balance, no definite statement can be made about the local variations and the influence of limited fetch. Independent wind measurements suggest however, that the true value is within the given error margin of 10%.

4.2 PRIM Setup

After the method has shown to be conceptual possible in the *Benjamin* test tank (see figure 4.6), the focus was on optimizing the setup in the larger linear tunnel. The main experimental challenge of this visualization technique arises from the fact that the illumination and the scattered light falling on the image sensor have the same wavelength. This is in contrast to the established optical visualization methods LIF

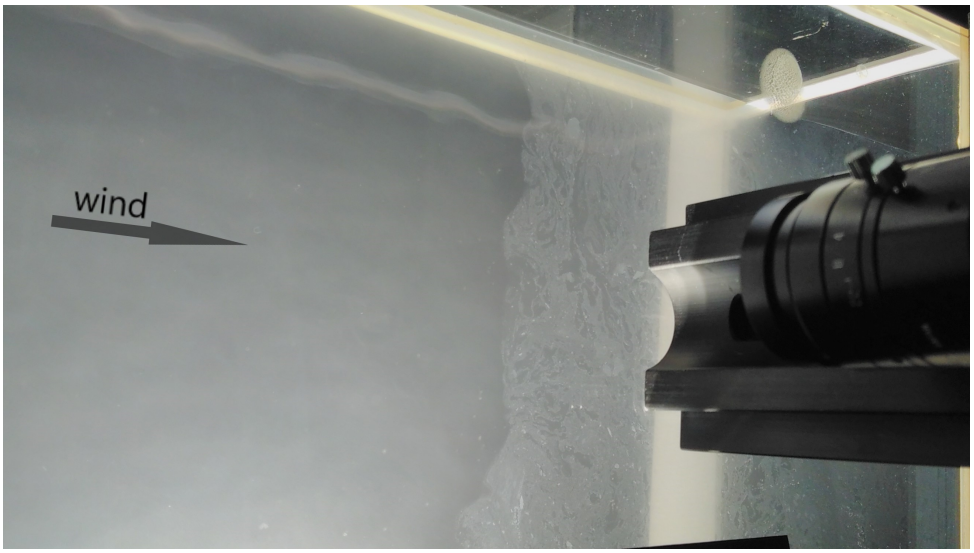

FIGURE 4.6: Top view on an experiment with $BaCO_3$ in the *Benjamin* channel. As the reaction progresses, the precipitate accumulates towards the beach and the water becomes cloudy. On the right-hand side one sees the TAMRON lens of the Basler camera.

and BLI, where fluorescent dyes enable the experimentalist to filter all frequencies, in particular the one of incidental excitation, except for the emitted light intended to see. PRIM however aims to detect the tracer particles by their scattered light, making it impossible to filter disturbing signals coming from the water surface right away.

4.2.1 Illumination

Several different light sources have been used in the course of the development of the technique. In the beginning, white LED light sources were sufficient and allowed for flexible illumination from different angles. To make lower exposure times possible, programmable LEDs (green) were used that could be triggered with the camera system. To isolate the surface from the rest of the water-body, an absorbing dye needed to be added to the water (described in detail in section 4.2.2). The illumination wavelength had to be adapted in order to work together with the absorber. Consequently, two new, blue LED light sources with a mean wavelength of 470nm were built. This allowed for first useful results, as shown in figure [4.7].

The blue LEDs however turned out to be not ideal either, mainly because of the hardly avoidable reflections from the water surface directly onto the image sensor. Point-like light sources, on the other hand, only lead to direct reflections under a distinct angle and are therefore better suited for this application. For that reason, systems of blue lasers with a wavelength of $(445 - 446)$nm (spectra in figure [4.9]) are used. Compared to the LEDs, this is a better suited wavelength in combination with tartrazine (cf. section 4.2.2 and figure [4.10]). Every laser diode is incorporated in an eloxed aluminium heat sink. On top is the control electronics with two buffer capacitors, allowing to trigger the system together with the camera. Cylindrical lenses allow to adjust the lasers to a broad sheet, providing a homogeneously illuminated surface patch. As a trade of between few angles of direct reflection and high homogeneity, two lasers are mounted at each fetch length of interest as seen in figure [4.8].

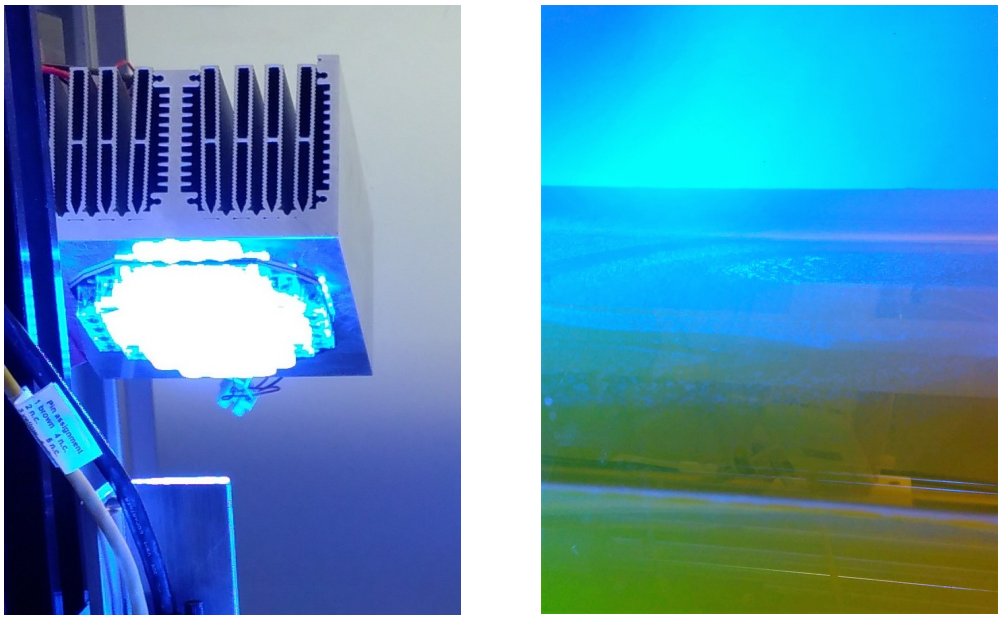

FIGURE 4.7: Illustration of the blue LED's functioning. The tracer particles here are clearly visible because they accumulated on the surface over a long time period without wind

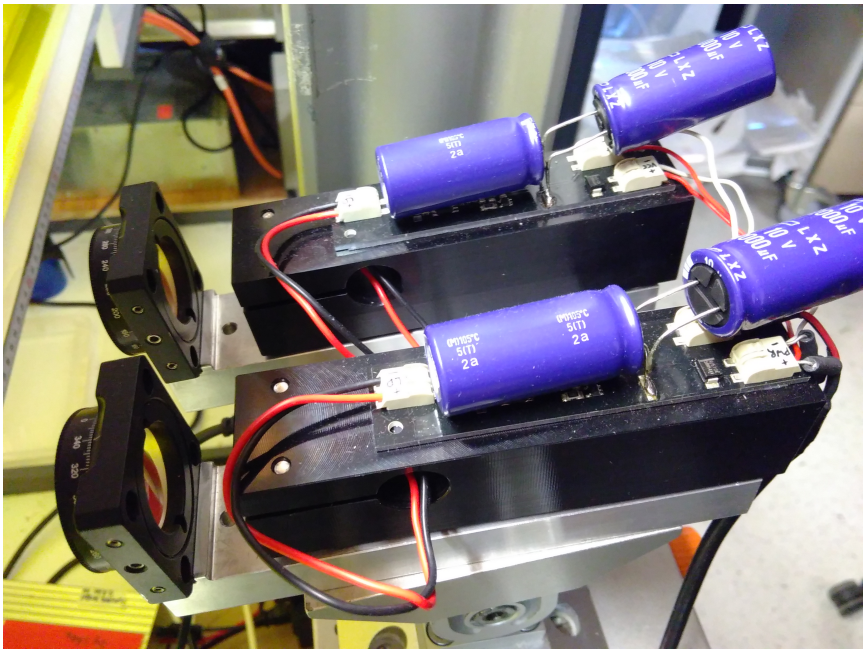

FIGURE 4.8: Laser illumination system, mounted at the side window of the *Heidelberg Linear Wind-Wave Tunnel*. A laser diode is incorporated in an eloxed aluminium heat sink. On top is the control electronics with two buffer capacitors. A cylindrical lens is mounted in front of it to achieve best possible homogeneity.

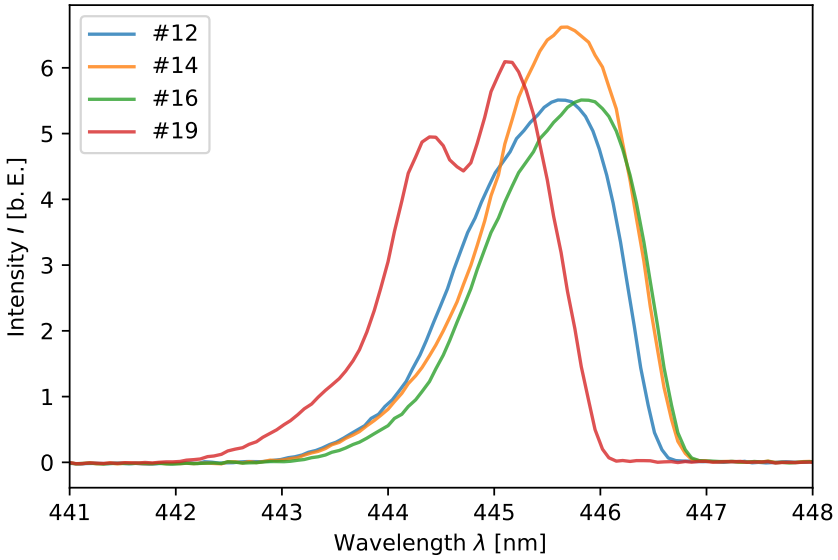

FIGURE 4.9: Spectra of the used lasers (measured in cooperation with Arne Emmel). #12 and #14 were mounted at the larger fetch of $F_2 = 220\,\text{cm}$ while #16 and #19 were in use at $F_1 = 120\,\text{cm}$.

Direct reflections and disturbing signals from the water below the top surface layer could therefore be suppressed to a great extend. What turns out to be more complicated to avoid are lens effects of the water waves. Light refractions due to the curved water surface lead to shadowing effects, making the waves appear brighter and troughs darker. While this effect is not important at a smooth interface, its influence grows with wind speed as waves become stronger.

4.2.2 Absorption Dye

Only tracer particles within the (aqueous, since the reaction occurs in the water) boundary layer are of importance for the interpretation of PRIM data. Precipitate within the well mixed water bulk results in cloudy water and grey images without information about gas exchange.

The vertical transport due to diffusion and sedimentation of the tracers is found to be very small, as desired. There are however several effects that still lead to the observation of precipitate below the surface. One reason are microscale breaking and other surface renewal events that transport the particles from the surface into the bulk. Because of the tank's linearity, additional turbulence is introduced at the beach at maximum fetch. Most particles are observed to accumulate there at the surface, as in figure [4.6], but a considerable fraction is transported downwards. Another cause is incompleteness of the precipitation reaction. Although the chemical systems are chosen to have a low solubility product, not all ions react to form the product. Even if a first order chemical reaction is assumed, the dissociation equilibrium of $K_{sp} = [\text{A}] \cdot [\text{B}] > 0$ sets in. This non-zero solubility product leads to a certain concentration of the reagent that is coming from the air-space in the water bulk.

To block out scattering light from the resulting turbidity of the water, the absorption dye **tartrazine**, $C_{16}H_9N_4O_9S_2Na_3$, is used. The intensity of incoming light is

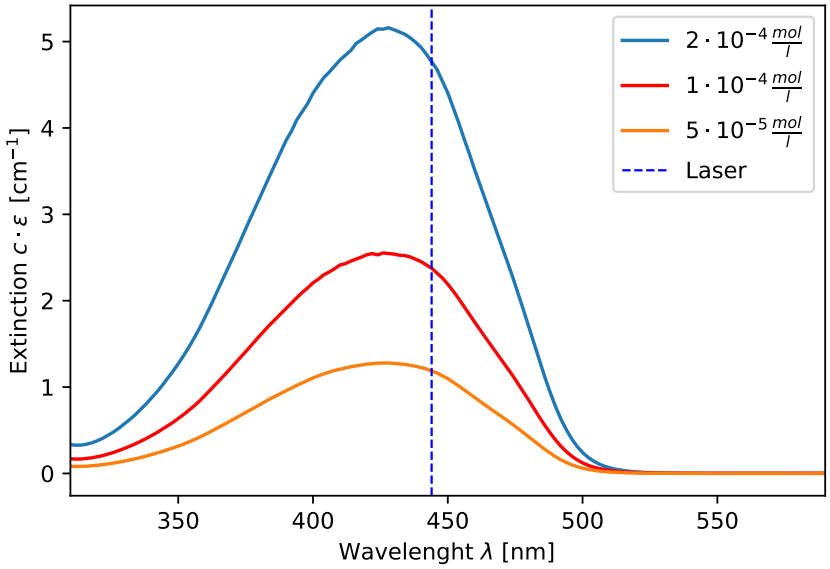

FIGURE 4.10: Absorbance spectra $c \cdot \epsilon(\lambda)$ of tartrazine for three considered concentrations. The wavelength of the lasers is shown as reference and is is a range where the absorption is high.

then absorbed according to the Beer-Lambert law:

$$I(z) = I_0 \cdot 10^{\epsilon \cdot c \cdot z} \tag{4.1}$$

$$\overset{[4.10]}{\Rightarrow} \quad I(1\text{cm}, 10^{-4}\tfrac{\text{mol}}{l}) \approx 0.5\%\, I_0, \tag{4.2}$$

with the tartrazine concentration c, the penetration depth z and the molar attenuation coefficient ϵ. To obtain a reasonable concentration for this purpose, different concentrations were analysed spectroscopically. As expected, a linear increase of the absorbance can be observed and the maximum is in good accordance with the literature value of $\lambda = 430\,\text{nm}$ (Maslowska and Janiak, 1996). With the results of figure [4.10], a concentration of $10^{-4}\frac{\text{mol}}{l}$ was found to be sufficient.

This reduction of the penetration depth of the illumination is crucial to obtain good contrast in the PRIM data. It comes however with the drawback that illumination or observation from below the tank is not possible anymore.

4.2.3 Camera System

The aim to visualize already small concentrations of the tracer particles at the water surface comes with particular requirements concerning the camera system. Basler's compact *acA1920-155um* USB3.0 camera with a *Sony IMX174* CMOS sensor was found to meet those demands. The sensor has a resolution of $1920\,\text{px} \times 1920\,\text{px}$ with a pixel size of $(5.86\,\mu\text{m})^2$, while allowing for a frame rate of up to 164fps with a global shutter. It has a particularly low noise of 6.6e^- and a high signal to noise ratio of typically $SNR = 45.0\,\text{dB}$.

TAMRON 23FM25SP lenses with a focal length of 25 mm were used. With an aperture of $f = 1.4$ this lens is fast enough for this application and has a low distortion of $|DTV| < 0.05\%$.

Two camera systems were mounted on the top window of the large linear tunnel at fetch lengths of $F_1 = 120\,\text{cm}$ and $F_2 = 220\,\text{cm}$. They were positioned at central

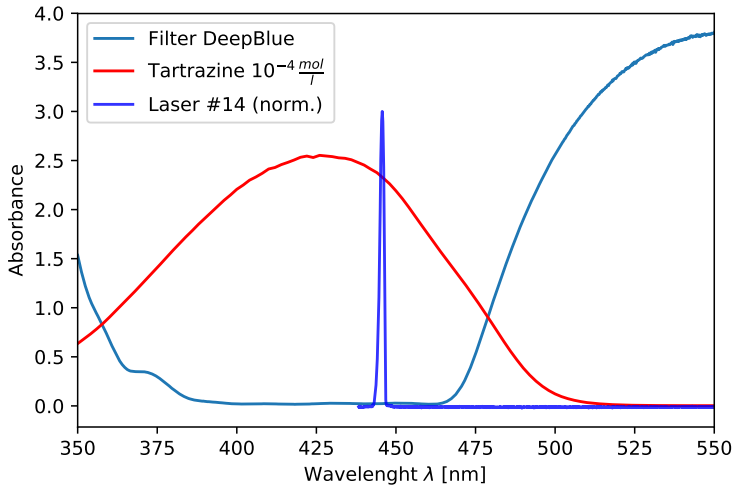

FIGURE 4.11: Combined representation of the absorbance spectrum of the *DeepBlue* filter and tartrazine. The spectrum of laser #14 is added with an normalized intensity of $\equiv 3$ for comparison.

width and directly ontop of the glass to avoid reflections. Therefore, the distance from the water surface was 24 cm (water height of 9 cm). The cameras are triggered together with the light sources via a dual channel function generator and accessed with *heurisko* scripts.

4.2.4 Filter

A *DeepBlue* filter is used in front of the lenses to further suppress unwanted signals. Its measured absorption spectrum in the range of interest is plotted in figure [4.11]. This shows that the laser effectively suppresses wavelength that could potentially penetrate through the absorption dye tartrazine.

As described above, reflected light from the water surface cannot easily be filtered away since the scattered light of the particles has the identical wavelength. Experiments with polarisation filters were conducted but had no positive effect. It is therefore neither possible to discriminate the signals from water surface and tracer particles by polarisation.

4.2.5 Gas Supply

The air-sided reagent is fed into the air volume right after the wind engine (see figure [4.2]) which is more then 6 m before the water segment. The gas in the air volume is therefore well mixed when it reaches the water body so that a homogeneous gas transport can be assumed.

For a controlled reaction, the gas flux is regulated with a *ANALYT-MCT* electronic mass flow controller. The start and endpoint are set with digital time switches. The exact inflow of CO_2 and SO_2 can therewith be regulated easily. To convey small concentrations, the gases were combined with influx of N_2, also controlled by an *ANALYT-MCT*. For HCl, which was not on hand in gas bottles, air can be piped through a wash bottle with 25% p.a. hydrochloric acid solution.This carries off the vapour pressure that is in the gas volume on top of the solution. Estimates for the effectively transported amount of HCl are provided in section 5.2.2.

4.2.6 Vertical Laser Sheet

During early measurements, where the described setup and reagent concentrations were not optimized yet, the tracers was not visible from top view. This is why an alternative optical setup, inspired by the LIF method, was supplementary in use. For a higher sensitivity to the potential appearance of tracer particles, a vertical laser sheet was arranged and recorded from the side. One of the lasers described in section 4.2.1 was used together with cylindric lenses to provide a $\sim 1\,\mathrm{cm}$ wide sheet, stretching in wind direction. This setup was mounted in central position below the transparent bottom of the *Heidelberg Linear Wind-Wave Tunnel*. Through the side window, a *Basler* camera (cf. section 4.2.3) is focused on the sheet in the water-side. Obviously, no tartrazine can be used during these measurements[1] since the laser light would be immediately absorbed. Cloudiness of the water can hereby be investigated by an increasing observed intensity of the laser sheet in the bulk. Tracer particles at the surface lead to high intensities, since they are directly illuminated by the laser.

The laser, and with it the sideways camera, were triggered in a way that they do not interfere with the measurement from top view.

[1] Chronologically, this setup was used before the idea came up to use absorption dye during the measurements.

Chapter 5

Experiments

The precipitation reaction imaging method was optimized over the course of many experiments. This chapter briefly describes the meticulous experimentation that has been done to determine the best suitable chemical system and the respective concentrations. While the experimental difficulties of less successful systems are qualitatively described, focus is set on the silver chloride measurement from which the later discussed results are obtained. Additionally, one preliminary experiment is described that was important for finding the suitable concentrations and provides information about the sedimentation behaviour of the tracer. Section 5.3 describes the surface velocity measurements with glass spheres. Experiments for the BLI and active thermography measurements are not further described since they were conducted by Angelika Klein and Jakob Kunz (functional principle and setup described in sections 3.1.1, 3.1.2 and 4.1.5).

5.1 PRIM with Barium Carbonate and Barium Sulfite

The first experiments were conducted with $BaCl_2$ dissolved in the water body and the gases SO_2 or CO_2 as air-sided reactant, as described in sections 3.2.2 and 3.2.2, respectively.

The slow reaction rate of CO_2 was experimentally confirmed by the observation that the water becomes increasingly cloudy without a visible reaction in the boundary layer. Different concentrations of NaOH in the water body were tried out to counteract this problem. Through the direct chemical reaction of CO_2 with the OH^- ions, the penetration depth is reduced and the transfer rate enhanced as carried out in section 2.4 and 3.2.2. To provide a sufficient amount of reaction partners in the boundary layer, a high pH value $\gtrsim 11$ has to be chosen. This however made the

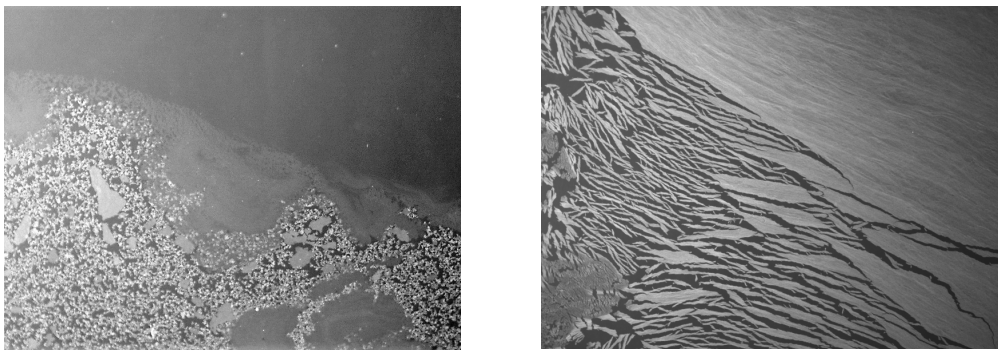

FIGURE 5.1: Accumulation of $BaCO_3$ at the beach during the experiment (*left*, wind top-down) and after the wind is turned off (*right*).

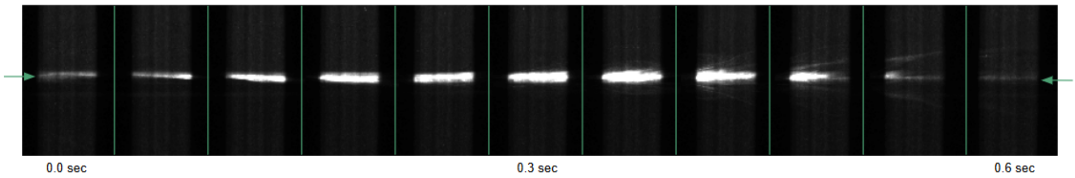

FIGURE 5.2: Laser sheet at the water surface at 11 consecutive time frames over 0.6 s. Arrows mark the interface, above that is the reflection of the water. Bright values indicate scattering at a tracer particle.

reaction very hard to control due to CO_2 concentration in the air and water. Consequently, a strong turbidity in the bulk and an accumulation at the beach was observed, a precipitate at the surface was however hardly visible. Figure [5.1] shows the clustering of $BaCO_3$ at the beach and without the influence of shear stress.

The usage of SO_2 as reaction partner for the dissolved Ba^{2+} ions made it easier to control the gas concentration. The influx of SO_2 reduces the pH value locally in the boundary layer. Even if the pH value in the water bulk is set to be higher than $pK_{a2} = 6.99$ (cf. section 3.2.2), no precipitate can be observed at the surface. For much higher pH values it becomes then however difficult to eliminate the influence of CO_2 on the reaction. Since the pH value can only be measured in the bulk, the conditions are difficult to monitor and control. Therefore, resulting observations can hardly be interpreted and are difficult to reproduce.

5.2 PRIM with Silver Chloride

Due to the described experimental difficulties with the other tracers, the focus was set on the chemical system with $AgNO_3$ dissolved in the water body and controlled influx of HCl gas.

5.2.1 Preliminary: Vertical Laser Sheet

During early experiments, the water was observed to get cloudy without a visible accumulation of tracer particles at the surface. This was due to a non-optimal setup and, as it turned out, an unsuitable gas concentration. Since the previous version for the setup was not sensitive enough to capture the surface signals from top view, an additional setup was implemented (section 4.2.6). This made it possible to find suitable concentrations and validate that the precipitation reaction takes place at the surface.

By observing the concentration of the precipitate vertically, a strong signal right at the interface could be confirmed as a result of correctly dosed gas influx. Figure [5.2] shows a sequence where tracer particles move across the illuminated line at the water surface. In this example, the concentration of Ag^+ ions in the water is $h = 5 \cdot 10^{-4} \frac{\text{mol}}{l}$ and the response is to a pulse of $1200 \frac{\text{ml}}{\text{min}} \approxeq 3 \cdot 10^{-10} \frac{\text{mol}}{\text{s} \cdot \text{cm}^2}$ of HCl gas (cf. calculation below).

Shown in a space-time image like figure [5.3], various "groups" of tracer particles can be identified. Out of the first 60 frames of this image, every sixth is shown in figure [5.2]. These measurements do not provide much information about the surface flow pattern and are therefore not objective of this work. The central conclusion of these measurements are a proof-of-concept for PRIM.

After numerous experiments, the water becomes cloudy and if the wind is turned off, precipitate accumulates homogeneously at the surface. Figure [5.4] shows the

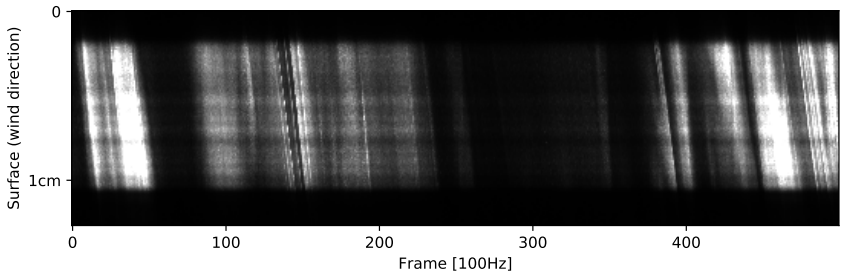

FIGURE 5.3: Space-time (XZ) image at the water surface (Y value marked by arrows in figure [5.2]), with time increasing to the right up to 5 s.

behaviour of the AgCl distribution in the water body for up to 50 h after an experiment. The intensity of the backscattered light within the bulk decreases over time. As expected, sedimentation leads to a decent of many particles, leading to an increase of intensity at the bottom. At the surface, the tracer particles are found to cluster together to form 'AgCl floes' of various sizes. Figure [5.5] shows a clear decline of the mean grey value of the laser sheet at all depth except for the bottom ($z = 9\,\text{cm}$) of the tank. A quantitative analysis of the sedimentation is not possible since because the influence of other effects (change of intensity due to sediment on the bottom, clustering, photosensitivity) cannot be estimated properly.

5.2.2 Exemplary Measurement Series

Several experiments with AgCl were conducted and the setup was improved on the basis of the observations. To make comparisons and interpretations easier, all shown results are obtained from the same measurement series that is shown in table [5.1] and is conducted with the setup described in section 4.2. For every wind condition, it has been waited until the system is in equilibrium. Image data was acquired for 5 minutes with 100Hz at two different fetch length: $F_1 = 120\,\text{cm}, F_2 = 220\,\text{cm}$. In the first30 s at every condition, no gas was added to the system as a comparison and to obtain background images. Then, a flux of $5\frac{l}{\text{min}}$ air was piped through a wash bottle with 25% p.a. hydrochloric acid solution for a duration of 120 s. The recording time of 5 min was enough to observe an end of tracer particles emerging at the surface for every wind condition. Precipitates were visible for a duration of 200 s to 250 s, depending on the wind speed. In between the measurements, the channel was aerated and the analysis bypass was set on to measure pH value and conductivity.

The conversion of motor frequency to u_* is calculated by Friedl (2013) and compared to the friction velocity in the *Aeolotron* in figure [5.6]. The different friction velocities due to the fetch dependency are in the following denoted as $u_{*1} := u_*(F = 120\,\text{cm})$ and $u_{*2} := u_*(F = 220\,\text{cm})$. Conductivity and pH values were measured in the analysis bypass (i. e. water bulk) of the linear tank (cf. figure [4.2]). The gas concentration of HCl in the air volume is difficult to measure. Since it is a strong acid though, the pH value in the water body can be used as a proxy for the amount of Cl^- ions that were dissolved over time. The pH value measurement after every condition, i.e. after every pulse of HCl, is plotted in figure [5.7]. The values of measurements 1-7 systematically underestimate the amount of absorbed HCl because the water is not well mixed and a reasonable error can only be estimated for the first and last data point. These measurements are obtained under better conditions and

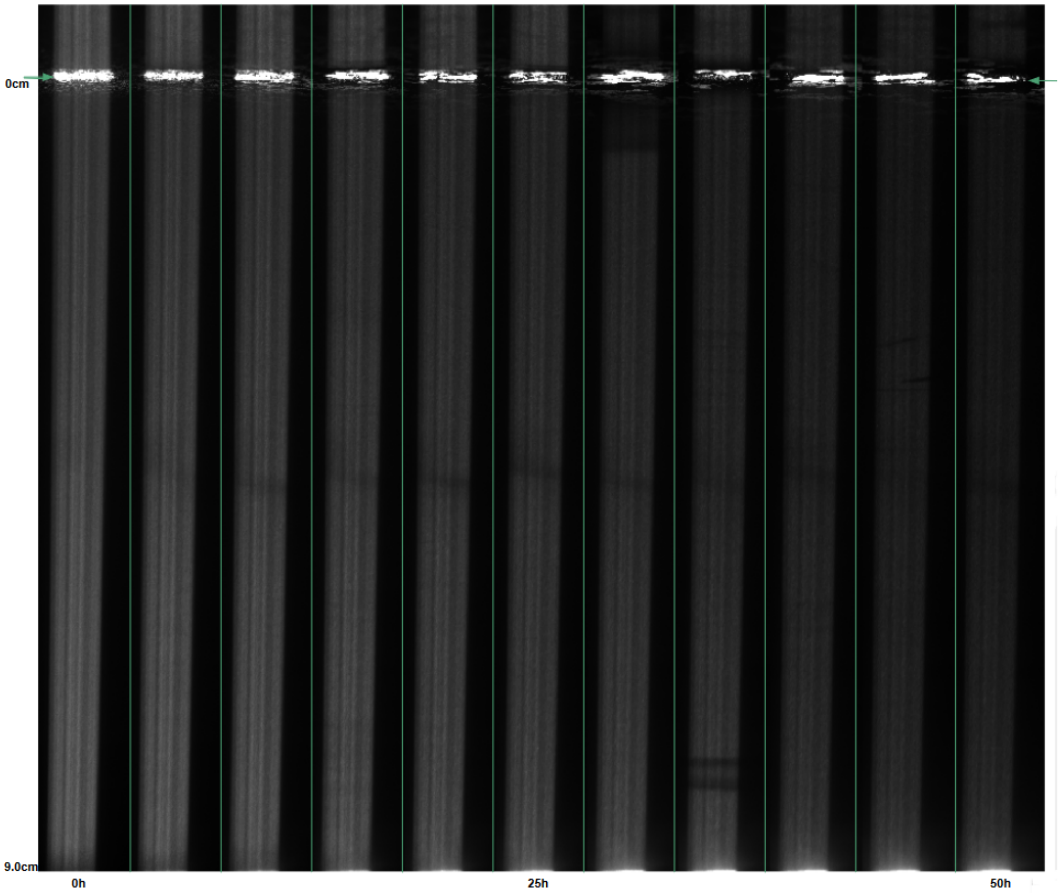

FIGURE 5.4: Vertical concentration profile of the channel's whole depth of 9 cm recorded in steps of 5 h without wind.

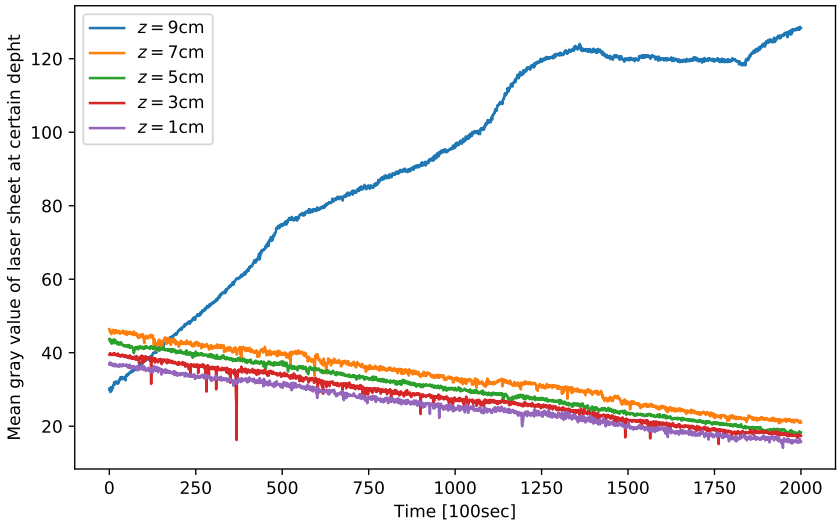

FIGURE 5.5: Average grey value over the wideness of the laser sheet at various depth z (0 cm:= surface) recorded every 100 sec over the course of $\sim$ 55 h.

TABLE 5.1: Measurement of 4th December 2017, with a concentration of silver nitrate: $c_{AgNO_3} = 10^{-3}\frac{mol}{l}$, tartrazine: $c_{tar} = 10^{-4}\frac{mol}{l}$, constant values for $T_{water} = 22.1°C$, $T_{air,1} = 20.7°C$, $T_{air,2} = 20.6°C$, $p = 1018\,hPa$.

Freq. [Hz]	time t [min]	u_{*1} [cm/s]	u_{*2} [cm/s]	pH value	Cond. [µS/cm]
-	0	-	-	5.50	182
5	0-5	.208 ±10%	.208 ±10%	4.81	169
7.5	12-17	.278 ±10%	.347 ±10%	4.80	171
10	25-30	.382 ±10%	.452 ±10%	4.64	160
12.5	37-42	.486 ±10%	.556 ±10%	4.66	158
15	47-52	.590 ±10%	.764 ±10%	4.55	164
17.5	57-62	.764 ±10%	.973 ±10%	4.46	161
20	69-73.5	1.08 ±10%	1.25 ±10%	4.15	158
22.5	87-92	1.32 ±10%	1.49 ±10%	4.02	165

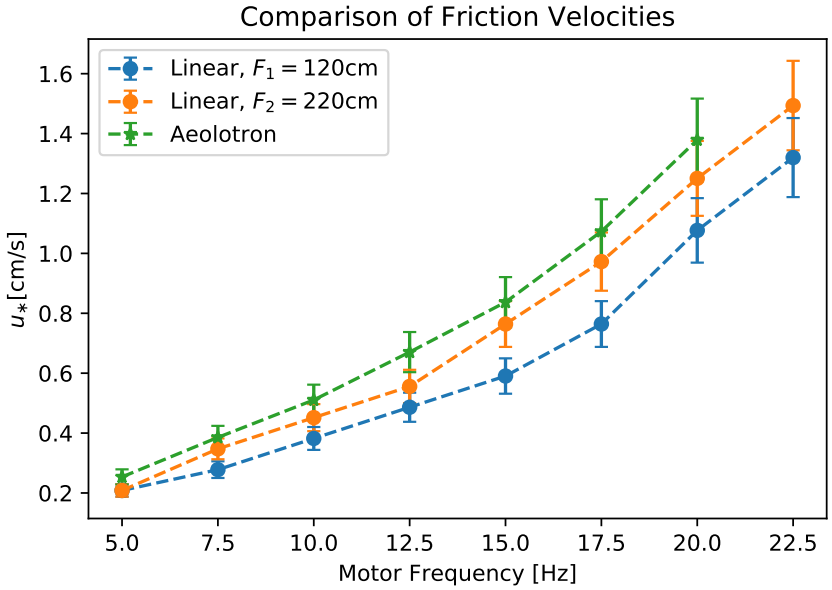

FIGURE 5.6: Friction velocities u_* for the used motor frequencies at *Aeolotron* and the measuring conditions in the *Heidelberg Linear Wind-Wave Tunnel*.

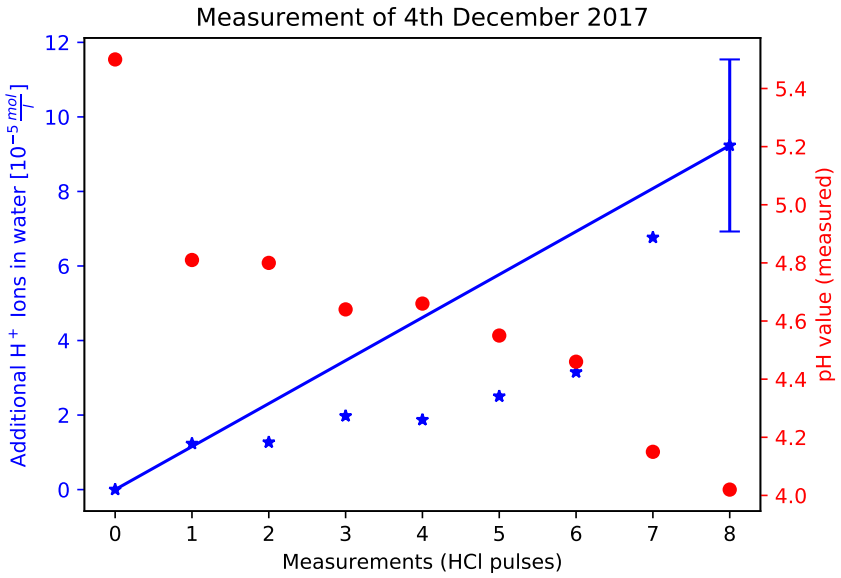

FIGURE 5.7: Plot of the measured pH values in the analysis bypass and the resultant mean ion concentration.

can be used to estimate the amount n_{HCl} per pulse and with that the gas flux:

$$
\begin{aligned}
&\text{pH: } (5.50 \pm 0.10) \rightarrow (4.02 \pm 0.10) && \text{with } V_w = 130l \\
\Rightarrow\quad & n_{\mathrm{HCl}} = (1.2 \pm 25\%) \cdot 10^{-2}\mathrm{mol} && \text{within } t = 8 \cdot (230 \pm 20)\mathrm{s} \\
\Rightarrow\quad & \frac{n_{\mathrm{HCl}}}{t} = (6.5 \pm 35\%) \cdot 10^{-6} \tfrac{\mathrm{mol}}{\mathrm{s}} && \text{with } A_w = 1.28\mathrm{m}^2 \\
\Rightarrow\quad & j_{\mathrm{HCl}} = (5.0 \pm 35\%) \cdot 10^{-10} \tfrac{\mathrm{mol}}{\mathrm{s \cdot cm}^2} \\
\Rightarrow\quad & \Delta c_w = \frac{j_{\mathrm{HCl}}}{k_w} \approx \frac{5 \cdot 10^{-10} \frac{\mathrm{mol}}{\mathrm{s \cdot cm}^2}}{5 \frac{\mathrm{cm}}{\mathrm{h}}} = (3.6 \pm 50\%) \cdot 10^{-7} \tfrac{\mathrm{mol}}{\mathrm{cm}^3}
\end{aligned}
$$

Estimates from other experiments and theoretical limits derived from the vapour pressure of the HCl solution affirm the result for n_{HCl} within its error margin. The volume and surface area of the water V_w, A_w are given by the tank geometry, k_w is estimated through typical transfer velocity measurements (cf. Friedl, 2013) but is in fact expected to be even higher because of the enhancement due to the chemical reaction (compare equation (2.71)). This gas flux was empirically found to lead to the best experimental results. A lower gas concentration leads to less tracer particles, making it much harder to capture them on the image sensor. Below a the critical concentration of $[\mathrm{Ag}^+] \cdot [\mathrm{Cl}^-] = 1.77 \times 10^{-10}$, given by the solubility product (cf. section 3.2.2), no precipitate can be seen at all. If the influx of HCl becomes however much bigger, the Ag^+ ions in the boundary layer are used up and the Cl^- ions do not have a reaction partner at the interface. According to the preliminary considerations in section 2.4, the reaction front moves away from the surface to larger depth[1]. Precipitate that forms below the water interface is turbulently transported to the bulk and become invisible due to the use of tartrazine (cf. section 4.2.2). The gas influx used in this experiments is chosen so that the maximal amount of tracer particles is observable at the water surface.

[1] In fact, the calculation for charged particles is more complicated than suggested in section 2.4 since the charge has to be conserved at all depth. Hence, the concentration profiles of the spectator ions also have to be considered. This qualitative statements remains however true.

TABLE 5.2: Main experiments to determine the surface velocity

Date	Size (Amount [g])	Freq. [Hz]	u_* [$\frac{cm}{s}$]	u_b [$\frac{cm}{s}$]
10.01.18	70 µm (2.75) & 1 mm–2 mm (2.5)	5	0.25 ± 0.02	1.69 ± 0.14
10.01.18	70 µm (2.75) & 1 mm–2 mm (2.5)	7.5	0.38 ± 0.02	2.74 ± 0.11
10.01.18	70 µm (2.75) & 1 mm–2 mm (2.5)	10	0.51 ± 0.04	3.81 ± 0.22
10.01.18	70 µm (2.75) & 1 mm–2 mm (2.5)	12.5	0.67 ± 0.05	5.25 ± 0.18
10.01.18	70 µm (2.75) & 1 mm–2 mm (2.5)	15	0.83 ± 0.06	6.67 ± 0.19
27.02.18	1 mm–2 mm (4)	10	0.51 ± 0.04	3.81 ± 0.22
27.02.18	+ 0.5 mm–1 mm (2)	10	0.51 ± 0.04	3.81 ± 0.22
27.02.18	+ 0.25 mm–0.5 mm (1.5)	10	0.51 ± 0.04	3.81 ± 0.22
27.02.18	+ 70 µm (1)	10	0.51 ± 0.04	3.81 ± 0.22
27.02.18	+ 0.25 mm–0.5 mm (5)	10	0.51 ± 0.04	3.81 ± 0.22

5.3 Macroscopic Flow Tracer

Glass spheres of various sizes were used as a further comparison to the flow patterns observed with PRIM. Within the course of preliminary experiments they were found to be suitable flow tracer to determine the surface velocity. The experiments were conducted in the *Aeolotron* since its annular geometry is well suited for these experiments. Broken glass bubbles were sorted out prior to all measurements through flotation and filtering by buoyancy. A frame rate of 400 Hz was found to be sufficient to track the individual particles, except for the highest wind condition where it was chosen to be 800 Hz.

The two experiments that were used for the determination of the surface velocity are shown in table [5.2]. The plus (in column *size*) indicates the successive adding of tracer bubbles. It was waited for every condition until the momentum balance reaches equilibrium and an additional measurement was conducted after turning off the wind turbines, respectively. While the measurements at 10.01.18 aimed to observe the flow pattern and the surface velocity at various wind conditions, focus was set on the different behaviour of the tracer depending on size at 27.02.18.

With larger size of the glass bubbles they show a stronger tendency to cluster together at low wind speed conditions. The influence of the *Aeolotron's* secondary flow fields on the tracer is also found to increase with size. Larger glass bubbles are found to accumulate at the outer wall for low, and at the inner wall for high wind speeds. For this reason, in the second measurement series (27.02.18) only one intermediate wind condition was investigated.

No meaningful measurements could be performed at wind conditions above 15 Hz. Turbulent wave breaking in that regime was observed to transport a significant amount of glass bubbles towards the bulk. Since no depth information about the tracer can be obtained, this distorts the measurement.

Chapter 6

Image Processing

During the optimization of the PRIM technique it could be achieved that direct reflections are avoided, signals from the water bulk are blocked out and sufficient amounts of tracer particles are produced directly at the interface. This chapter describes the remaining difficulties in the image data and provides a short overview of approaches on how to overcome them in post-processing. The algorithm used for the tracking of macroscopic tracer particles at the surface is briefly described.

6.1 Calibration and Conventions

The image data for active thermography and BLI was provided and already calibrated according to Kräuter (2015) and Kunz (2017), respectively. Throughout this work, BLI images are displayed in the colormap *bone* (black to white, blue tone), thermography in *afmhot* (black to white, red tone) as seen in figure [7.6]. The two methods are adjusted to observe the same surface patch simultaneously of size $(17.7 \times 20.7)\mathrm{cm}^2$ with a resolution of $0.23\,\mathrm{mm/px}$.

A calibration of the PRIM imagery to the concentration of the precipitate was unfeasible due to brightness modulations by the wave field (see below). The absolute grey values have therefore no significance and the value for M in equation (6.2) is chosen for each invested batch individually to obtain good contrast. The colormap *jet* (blue to red, see figure [6.2]) and the colorbar is later omitted for convenience. A chessboard calibration of the optical setup was carried out and the FOV is $(7.3 \times 11.7)\mathrm{cm}^2$ with a resolution of $61\,\mu\mathrm{m/px}$. The telecentric ISG setup that was used for the particle tracking observes a surface patch of $(13.6 \times 21.7)\mathrm{cm}^2$ with a resolution of $113\,\mu\mathrm{m/px}$.

The axis label of the images show the size of the surface patch for better comparability. Unless otherwise stated, the wind direction in the images is from left to right.

6.2 PRIM Data

It was great effort taken in optimizing the experimental setup for data acquisition. The already elaborated difficult conditions however partially entailed non-optimal image results. Even tough direct reflections could be avoided by a suitable choice of the illumination system, the structures of interest are superimposed with light patterns from the waves. With higher wind speeds, intensity fluctuations occur due shadowing and lensing effects at the emerging water waves.

First aim of the digital post-processing of the data is to correct for inhomogeneous illumination. To be able to measure continuously for extended periods of

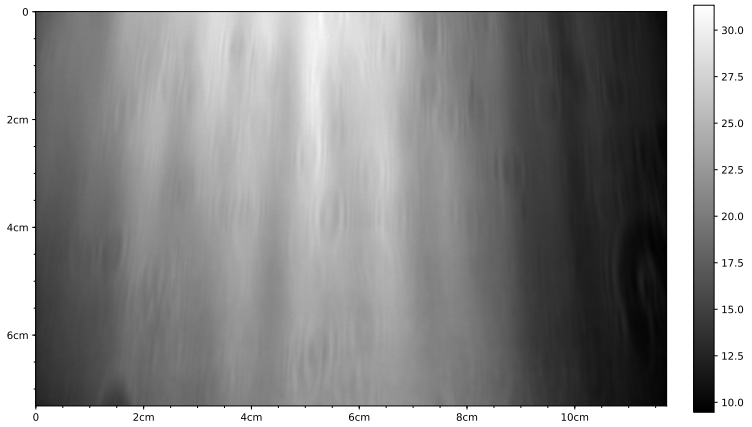

FIGURE 6.1: Background image for the 220 cm fetch, $u_{*2} = 0.97\,\frac{\text{cm}}{\text{s}}$.

time (usually 5 min, cf. section 5.2.2) and not overheat the lasers, their duty cycle has to be considered for the length of exposure.

6.2.1 Background Correction

The background image is obtained for both cameras and for every wind condition separately. Before tracer gas was induced, at least 2500 images were recorded in equilibrium. Their mean image, as for example figure [6.1], is used as reference for this condition. Reasons for variations in the background images are a growing number of tracer particles in the water body, potential wavelength shifts[1] or intensity fluctuations of the laser light due to heating, and changing diffraction patterns due to the wave spectrum. Figure [6.1] shows ring-shaped structures due to inhomogeneities of the laser. Since the water surface is moving, it cannot fully be corrected for their influence and they also appear in later images.

The fixed pattern noise of the *Basler* cameras (cf. section 4.2.3) was found to be negligible and does not need to be compensated for. The background correction is done by dividing the image data of one condition **G** by the respective reference image **R**:

$$\mathbf{G'} = c \cdot \frac{\mathbf{G}}{\mathbf{R}'}, \tag{6.1}$$

while the factor c is used to transform the image back on the original integer range.

6.2.2 Contrast Modifications

A natural choice for c would be $c_0 := 255/\max(\frac{\mathbf{G}}{\mathbf{R}})$, for `uint8` with $q = 255$ as maximum grey value. Setting it lower leads to underexposed histograms and higher to information loss. In view of the image data, highest grey values are not obtained by the signals of interest but rather due to reflections of waves. Therefore, no actual information is lost if an image saturates in these regions. With this motivation,

[1] This has to be considered because of the wavelength dependent absorption of tartrazine and the filter.

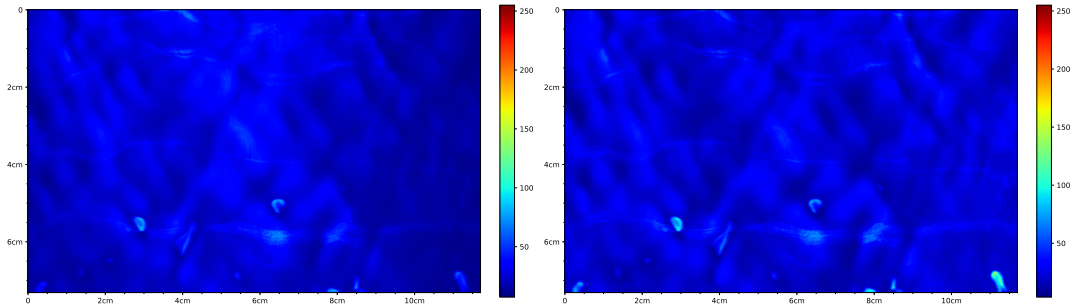

(A) Original Image

(B) Background corrected

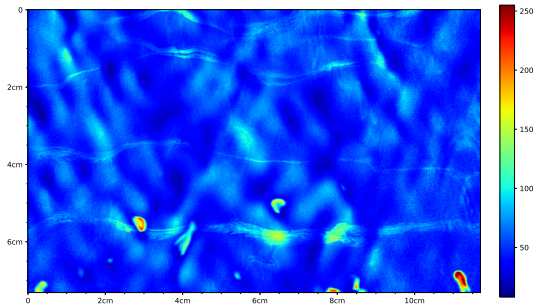

(C) $M \equiv 5$, so that $5 \cdot \text{median} \equiv 255$

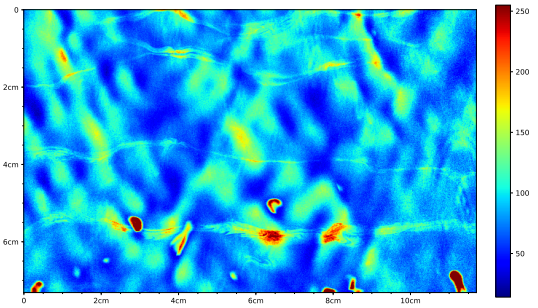

(D) $M \equiv 3$, so that $3 \cdot \text{median} \equiv 255$

FIGURE 6.2: Correction of the original image with the reference image shown in figure [6.1]. Of interest are the streaky structures.

equation (6.1) is modified to:

$$\mathbf{G'}(M) := \frac{255}{M \cdot \text{median}(\frac{\mathbf{G}}{\mathbf{R}})} \cdot \left(\frac{\mathbf{G}}{\mathbf{R}} - \min(\frac{\mathbf{G}}{\mathbf{R}}) \right), \tag{6.2}$$

where M determines the multitude of the median value that is projected on the maximal grey value. The subtractive term is introduced to make sure that the whole range $(0 - 255)$ is used. Equation 6.2 is effectively stretching the image contrast by setting the range of interest to the maximal grey value range. To comparisons within a batch of images $\mathbf{B}$, min or median$(\frac{\mathbf{B}}{\mathbf{R}})$ was used for consistency.

Figure [6.2] shows the described approaches: In [6.2b], the structure in the bottom right, where the illumination was lower, can be seen way better. No pixel in the image has a value larger than $q = 121$ because apparently a reflection in another image of the batch set the maximum value. By choosing the maximum to be $5\times$median, this can be avoided and the objects of interest are well visible. A lower value for M on the other hand leads in [6.2d] a part of the streak in saturation and is therefore not desirable.

This procedure is a linear mapping of the grey values to a smaller interval and sets everything above the chosen threshold to the maximum. They can be implemented efficiently in form of a lookup-table (LUT). Obviously, contrast enhancement in the form of stretching the range does not add new information to the image or improve its quality.The improved visual impression allows however for better qualitative comparison.

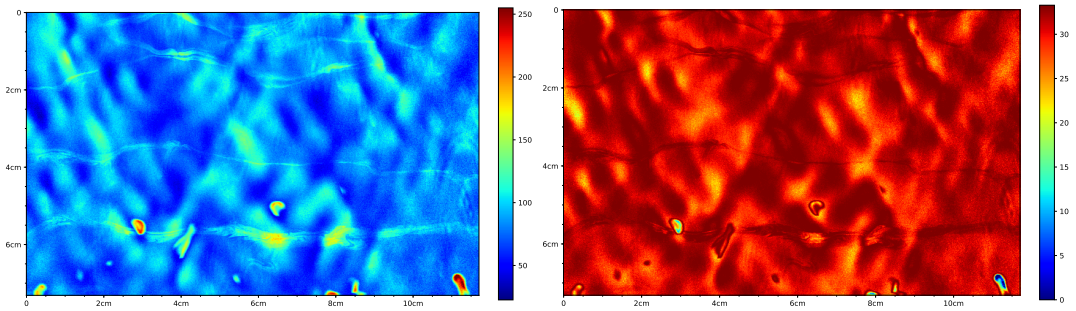

(A) Result of $\gamma = 0.7$ transform to [6.2c] (B) Difference image of (A) and [6.2c].

FIGURE 6.3: Influence of the *gamma transformation* on the data

Additional compression of grey values can be achieved through applying the so-called *gamma transformation*:

$$q' = \frac{255}{255^{\gamma}} q^{\gamma}. \tag{6.3}$$

This point operation has again the form $q \in [0, 255] \rightarrow [0, 255]$ and leads to a enhanced dynamic range while either compressing high (choose $\gamma < 1$) or low ($\gamma > 1$) grey values. An example for this transformation with the γ-value set to $\gamma = 0.7$ is provided in figure [6.3]. The difference image shows that indeed the structures of interest are amplified. The intensity fluctuation due to the waves is however also enhanced so that no significant improvement of the visual impression can be achieved. A wide variation of further LUTs were considered but neither improved the image quality and are therefore not shown.

6.2.3 Pattern Analysis

Different approaches were considered to quantify the similarities and differences between the observations of PRIM and the other methods. If the same surface patch is simultaneously observed, the correlation in different layers of the Laplacian pyramid can be measured (Kräuter, 2015). It was however not possible to realize parallel measurements of PRIM with one of the other visualization techniques within the scope of this thesis (cf. section 8.2). Therefore, a meaningful universal measure is necessary for quantitative comparison.

The reference value typically used in the literature is the streak spacing, described in section 2.5.4. This however calls for a full segmentation of the image data, for example classifying each pixel as *streak* or *no streak*. Considering the quality of the tracer signal obtained with PRIM (e.g. figure [6.2]), it is obvious that no simple threshold for the grey values can be used. The presumably most suitable features to distinguish streaks from the background are their expansion in flow direction and the lower velocity compared to the wave signals. Numerous efforts of model based image processing techniques and investigations of the local orientation using the structure tensor were unsuccessful in filtering these structures reliably. Providing manual labels within the framework of the *Interactive learning and segmentation toolkit* (*Ilastik*, Sommer et al., 2011) did neither provide sufficient results.

A different approach is the detection of peaks in image lines vertical to the wind direction. The continuous wavelet-based algorithm (cf. Yang, He, and Yu, 2009) is used to determine the relative maxima for multiple length scales. Locations that

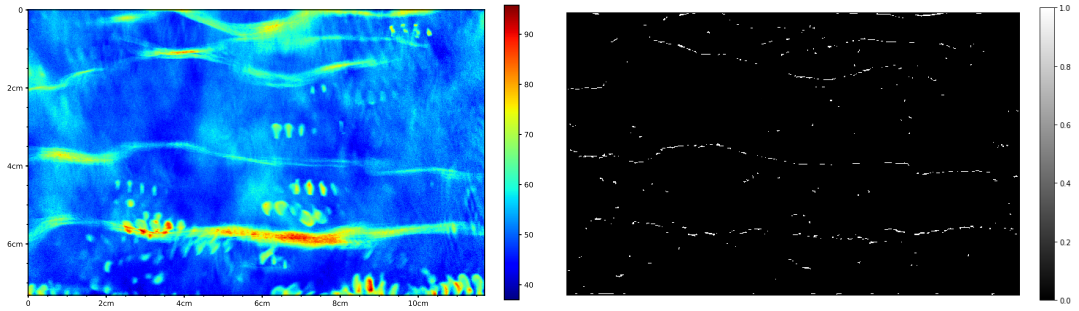

FIGURE 6.4: Time averaged image around [6.2c] over 10 frames $\widehat{=}$0.1 s (*left*) and binary result of a streak finding algorithm (*right*).

repeatedly occur with a sufficient SNR are included in a binary image. Suitable morphological operations are applied that favour elongated structures in wind direction. The influence of the waves is to some extend reduced by applying the algorithm on an average image of multiple consecutive frames. The result for one sample image is shown in figure [6.4] and is also clearly unfit to determine the streak spacing reliably.

Consequently, no algorithm could be found that would provide useful quantitative measures to compare the established methods with the separately recorded PRIM data. Significant improvements of the method, e.g. in the form of fluorescent tracer particles (cf. section 8.2), are necessary to further improve the quality of the image data.

6.3 Surface Tracking

Glass bubbles of various sizes from 70 µm to 2 mm were seeded on the water surface as described in section 3.3 and 5.3. In contrast to the commonly used particle image velocimetry (PIV) approaches, the experimental setup (cf. section 4.1.4) allows to track particles individually (cf. Engelmann et al., 1999). This has the big advantage that the trajectories and velocities of the particles can be further investigated.

The images were preprocessed by performing a flat-field calibration to correct for the fixed pattern noise of the camera $\mathbf{D}$, and for inhomogeneities in the illumination:

$$\mathbf{G'} = c \cdot \frac{\mathbf{G} - \mathbf{D}}{\mathbf{F} - \mathbf{D}}. \tag{6.4}$$

The image $\mathbf{F}$ was obtained by averaging multiple images of the resting water surface while the dark image $\mathbf{D}$ is recorded with closed lens.

The individual particles in the image were located by using an implementation of the Crocker-Grier centroid-finding algorithm (Allan et al., 2015; Crocker and Grier, 1996). The image is bandpass filtered and a threshold for pixels of candidate particle locations of being in the upper 64th percentile of brightness is applied. The particle location is first assigned to the brightest pixel within the neighbourhood and further refined by calculating the brightness-weighted centroid of the pixels. By investigating the histograms of the decimal part of the locations, the subpixel accuracy for this application was found to give reasonable results for the provided mask size of 11-15 (depending on particle size). Spurious particles are filtered by a suitable value (depending on size) for their total brightness. Figure [6.5a] shows the located particles of size $\sim$0.5 mm in a single frame. The locating is done for every frame individually, providing a dataframe with the features of all found particles.

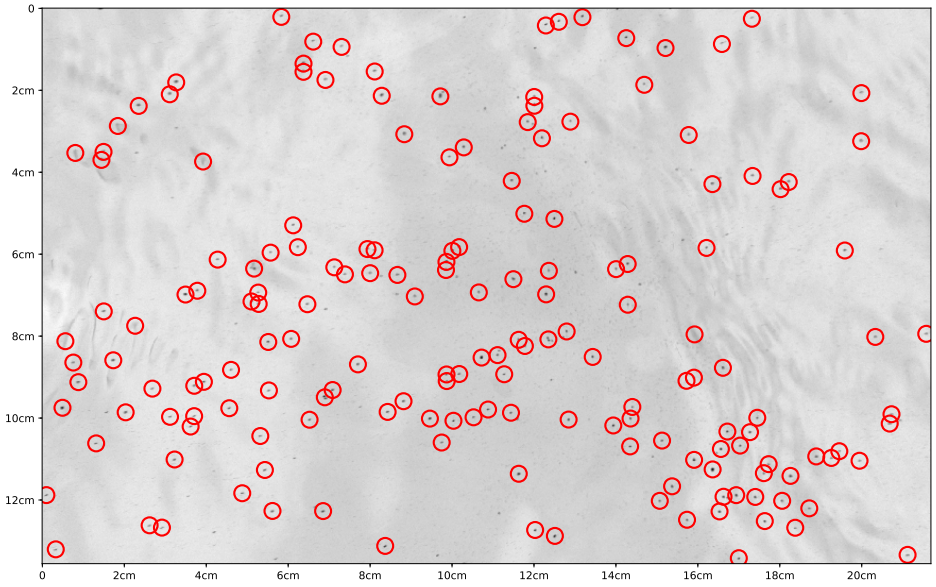

(A) Size filtered annotations in background corrected frame.

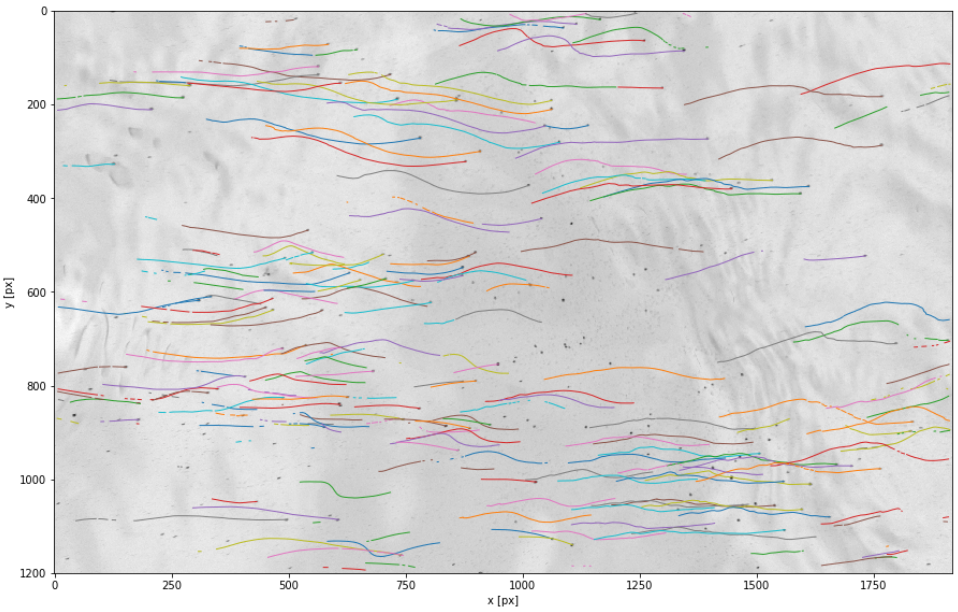

(B) Filtered trajectories of tracked glass bubbles up to the frame shown above.

FIGURE 6.5: Illustration of the steps for the PTV approach for glass bubbles of size ∼0.5 mm.

The features are then linked into particle trajectories. This is done by specifying a maximal displacement d (set to 3-7), quantifying the number of pixels a particle can travel between frames, and a memory parameter m (set to 3), allowing a particle to be missed for a certain number of frames. Each particle is accordingly assigned an ID that can be used to display its trajectory. Only trajectories that last for more than a certain number of frames n (chosen to be 30-50, depending on the statistics) are considered. Particles with a high eccentricity (> 0.3) and a large radius compared to their total brightness (out of focus) are also discarded. Figure [6.5b] shows the trajectories of a batch of 150 frames, superimposed with the last image.

The trajectories can then be used to calculate the overall drift from one frame to the next one, as well as to determine the velocity of individual particles. Size and total brightness are used to match the detected particles with the sizes of the actual glass bubbles. The choice of the parameters d, m, n has potential effect on the particle statistic and can therefore influence the results.

Chapter 7

Results and Discussion

The new visualization method allows for novel insights in the transport and flow processes at the water surface and their dependency on the Schmidt number. This chapter provides image data obtained with the precipitation reaction imaging method and compares the results with existing visualization techniques. Although the presented observations are all taken from the same series of experiments, the described behaviour was found repeatedly and carefully checked for reproducibility. The experimental findings are structured according to increasing wind speed and are interpreted and discussed together, respectively. Results of the surface tracking approach with macroscopic tracers are presented in the last section. They show that the usage of 70 µm glass spheres is a suitable tool to determine the surface velocity and opens up new possibilities to investigate the local momentum transfer.

7.1 Low Wind Regime

Tracer particles resulting from the precipitation reaction can be used as a flow tracer at wind speeds where turbulent surface renewal events are not yet expected. Other visualization techniques do not reveal information for low wind, low fetch conditions as further discussed in section 7.3. With the newly developed method however, wind induced flow structures can be analysed in this regime already.

With a homogeneous gas transfer across the interface, the initial expectation for the PRIM method was a layer of uniformly distributed tracer particles at the water surface. In fact, small and randomly scattered regions can be identified right after the onset of HCl gas. They become more numerous with time as seen in figure [7.1] after 1 min at low fetch length. The pattern of small regions where the precipitation reaction occurs becomes therefore denser.

For the identical second setup at 1 m additional fetch, the tracer signal does not appear to be random anymore but is shaped by macroscopic flow patterns. In the very low wind regime, no waves are present and the flow is solely shear induced. The observed patterns are therefore caused by shear turbulence alone. The shape shown in figure [7.2] is consistent with the forming of "overlapping laminae with a headtail structure" described by Handler, Smith, and Leighton (2001). Typical *fish-scales* observed in infrared images however appear more numerous and only for larger wind speed or fetch length. The typically measured streak spacing of $l^+ = 100$, described in section 2.5.4, leads to an expected characteristic length scale of $l = 4.24\,\mathrm{cm}$. This is indicated with the black bar in figure [7.2] at time $t \equiv 3.6\,\mathrm{s}$ and is consistent with the data. It seems however hardly possible to find objective criteria to determine a clearly defined spacing in this case.

The origin of the point like structures is not yet clear. An explanatory attempt is the tendency of the tracer particles to cluster together, which was already observed under the electron microscope (cf. section 3.2.2, appendix A). It is also possible that

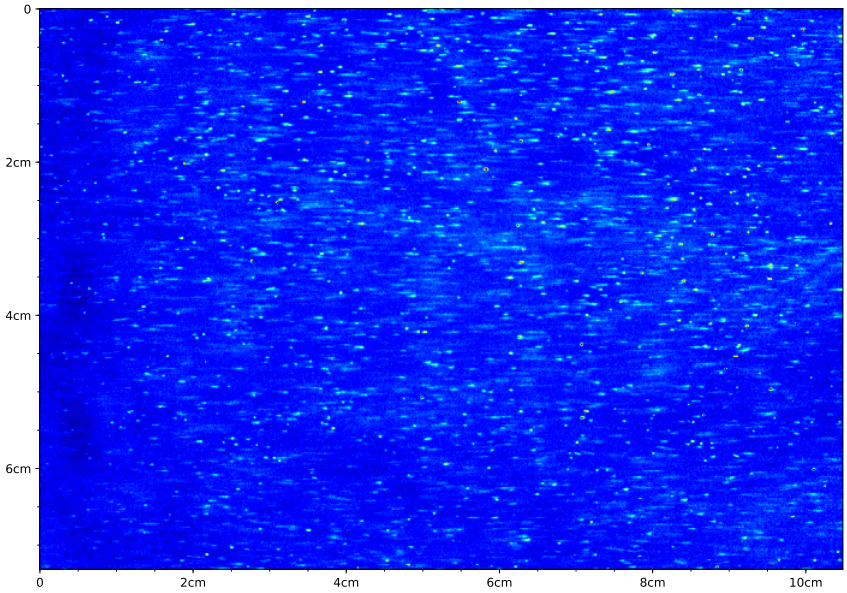

FIGURE 7.1: Surface pattern at 120 cm fetch with minimal wind speed $u_{*1} = 0.21\ \frac{\text{cm}}{\text{s}}$ after 60 s. Point-like structures indicate gas transfer.

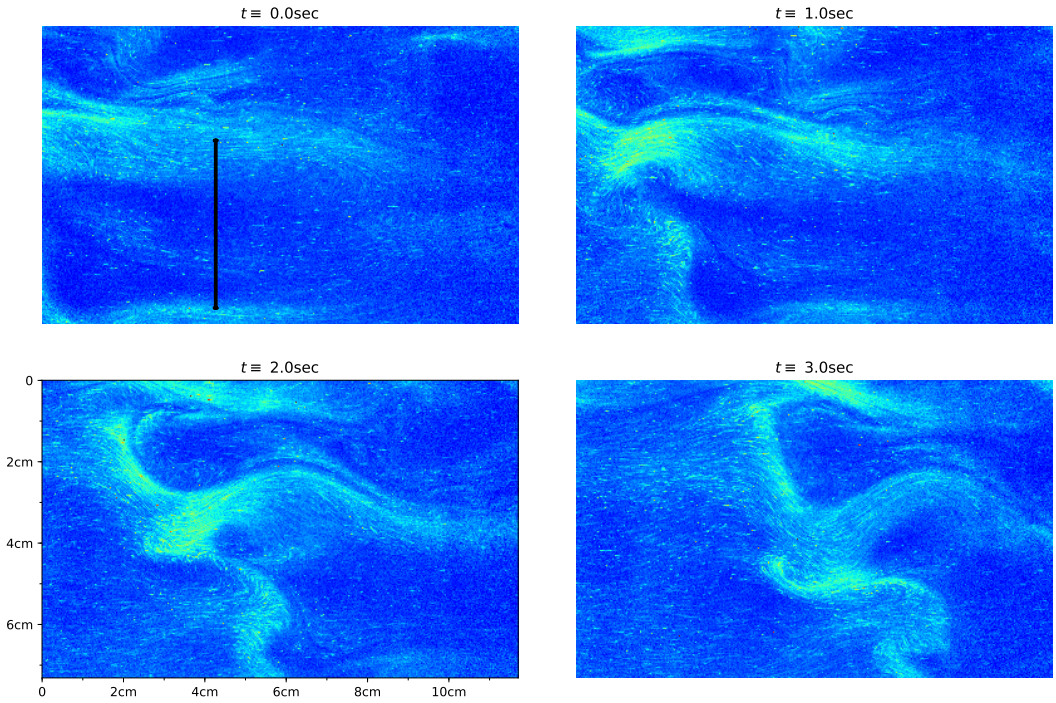

FIGURE 7.2: Same low wind conditions at larger fetch length of $F_2 = 220$ cm, where $t \equiv 0$ is set to 1 min after the onset of gas influx.

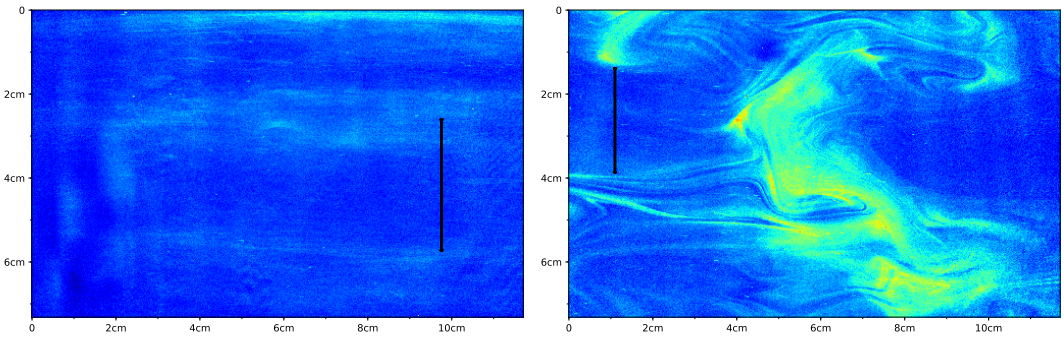

(A) $u_{*1} = 0.28\,\frac{\text{cm}}{\text{s}} \Rightarrow l^{100} = 3.20\,\text{cm}$ (B) $u_{*2} = 0.35\,\frac{\text{cm}}{\text{s}} \Rightarrow l^{100} = 2.56\,\text{cm}$

FIGURE 7.3: Comparison of the different fetch length for 7.5 Hz motor frequency.

the –very small but nonetheless present– threshold for the precipitation reaction due to the solubility product is only exceeded locally. Further investigations using an alternative chemical system with a much smaller solubility (e.g. AgBr, see section 8.2) are necessary to make further statements. Whereas they can still be identified at the second lowest wind condition in figure [7.3], they smear out and fully adapt to the flow field at a higher wind speed. Here the convergence strength at the surface is already sufficient to arrange the tracer in streaky flow patterns. This shows that the tracers' inclination towards clustering is not a dominant effect.

7.2 Fetch Dependency

At low fetch in figure [7.3a], regions of higher concentration are observed that remain parallel over time. The distance between the laminar structures is again in good agreement with the expected streak spacing for shear induced flow patterns. Figure [7.3b] shows that if the wind acts on the surface over a longer distance, more complex patterns evolve.

Choosing the wind speed slightly higher, so that the friction velocity at low fetch is about as high as it was at a larger fetch seen before, leads to the observations in figure [7.4]. The streaks become more distinct but the overall structure remains the same. Slight variations and small, turbulent outbreaks are observed but a clearly defined structure is preserved. A similar development is found by comparing the wind speeds at larger fetch length. Figure [7.5] shows the temporal evolution of the flow pattern that is changing on a smaller timescale due to the increased surface velocity. The spatial extent of the structures shrinks in accordance with the smaller l^{100}.

The clear differences between figures [7.3] and [7.4] for similar friction velocities shows a heavy influence of the fetch length on the flow pattern for small winds. The data suggests that the overall flow structure in this regime is determined by the fetch. For a given fetch length, a higher u_* intensifies the observed patterns. The convergence strength at the surface increases, pushing the tracer particles closer together. Consequently, the observed streaks at low fetch become more pronounced and the stretches of particles at larger fetch become narrower and more distinct.

A potential fetch dependency can be attributed to the method itself. Since tracer particles remain at the surface and are transported to larger fetch length, they are adding to the particles that form there. It can however be assumed that the tracer has

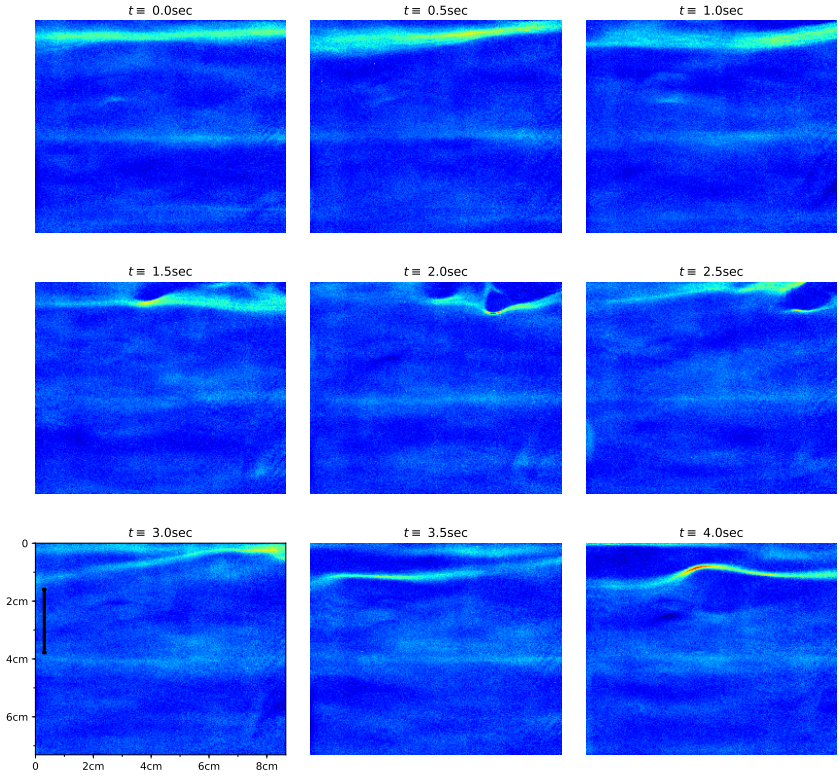

FIGURE 7.4: For $u_{*1} = 0.38\ \frac{\text{cm}}{\text{s}}$, streaks at low fetch are very similar to figure [7.3a] but begin to become unstable.

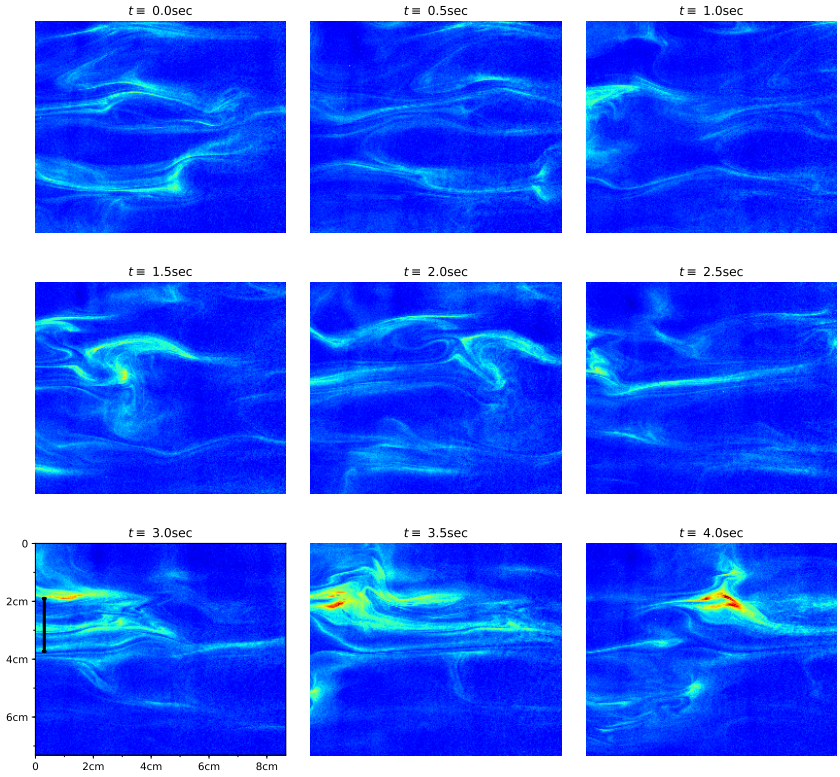

FIGURE 7.5: Time evolution of a flow pattern with $u_{*2} = 0.45\ \frac{\text{cm}}{\text{s}}$ that is similar to figure [7.3b].

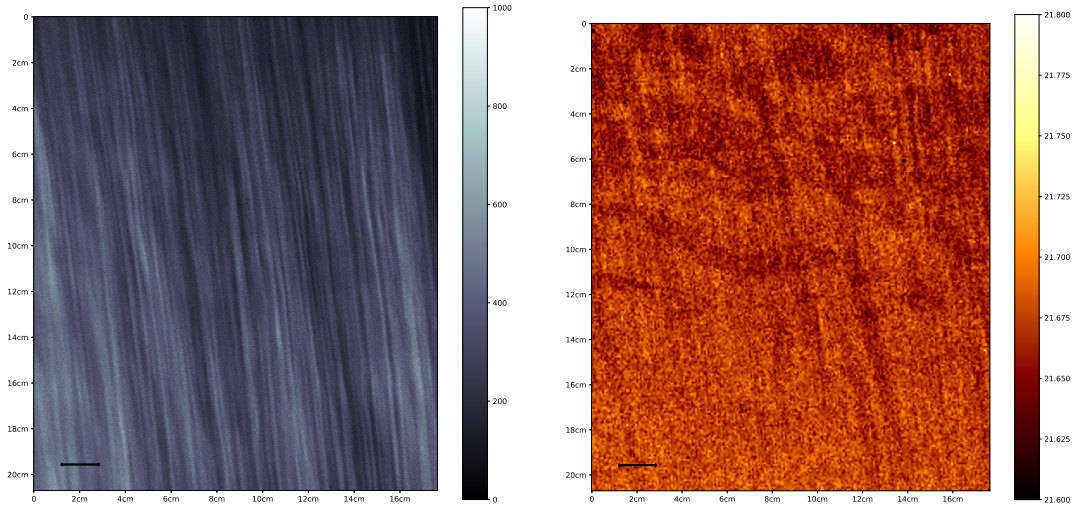

FIGURE 7.6: BLI (*left*) and active thermography (*right*, dark pattern in upper half is due to reflections) images in with 2 m fetch and $u_* = 0.51 \frac{\text{cm}}{\text{s}} \Rightarrow l^{100} = 1.74\,\text{cm}$. Wind blows from the bottom up.

no influence on the flow and instantly adapts to it upon emergence. Consequently, the intrinsic fetch dependency of the method reduces to a larger tracer density for higher fetch length. It can thus be expected that the observed flow pattern is not influenced by the method.

7.3 Schmidt Number Dependency

The established visualization methods, BLI and thermography, also aim to make flow and transport processes visible, but observe other physical properties. Bright regions in BLI (section 3.1.2) imagery show a compression of the boundary layer to higher thickness. Following equation (2.21), this leads to a locally lower transfer velocity. With active thermography (section 3.1.1), intensities are directly translated to temperature. Low values indicate up-welling water from the colder bulk and bright regions show where the heat influx is not as efficiently transported downwards. The tracer particles observed in PRIM follow the convergence zones at the surface, just like glass bubbles. Consequently, a higher tracer density is associated with a thicker boundary layer in BLI and higher temperatures in thermography. Even though the grey values for the different methods do not show the same quantity, they are nonetheless visualizing the same underlying structures.

The main difference between the techniques is the Schmidt number of the tracer, as described in section 2.3. Resulting differences in the observations are analysed in detail.

Sensitivity

In the low wind, low fetch regime, no meaningful comparison between the introduced visualization methods can be done, since neither in thermography nor in BLI do turbulent structures become apparent. Figure [7.6] shows the two methods observing the same surface patch simultaneously at a fetch length of 2 m. The friction velocity in these images is higher than in all conditions of the previously shown PRIM data. Whereas the flow appears laminar in figure [7.6], images under similar

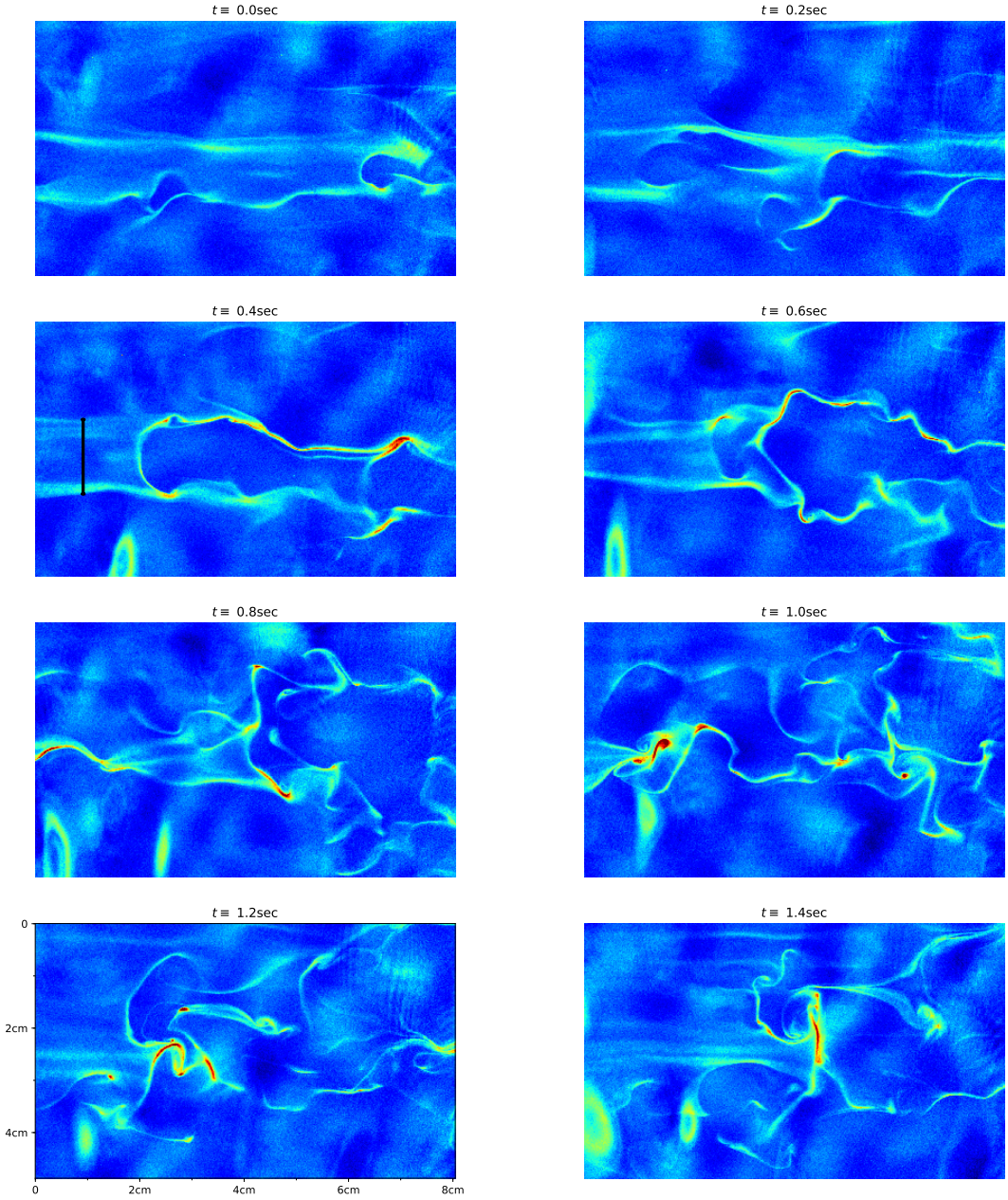

FIGURE 7.7: Turbulent outbreak of a streaky pattern at 120 cm fetch with $u_{*1} = 0.59 \frac{\text{cm}}{\text{s}} \Rightarrow l^{100} = 1.51\,\text{cm}$. For this wind condition, the FOV shows the critical fetch, where stable streaks (as in figure [7.4]) transition into a turbulent flow pattern.

conditions recorded with PRIM clearly show the footprints of turbulent near-surface processes (figure [7.7]).

One plausible explanation of why these fine structured turbulent eddies are not observed with the other methods given identical conditions, is that their tracer diffuse too fast to resolve it. Compared to the precipitate observed with PRIM, stronger convergence fields are necessary in order to keep regions of higher temperature or pH value together. Structures that evolve over the course of $\mathcal{O}(1\mathrm{s})$, as in figure [7.7], are therefore not observable.

Although the experiments are controlled for similar conditions in the important parameters of fetch and friction velocity, obtained differences could to some extend also be accounted for by the tunnels' distinct geometries.

Structure of Streaks

The convergence and divergence strength increases for higher wind speeds and similar structures are observed for $u_* > 0.6$. Figure [7.9] contrasts the four investigated visualization methods for near surface flow. Although the macroscopic tracer in figure [7.9d] also shows streaky structures, the observed pattern varies widely from the other techniques. This is however attributed to their size and the associated penetration depth and not to their Schmidt number. With a diameter of $\gtrsim 70\,\mu\mathrm{m}$ of the glass bubbles, the shear induced flow pattern is entirely different from what the PRIM tracer (size $\approx 1\,\mu\mathrm{m}$) observes much closer to the surface. The behaviour of these glass bubbles is analysed in detail in section 7.5 but is excluded from the further comparison in this section.

The statistics of the most pronounced streaks are observed to be similar across all visualization methods. Their lifetime as well as the streak spacing are in good agreement with each other, suggesting that, in fact, the same fundamental processes at the air-water interface are observed. The respective structure of the streaks differs significantly, though.

In IR images (figure [7.9a]), the most diverse patterns are observed. The low Prandtl number of $Pr = 7$ makes it possible for heat to spread much faster than gases ($Sc \approx 600$). Therefore, regions of high intensity appear blurry and further structure in between of the strongly pronounced streaks becomes apparent. Streaks in the fluorescence signal (figure [7.9b]) are more easily distinguishable due to the two orders of magnitude smaller diffusion coefficient. This effect is enhanced by

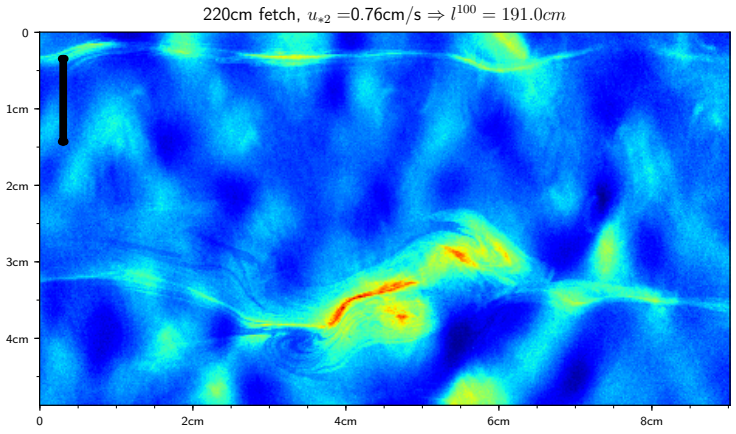

FIGURE 7.8: Streak with pronounced fine structure at 220 cm fetch with $u_{*2} = 0.76\,\frac{\mathrm{cm}}{\mathrm{s}} \Rightarrow l^{100} = 1.16\,\mathrm{cm}$

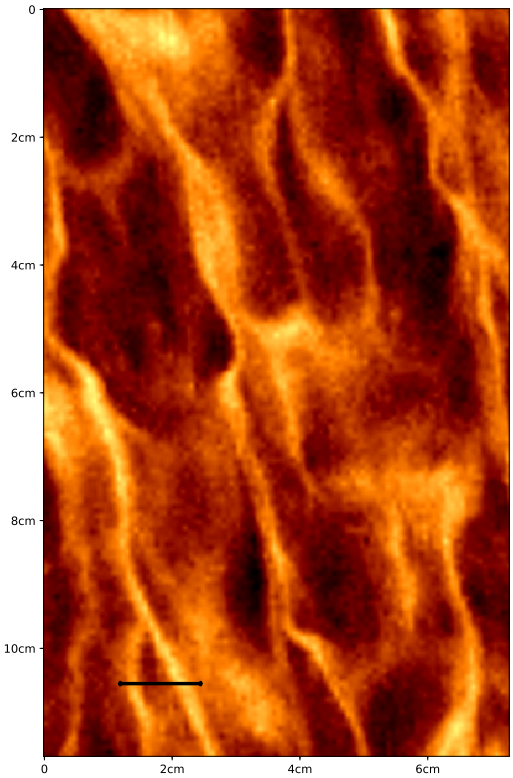

(A) Active Thermo., $u_* = 0.67\,\frac{\text{cm}}{\text{s}}$, 2 m fetch.

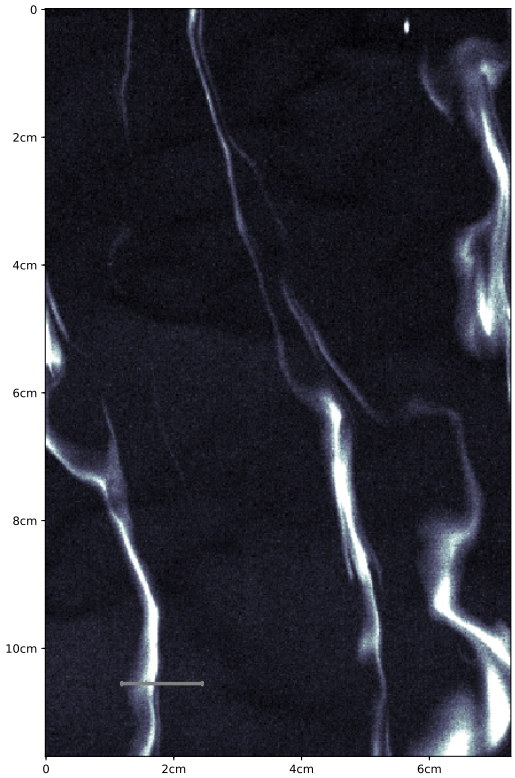

(B) BLI, , same condition as (A).

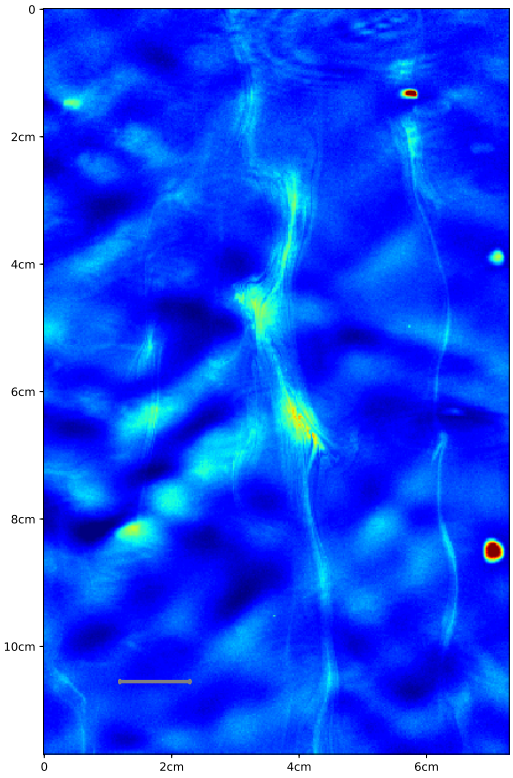

(C) PRIM, $u_{*2} = 0.76\,\frac{\text{cm}}{\text{s}}$, 220 cm fetch.

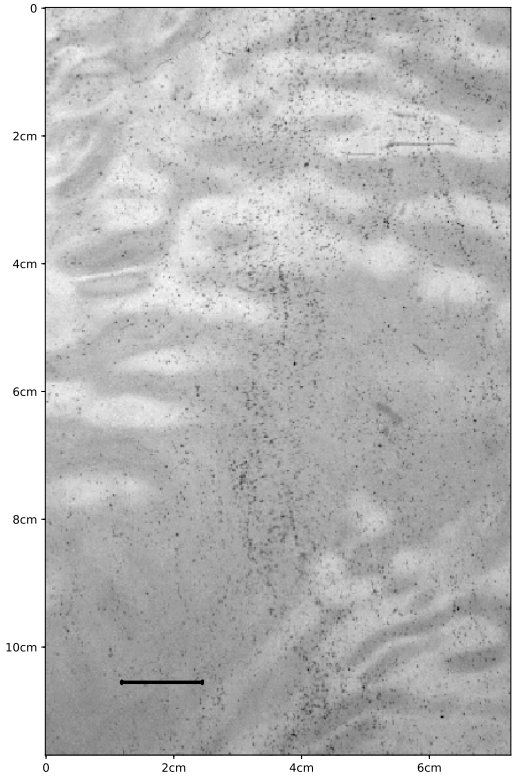

(D) Glass bubbles, $u_* = 0.67\,\frac{\text{cm}}{\text{s}}$, unlim. fetch.

FIGURE 7.9: Direct comparison of the visualization methods at similar conditions and sampled to the same FOV with same resolution. Wind blows from the bottom up.

the critical threshold for the pH value below that no fluorescence becomes apparent. In essence it acts like a step function, cutting off regions where the convergence is not strong enough to reach the needed pH value and truncating streaks so that they appear thinner than they really are.

The observed flow pattern in PRIM data is superimposed with the wave field due to experimental difficulties (cf. section 4.2). Aside from this, no structures are observed in between the clearly defined streaks. The Brownian motion of the particles is negligible by construction ($Sc \approx 10^6$, cf. section 2.3). With no other force acting on them, all tracer particles are observed to align in accordance with the strongest convergence field. In contrast to the naïve expectation, the most pronounced streaks in PRIM appear to be broader than in the other methods. This is related to the fine structure of the streaks that is already visible in figure [7.9c] but better investigated in figure [7.8] under the same conditions in higher resolution. It appears that pushing the tracer particles further together at the surface, forcing them to pile up, requires additional energy. This fine structure makes it therefore possible to resolve the convergence strength within a streak. The observed stability of fine lines is an additional indicator for the very low diffusivity of the tracer. It shows again that while the transport processes are fast on larger scales (turbulence) and efficient on the microscopic level (molecular diffusion), the mixing is very slow in the intermediate regime.

The qualitative comparison of the different visualization methods shows a clear evolution of the pattern with growing Schmidt number. Diffuse and "washed out" streaks in thermography images appear to be thinner and more organised in BLI data and are clearly separated and finely structured in PRIM. The tendency for the tracer to accumulate in regions of strong convergence clearly grows with the Schmidt number. Since no simultaneous measurements of PRIM together with one of the other visualization techniques was possible, a quantification of this effect is outside the scope of this work (cf. section 6.2.3).

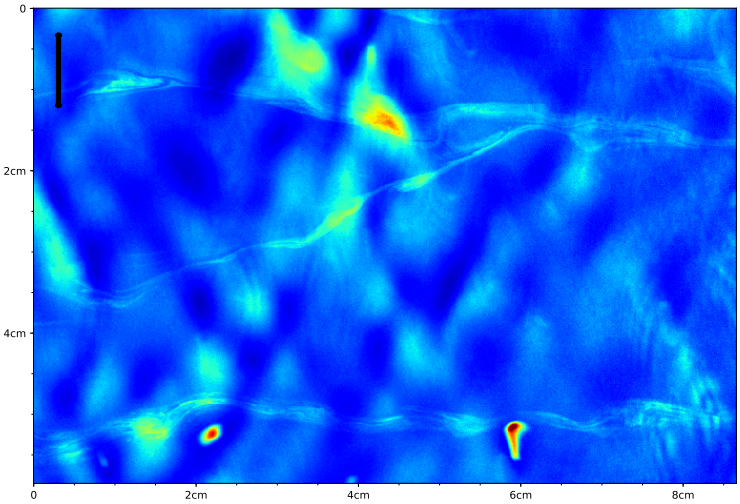

FIGURE 7.10: Typical downwind Y junction of two Langmuir streaks at $u_{*2} = 0.97\,\frac{\text{cm}}{\text{s}}$.

Streak Instabilities

With higher wind speeds, the wave field becomes more developed and the transport process is increasingly governed by the formation of Langmuir circulations

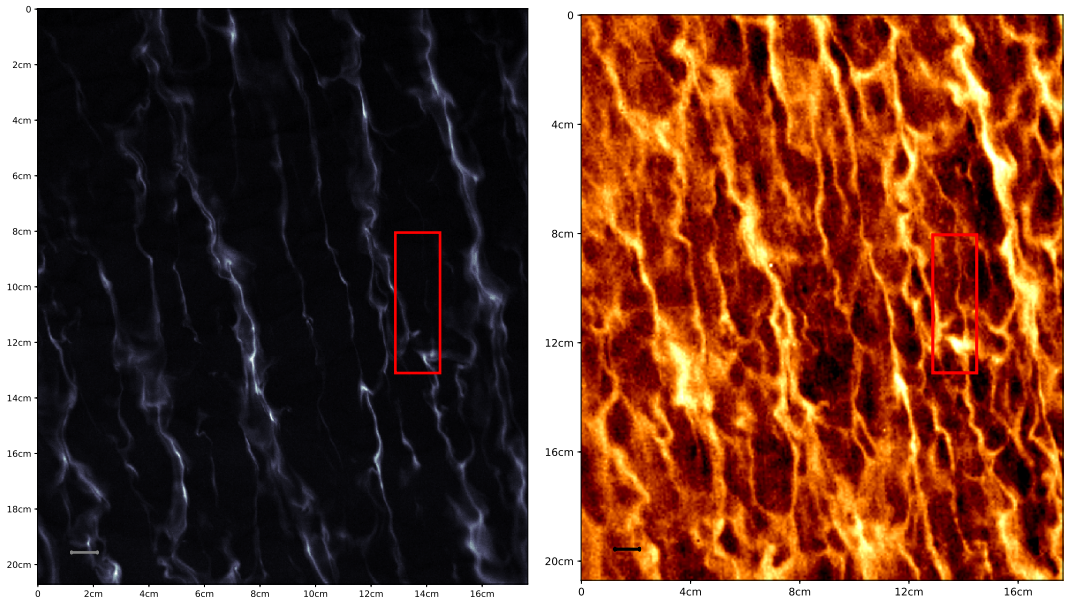

FIGURE 7.11: Streak pattern for BLI (*left*) and active thermography (*right*) with 2 m fetch and $u_* = 0.83 \frac{\text{cm}}{\text{s}}$ (bottom-up)

(cf. section 2.5.5). This is observed in the form of streaks with a much larger lifetime which remain persistent at the surface. The spacing of Langmuir circulations is larger than the theoretically expected streak spacing l^{100} since this scale also considers the smaller and short-living fish scales. A temporally constant pattern is however rarely observed. Streaks are found to merge and split up continuously rather than remaining parallel.

For micro Langmuir circulations, Y junctions appear analogously to the observations on larger scales in the field. Figure [7.10] shows one example that is in good agreement with the expected angle of 30° (cf. section 2.5.3). The streaks themselves maintain their structure while amalgamating into one. While this process was described on large scales by including effects of the Earth's rotation (Bhaskaran and Leibovich, 2002), no conceptual framework could be found to explain it under laboratory conditions.

Upwind Y junctions (i.e. open end towards higher fetch) are more often observed and result from the cleavage of streaks. Figure [7.11] shows the full FOV of the established methods BLI and active thermography. The dominant streaks in the images are observed to be persistent over time. An instability is however emerging in the framed region that causes this streak to split up and is shown over the course of 0.12 s in figure [7.12a] and [7.12b]. As suggested by numerical simulations (Tsai, 1998; Tsai and Liu, 2003), such an event is attributed to a horse shoe vortex bursting to the surface (cf. 2.5.4). This results in local upwelling, splitting the streak in two parts. The tracers follow the convergence zones caused by the emerged vortex lines. The resulting streak spacing is in good agreement with the l^{100} value. During this surface renewal event, the tracer concentration at the surface decreases over the consecutive frames as expected.

Figure [7.12c] shows a streak that becomes unstable in a region of strong convergence. Analogous to the observations described above, it is assumed to be caused by the emergence of a horse shoe vortex. It counteracts the influence of the Langmuir circulation and a large portion of the tracer particles are observed to be transported into the bulk. The result is an upwind Y junction, which is also being commonly

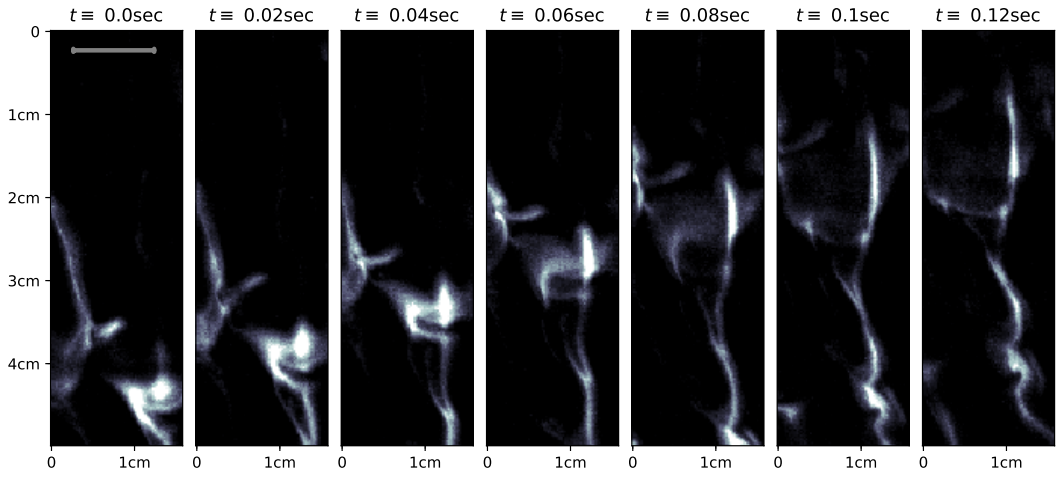

(A) Time evolution of the surface patch marked in figure [7.11] observed with BLI.

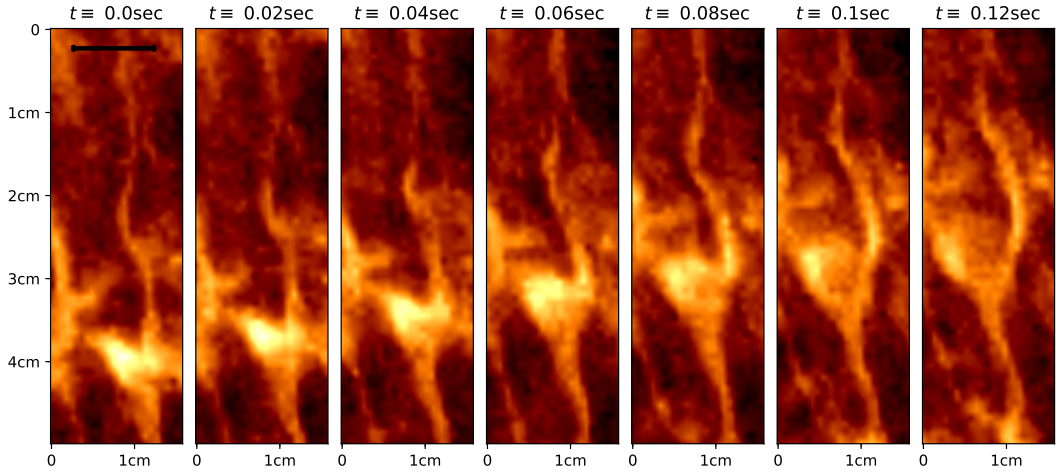

(B) Analogous to (A) with active thermography.

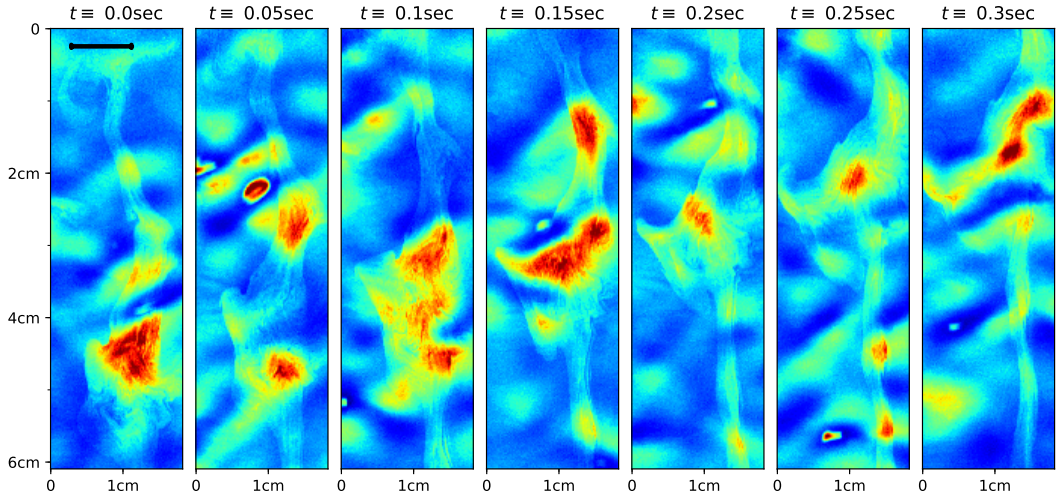

(C) Similar event observed with PRIM at 220 cm fetch, $u_{*2} = 0.97\ \frac{\text{cm}}{\text{s}}$

FIGURE 7.12: Separation of a streak for different tracers at similar conditions.

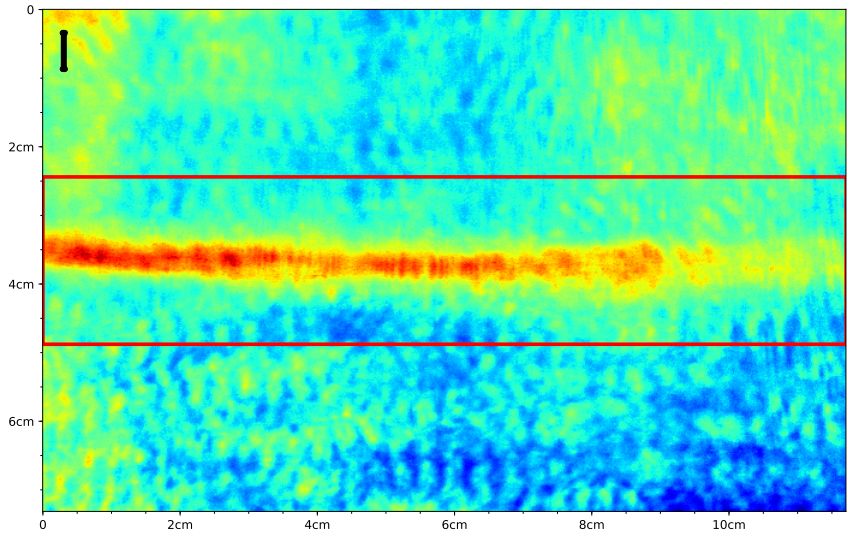

(A) Averaged image over 100 frames ($\widehat{=}$1 s)

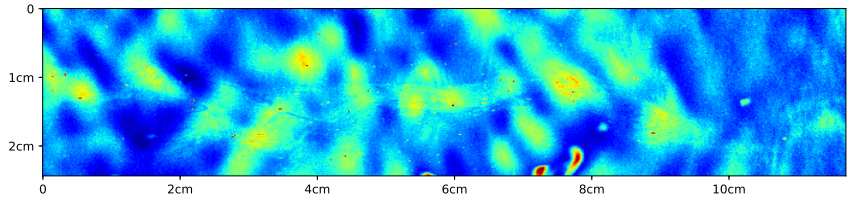

(B) Single frame showing the selected image section in (A)

FIGURE 7.13: Stable Langmuir streak at 220 cm fetch, $u_{*2} = 1.49\ \frac{\text{cm}}{\text{s}}$

observed in PRIM data.

Analysing such image data seems to be the most promising approach to determine the individual contributions of characteristic flow processes to air-water gas transfer. Quantitative analysis has so far only been done with thermal images (e.g. Lu, Tsai, and Jähne, unpub.) and conservative tracer methods (e.g. Turney, 2016). The qualitative analysis within the scope of this work suggests that PRIM provides a powerful tool to determine the convergence strength at the water surface.

7.4 Microscale Breaking

The growing influence of the surface curvature on the recorded PRIM data makes investigations in the high-wind regime, where microscale breaking events are expected, considerably harder. Figure [7.13] shows how difficult it becomes to distinguish streaks from the background when only single images are considered. While watching time series or averaging over many frames, streaks aligned in wind direction become however clearly visible. Aside from the dominant Langmuir streaks, the occurrence of small and fast moving dots is observed. It is not clear whether they are due to the same processes observed for very small wind speeds (cf. figure [7.1]) or of other origin, e.g. upwelling (bulk is not visible due to tartrazine, section 4.2.2) particle clusters.

Microscale breaking events are exclusively observed in gravity waves with parasitic capillaries, which is in agreement with previous investigations of thermal imagery (Jessup, Zappa, and Yeh, 1997). Growing shear stress leads to an accumulation of the tracer at the wave crest and the boundary layer is pushed together. The first

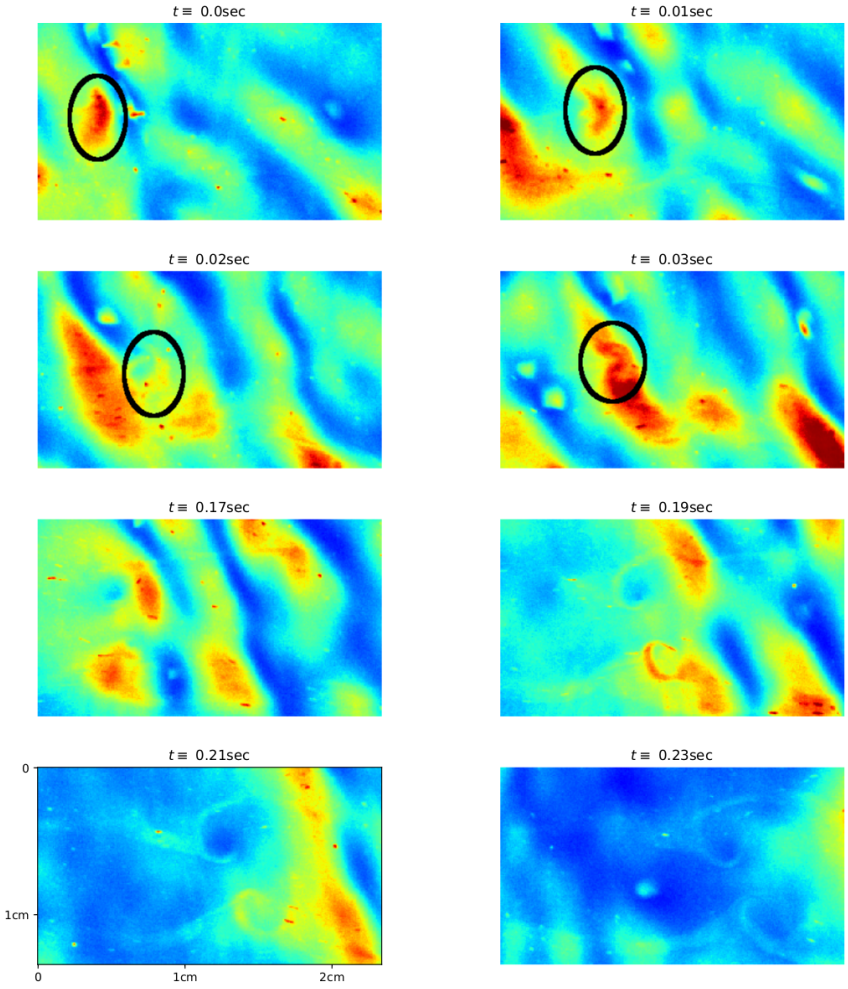

FIGURE 7.14: Temporal evolution of a single microscale breaking event at 220 cm fetch, $u_{*2} = 1.49\,\frac{\text{cm}}{\text{s}}$. Initial event is marked with black ellipsis.

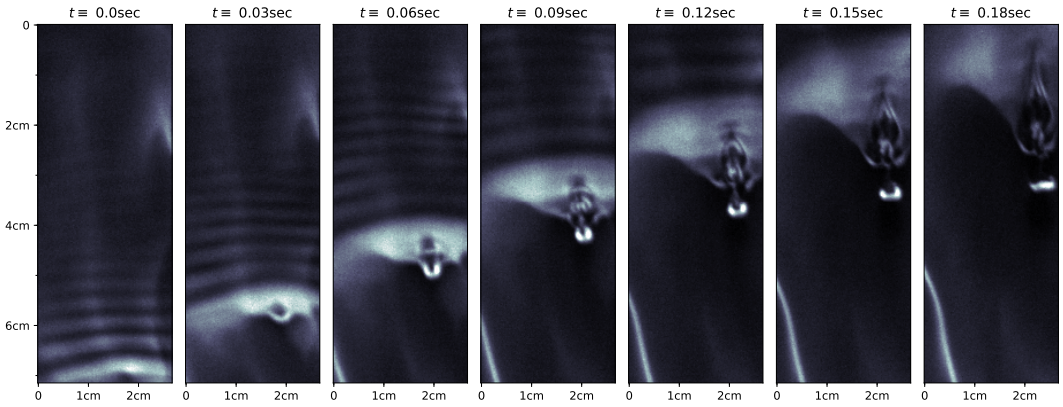

FIGURE 7.15: Time development of a small microscale breaking event observed with BLI at $u_* = 0.59\,\frac{\text{cm}}{\text{s}}$ (bottom-up) with unlimited fetch length.

image in figure [7.14] shows a small region forming a sharp edge. In the following, the shear stress exceeds a critical value and produces turbulent kinetic energy. Turbulent eddies form, renewing the surface and transporting the tracer from the wave crest into the water bulk. The wake of this event is shown by the last four images in figure [7.14]. Dark centres in the resulting eddies indicate that the surface is slightly concave in these regions. A small denting of the surface due to microscale breaking is confirmed by simultaneous BLI and slope (ISG) measurements in the *Aeolotron*.

This events describes a minimal example for a turbulently breaking wave crest. Usually, microscale breakers at larger fetch length with higher waves are investigated that result in the renewal of much larger surface patches[1]. Such minimal microscale breaking events are however also observed with BLI. Figure [7.15] shows the temporal evolution of an equally small wave crest. The boundary layer is pushed together analogously to the precipitate density and forms a sharp edge. When exceeding a critical value, the wave breaks and the surface is renewed. The footprints of the turbulent eddies are diffusing away faster and can therefore not be observed as clearly as with PRIM.

The frequency of microscale breaking events could not reliably be determined. Light refractions and lensing effects due to the wave field make it hard to investigate events at high wind speeds with PRIM. Right now, microscale breaking events only become apparent by careful observations and are even harder to detect with computer vision algorithms. If it is managed to further suppress the interfering signals, PRIM provides a sensitive tool to investigate all sorts of surface renewal events.

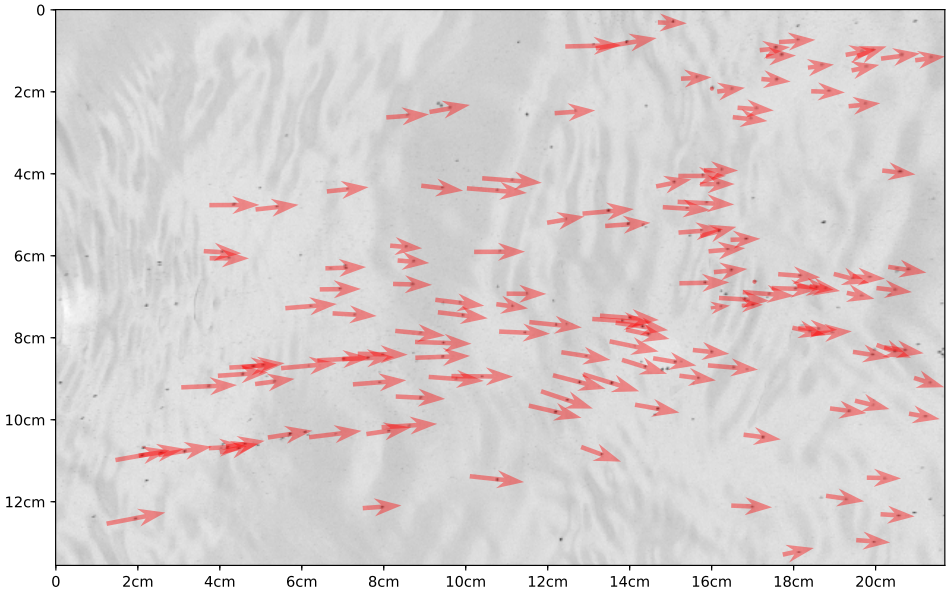

FIGURE 7.16: Calculated velocity vectors from filtered trajectories of 0.5 mm glass bubbles.

[1]There is actually no unanimous consensus in the literature on what surface patterns are already associated with the microscale breaking described in section 2.5.2. Recent and unpublished research by Angelika Klein however clearly classifies the here shown phenomenon as such events.

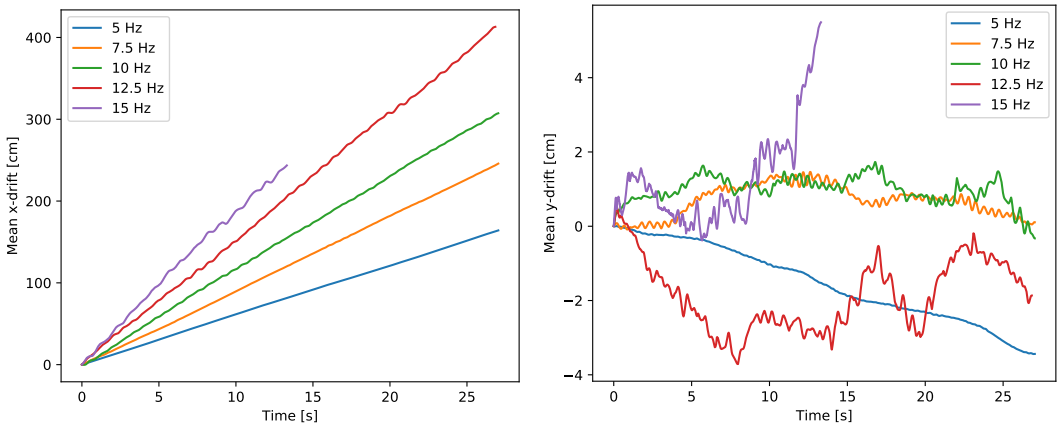

FIGURE 7.17: Plot of mean particle drift for 70 µm glass bubbles in x (*left*) and y direction (*right*) for different wind speeds. 15 Hz condition was measured with twice the frame rate.

7.5 Surface Velocity

Small glass bubbles were considered to expand the comparison in section 7.3 by a macroscopic tracer with $Sc \rightarrow \infty$. Even though streaky patterns are formed, the turbulent footprints were observed to differ vastly from the other visualization techniques. This provides evidence that the flow field strongly depends on the penetration depth in the viscous boundary layer. An additional contribution to the different observations might originate from interactions of the glass bubbles vertically to the wind direction. This counteracts the expectation towards a tracer with large Schmidt number of being highly sensitive to any surface convergence. Figure [7.16] and [7.9d] hence show –except for occasional streaky alignments– an almost homogeneous distribution on the water surface. The particles that are however aligned (e.g. lower left in figure [7.16]) appear to have a higher surface velocity. This is consistent with the theory of Langmuir circulations (cf. section 2.5.3) but a quantitative analysis of this effect is outside the scope of this thesis.

The motion in wind direction is not affected from potential interactions of the particles since no velocity gradient in x direction is present. This makes the glass bubbles a well suited tracer for the surface velocity. Due to the velocity gradient in the viscous boundary layer, the various sizes are expected to move with an velocity that has to be integrated over their penetration depth (cf. section 3.3).

The plots in figure [7.17] show the drift of the smallest glass spheres obtained with the tracking approach described in section 6.3. The drift between two frames is determined by averaging over all particles that passed the previously described filters. As expected, the particle movement in wind direction is linear with time. Fluctuations around the average velocity are due to waves and thus become more pronounced for higher wind speeds. The drift vertically to the wind direction is not used for the calculations but monitored for checking purposes. While a clear tendency to drift towards the outer wall is observed at slow wind, glass bubbles are more likely to go towards the inner wall for higher wind speeds. This is due to complex secondary flow patterns in the annular tank and has a significantly more pronounced effect on the glass bubbles with larger radius. For motor frequencies other than 10 Hz, the amount of bigger tracers within the FOV becomes too small until the flow reaches equilibrium.

TABLE 7.1: Expected and experimentally observed surface velocities for different experimental conditions.

Size	Freq. [Hz]	u_* [$\frac{cm}{s}$]	u_b [$\frac{cm}{s}$]	u_{surf}^{aTh} [$\frac{m}{s}$]	u_{surf}^{theo} [$\frac{cm}{s}$]	u_{surf}^{exp} [$\frac{cm}{s}$]
70 µm	5	0.25	1.69	5.65 ± 0.16	5.16±0.52	6.04±0.18
70 µm	7.5	0.38	2.74	8.4 ± 0.6[2]	8.38±0.84	9.13±0.27
70 µm	10	0.51	3.81	10.8 ± 1.1	11.67±1.17	11.44±0.34
70 µm	12.5	0.67	5.25	-	16.07±1.61	15.26±0.46
70 µm	15	0.83	6.67	-	20.39±2.04	18.05±0.90
$\sim$ 0.5 mm	10	0.51	3.81	10.8 ± 1.1	< 11.67	12.24±0.61
(1-2)mm	10	0.51	3.81	10.8 ± 1.1	< 11.67	11.32±0.57

Table [7.1] shows the results for the surface velocity. Values denoted with u_{surf}^{aTh} are used for comparison and were measured by Emmel (2017) with a technique based on active thermography. The theoretically expected surface velocities u_{surf}^{theo} are estimations based on the momentum balance in equation (2.31) with the geometry of the *Aeolotron* and the assumption of constant momentum resistance β. There is no experimental data available that quantifies to what extend the assumption of a constant β is valid. The error is hence estimated to be 10% of the predicted value. The calculation does not consider the additional contribution of the wind to the momentum balance in the form of "pushing" against waves. The influence of this so-called *form drag* increases with the growth of waves. Since its calculation assumes that all momentum is transferred via the viscous boundary layer, u_{surf}^{theo} overestimates the surface velocity systematically.

The experimentally determined surface velocities u_{surf}^{exp} are obtained by fitting a linear slope to the drift in wind direction.

The dominant error is expected to be due to a bias by filtering the particle trajectories. Different combinations of the parameters d, m, n, as described in section 6.3, were applied on each dataset to obtain a measure for the systematic differences. On this basis, the error for the surface velocities was estimated to be 3%. Since the statistics of the larger particle sizes and the 15 Hz wind conditions was considerably smaller, the error there is approximated with 5%.

Resulting values are systematically larger than the measurements with active thermography suggest. This technique is under active development and is currently assumed to underestimate the surface velocity due to various approximations (cf. Emmel, 2017, p. 32). Both methods lead to values that are significantly higher than expected for small wind speeds. This is explained by a notoriously higher u_* at segment 13 (not reliably determined since the modifications, cf. section 4.1.3) than the average that is used for the momentum balance. For intermediate wind conditions, the unquantified contribution of the form drag to the momentum balance outweighs the inhomogeneous wind conditions. Taking these effects into consideration, the experimental results are in good agreement with the expectation. Higher wind speeds could not be measured with this setup since glass bubbles are turbulently transported to the water bulk (cf. section 4.1.4).

Larger glass bubbles of various sizes were used in the attempt to determine the velocity gradient in the viscous boundary layer (cf. section 3.3). With larger diameter, their velocity should therefore decrease. Because of the vertical particle drift in the *Aeolotron*, a large enough statistic for particle trajectories could only be achieved

[2]Interpolated value between measurements for the conditions of 5 Hz, 6.3 Hz, 7.9 Hz and 10 Hz.

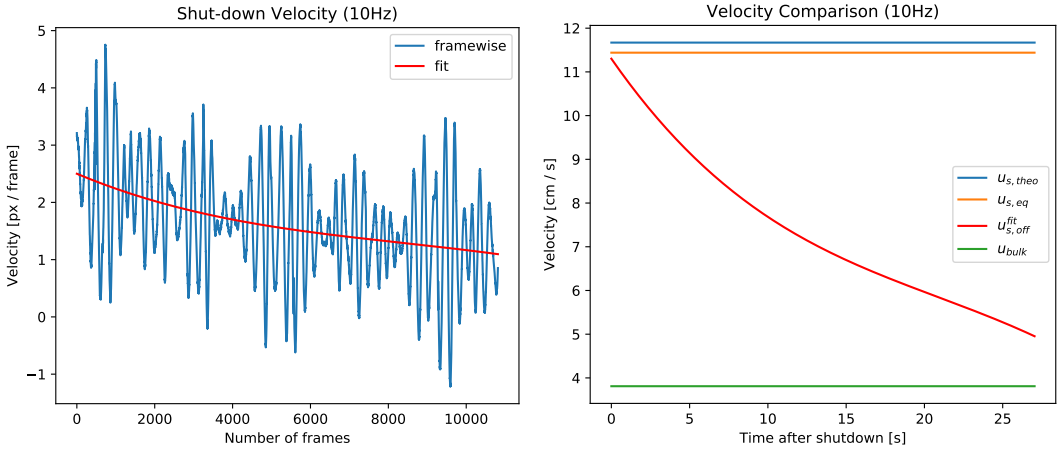

FIGURE 7.18: Development of the surface velocity after shut-down of the wind turbines (*left*) and its comparison to the equilibrium and bulk velocity (*right*) at 10 Hz.

for a motor frequency of 10 Hz. Against expectations, the obtained velocity turns out to be about the same as for the 70 µm glass spheres. Various effects can be thought of to have an influence on this result. One reason could be that the glass bubbles are not *fully* immersed in the water and therefore provide a direct target for the wind. The velocity gradient in the boundary layer could moreover cause the glass bubbles to rotate. A further analysis of this tracer's complex behaviour is beyond the scope of this thesis.

Additional measurements have been conducted right after turning off the wind turbines. With the shutdown of the wind forcing, the viscous boundary layer dissolves as described by Bopp (2014). The measuring time of 29 s is limited by the internal memory capacity of the high speed camera. Figure [7.18] shows that the surface velocity already decreases significantly within this time period. Starting close to u^{exp}_{surf}, it converges over time to the bulk velocity.

This preliminary result further encourages the use of 70 µm glass spheres as an inexpensive and easy to use tracer for the surface velocity. It provides a new experimental approach to investigate the wind induced forcing on the viscous boundary layer and can be used to determine the local friction velocity u_*.

Chapter 8

Conclusion and Outlook

Previous analysis shows that precipitation reaction imaging is a powerful technique to observe near-surface flow for air-sea interactions. Further improvements are however necessary to establish the method and make quantitative analysis possible. This chapter summarises the experimental results and suggests measures to further improve the quality of the obtained data.

8.1 Conclusion

A new two-dimensional imaging method has been developed which can be used to investigate gas transfer and the footprints of near-surface turbulence at the air-water interface. The underlying concept is a precipitation reaction of one reagent, present in excess in the water body, and the reaction partner introduced into the airspace. The reaction is controlled by the gas supply and leads to an accumulation of microscopic particles at the water surface. The precipitate at the surface is observable due to the scattering of light from a suitable illumination source.

Different chemical systems were tested to implement this idea. Experiments with CO_2 as air-sided reactant provide qualitative evidence for the slow reaction rate of CO_2 in water and its dependency on the pH value. Moreover, this makes the experimental conditions hard to control, which was also encountered during experimentation using SO_2. Best results were achieved using the chemical system with $AgNO_3$ in the water body and a controlled influx of HCl gas. The solubility product of the reaction, $K_{sp} = 1.77 \times 10^{-10}$, is sufficiently small and the salt AgCl precipitates. Due to a suitable choice of the reactants concentrations, the reaction takes place directly at the water surface. The diffusivity as well as the sedimentation speed of this tracer are found to be very low, leading to a high effective Schmidt number. The tracer therefore stays at the water surface and provides a sensitive indicator for convergence and divergence fields at the interface.

Only small concentrations of the gas can be used in order to avoid a sinkage of the reaction plane (cf. section 2.4). Analysing already small amounts of precipitate with a high spatial and temporal resolution, sets high demands on the experimental setup. During experiments at the *Heidelberg Linear Wind-Wave Tunnel* (cf. section 4.1.2) the individual components of the setup were optimized. The main experimental challenge arises from the fact that the scattered light from the tracer and reflections from the water surface have the same wavelength and polarization. Direct reflections can be avoided by the use of point-like illumination sources. A combination of two lasers with cylindrical lenses is used to provide a sufficiently strong and homogeneous illumination field (cf. section 4.2.1). They are triggered together with a fast and low-noise camera (cf. section 4.2.3), observing a surface patch of $(7.3 \times 11.7)\text{cm}^2$ with a spatial resolution of 61 µm and frame rate of 100 Hz.

The absorption dye tartrazine is necessary to block the influence that tracer particles present in the water bulk have on the image (cf. section 4.2.2).

The precipitation reaction imaging method (PRIM) was used for systematic laboratory experiments under a large range of environmental conditions. Measurements for eight different wind speeds, covering friction velocities from 0.21 $\frac{\text{cm}}{\text{s}}$ to 1.49 $\frac{\text{cm}}{\text{s}}$, were conducted simultaneously at two fetch lengths 120 cm and 220 cm. The observations are compared to provided data of active thermography (cf. section 3.1.1) and boundary layer imaging (cf. section 3.1.2) as well as to experiments with glass spheres as macroscopic flow tracers (cf. section 3.3). While all methods visualize the same underlying flow structures, their main difference is the Schmidt number of the respective tracer (cf. section 2.3). With $Sc = \mathcal{O}(10^6)$ for PRIM, the diffusivity of the tracer is negligible for all conditions compared to the surface flow. The method is therefore an excellent indicator for convergence strength with a much higher sensitivity than the established techniques.

This allows a detailed analysis of the formation and temporal evolution of shear induced surface patterns. A strong fetch dependency for the onset of specific flow mechanisms has been observed. For a given fetch, a higher friction velocity is found to increase the convergence strength and intensify the specific flow patterns. Footprints of Langmuir circulations and microscale breaking events in the associated characteristic regimes (cf. section 2.5.5) can also clearly be identified in the data.

Qualitative comparison of PRIM imagery with BLI and infrared images show a close resemblance between the flow patterns. With a higher Schmidt number however, observed streaks are more clearly separated and show a more pronounced structure (cf. section 7.3). Accumulations of the PRIM tracer show a fine structure, making it possible to resolve the convergence strength within a streak.

There remain however serious difficulties which emerge when using the PRIM technique with a growing wave field. Higher surface curvature leads to shadowing and lensing effects in the image data, making it harder to identify the tracer and the underlying turbulent footprints. Despite extensive investigation using various image processing techniques, the quality of the data could not be improved significantly (cf. section 6.2.3).

Macroscopic tracer particles ($Sc \to \infty$) are observed to to be not as sensitive to surface convergence due to their non-negligible penetration into the viscous boundary layer. They are however found to be a suitable tracer to determine the surface velocity. Results from a particle tracking approach are in good agreement with theoretical predictions and previous measurements (cf. section 7.5). This technique therefore provides a previously unused and easily applicable measure for the momentum transport and the influence of the wind induced shear stress on the viscous boundary layer. Furthermore, the macroscopic tracer can be used for detailed analysis of secondary flow patterns which play an important role in annular wind wave tunnels.

8.2 Outlook

The focus of this thesis was set on the development of the previously untried precipitation reaction imaging method and a more detailed quantitative evaluation of the obtained flow patterns is yet to be done. The qualitative analysis within the course of this work however already provides new insights in the formation of shear induced flow patterns. Quantifying these effects would provide a valuable contribution to our understanding of small scale air-sea interactions. PRIM provides a powerful tool to investigate the individual footprints of shear induced turbulence and the strong tendency of the tracer to accumulate in the most prominent convergence zone. This makes it easy to determine the dominant flow mechanism. With suitable calibration, the intensity, thickness and fine structure of the streaks can be used to determine the local convergence strength. This is expected to provide a reasonable lower bound for the local transfer velocity.

Difficulties however remain in the high wind regime where refraction light corrupts the tracer signal in the image data. Great effort has been done to overcome this issue but it was not possible to separate the tracer signal from the reflecting surface. Other methods in the visible spectrum like BLI and LIF use fluorescent tracers to overcome this issue. Although no suitable chemical system with a fluorescent precipitate could be found within the course of this work, it may be a subject to further investigation. The usage of (hyper-)spectral imaging provides a promising approach since it is commonly used to classify different materials (Chang, 2003). Moreover, simultaneous slope measurements of the investigated surface patch could possibly be used to exclude the contribution due to the surface curvature. It is however not clear how the presence of the precipitate would affect optical water wave measurements.

Simultaneous measurements of PRIM with active thermography are needed to quantify the observations in section 7.3. The chemical system of BLI and PRIM are not compatible in their current form since HCl affects the pH value. An idea would be to combine the methods, for example by using a fluorescent dye to visualize the acidification in the boundary layer due to HCl influx, analogous to the alkaline ammonia (cf. section 3.1.2). Measurements with PRIM in the *Aeolotron* were not feasible for practical reasons. With a water volume of 18 m^3 more than 3 kg of $AgNO_3$ would be necessary to reach the Ag^+ concentration that was used in the smaller facility. Environmental and financial factors considered, this experiment was outside the scope of this work.

PRIM is however expected to work well in annular facilities. While the tracer particles accumulate at the beach of a linear facility, an unlimited fetch would allow them to remain at the interface. Since the precipitate could accumulate at the water surface over time, this might allow for the usage of considerably lower concentrations of the reactants.

Further improvements to the chemical system could possibly be achieved by substituting HCl with hydrogen bromide (HBr). The reaction product silver bromide (AgBr) has an considerably lower solubility product of: $K_{sp} = 5.35 \times 10^{-13}$ (Haynes, 2016). A potential drawback could be the even higher photosensitivity of AgBr. This was however not found to be a problem within the course of this work.

Bibliography

Allan, Dan et al. (2015). *trackpy: Trackpy v0.3.0*. Full list of contributors: Aron Ahmadia, Continuum Analytics; François Boulogne, Princeton University; Rebecca Perry, Harvard University; Al Piszcz, The Mitre Corporation Jan Schulz, TU Freiberg; Leonardo Uieda, Universidade do Estado do Rio de Janeiro. DOI: 10.5281/zenodo.34028. URL: https://doi.org/10.5281/zenodo.34028.

Asher, W. E. and J. F. Pankow (1991). "Prediction of gas/water mass transport coefficients by a surface renewal model". In: *Environmental Science and Technology* 25.7, pp. 1294–1300. DOI: 10.1021/es00019a011.

Astarita, Giovanni, Attilio Bisio, and David W Savage (1983). *Gas treating with chemical solvents*. English. "A Wiley Interscience publication." New York : John Wiley. ISBN: 0471057681.

Banner, M. L. and W. L. Peirson (1998). "Tangential stress beneath wind-driven air-water interfaces". In: *Journal of Fluid Mechanics* 364, pp. 115–145. DOI: 10.1017/S0022112098001128.

Banner, M. L. and O. M. Phillips (1974). "On the incipient breaking of small-scale waves". In: *Journal of Fluid Mechanics* 65, pp. 647–656. DOI: 10.1017/S0022112074001583.

Bhaskaran, R. and S. Leibovich (2002). "Eulerian and Lagrangian Langmuir circulation patterns". In: *Physics of Fluids* 14, pp. 2557–2571.

Bock, E. J. et al. (1999). "Relationship between air-sea gas transfer and short wind waves". In: *Journal of Geophysical Research* 104.C11. J NOV 15, pp. 25821–25831. ISSN: 0148-0227. DOI: 10.1029/1999JC900200.

Bopp, Maximilian (2014). "Luft- und wasserseitige Strömungsverhältnisse im ringförmigen Heidelberger Wind-Wellen-Kanal (Aeolotron)". Master's thesis. Institut für Umweltphysik, Universität Heidelberg, Germany. DOI: 10.11588/heidok.00017151.

Campbell, J. A. and T. J. Hanratty (1983). "Mechanism of turbulent mass transfer at a solid boundary". In: *AIChE Journal* 29.2, pp. 221–229. ISSN: 1547-5905. DOI: 10.1002/aic.690290208. URL: http://dx.doi.org/10.1002/aic.690290208.

Caulliez, G. (1998). "The generation of the first visible wind waves". In: *Physics Fluids* 10.4, pp. 757–759.

Chang, Chein-I (2003). *Hyperspectral imaging: techniques for spectral detection and classification*. Vol. 1. Springer Science & Business Media.

Clegg, S.L. and P. Brimblecombe (1986). "The dissociation constant and henry's law constant of HCl in aqueous solution". In: *Atmospheric Environment (1967)* 20.12, pp. 2483 –2485. ISSN: 0004-6981. DOI: https://doi.org/10.1016/0004-6981(86)90079-X. URL: http://www.sciencedirect.com/science/article/pii/000469818690079X.

Crocker, John C. and David G. Grier (1996). "Methods of Digital Video Microscopy for Colloidal Studies". In: *Journal of Colloid and Interface Science* 179.1, pp. 298 – 310. ISSN: 0021-9797. DOI: https://doi.org/10.1006/jcis.1996.0217. URL: http://www.sciencedirect.com/science/article/pii/S0021979796902179.

Csanady, G. T. (1990). "The role of breaking wavelets in air-sea gas transfer". In: *Journal of Geophysical Research* 95.C1, pp. 749–759. DOI: 10.1029/JC095iC01p00749.

Cussler, E. L. (2009). *Diffusion - Mass Transfer in Fluid Systems*. 3rd ed. Cambridge: Cambridge University Press.

Deacon, E. L. (1977). "Gas transfer to and across an air-water interface". In: *Tellus* 29, pp. 363–374. DOI: 10.3402/tellusa.v29i4.11368.

Degreif, K. (2006). "Untersuchungen zum Gasaustausch - Entwicklung und Applikation eines zeitlich aufgelösten Massenbilanzverfahrens". Dissertation. Institut für Umweltphysik, Fakultät für Physik und Astronomie, Univ. Heidelberg. URL: http://www.ub.uni-heidelberg.de/archiv/6120.

Ebuchi, N., H. Kawamura, and Y. Toba (1987). "Fine structure of laboratory wind-wave surfaces using an optical method." In: *Boundary LayerMeterology* 39, p. 133.

Einstein, A. (1905). "Über die von der molekularkinetischen Theorie der Wärme geforderte Bewegung von in ruhenden Flüssigkeiten suspendierten Teilchen". In: *Annalen der Physik* 322.8, pp. 549–560. DOI: 10.1002/andp.19053220806.

Emmel, Arne (2017). "Bestimmung der Geschwindigkeit und des Geschwindeigkeitsgradienten an der windgetriebenen Wasseroberfläche". Master's thesis. Institut für Umweltphysik, Fakultät für Physik und Astronomie, Univ. Heidelberg.

Engelmann, D. et al. (1999). "Particle-tracking velocimetry". In: *Handbook of Computer Vision and Applications*. Ed. by B. Jähne, H. HauSSecker, and P. GeiSSler. Vol. 3: Systems and Applications. Academic Press. Chap. 31, pp. 663–697.

Fairall, C. W. et al. (1996). "Cool-skin and warm-layer effects on sea surface temperature". In: *Journal of Geophysical Research* 101.C1, pp. 1295–1308. DOI: 10.1029/95JC03190.

Farmer, D. and M. Li (1995). "Patterns of Bubble Clouds organized by Langmuir Circulation". In: *Journal of Physical Oceanography* 25, pp. 1426–1440. DOI: 10.1175/1520-0485(1995)025.

Fick, A. E. (1855). "Über Diffusion". In: *Annalen der Physik* 170, pp. 59–86. DOI: 10.1002/andp.18551700105.

Flothow, Leonie (2017). "Bubble characteristics from breaking waves in fresh water and simulated seawater". MA thesis. Institut für Umweltphysik, Fakultät für Physik und Astronomie, Univ. Heidelberg. DOI: 10.11588/heidok.00023754.

Friedl, Felix (2013). "Investigating the Transfer of Oxygen at the Wavy Air-Water Interface under Wind-Induced Turbulence". Dissertation. Institut für Umweltphysik, Fakultät für Physik und Astronomie, Univ. Heidelberg. URL: http://www.ub.uni-heidelberg.de/archiv/14582.

Garbe, C. S. (2001). "Measuring Heat Exchange Processes at the Air–Water Interface from Thermographic Image Sequence Analysis". Dissertation. Heidelberg, Germany: IWR, Fakultät für Physik und Astronomie, Univ. Heidelberg. URL: http://www.ub.uni-heidelberg.de/archiv/1875.

Garbe, C. S., H. Spies, and B. Jähne (2003). "Estimation of surface flow and net heat flux from infrared image sequences". In: *Journal of Mathematical Imaging and Vision* 19.3, pp. 159–174. DOI: 10.1023/A:1026233919766.

Garbe, C. S. et al. (2014). "Transfer across the air-sea interface". In: *Ocean-Atmosphere Interactions of Gases and Particles*. Ed. by Peter S. Liss and Martin T. Johnson. Springer, pp. 55–112. DOI: 10.1007/978-3-642-25643-1_2.

Garrett, C. and J. Smith (1976). "On the Interaction Between Long and Short Surface Waves". In: *Journal of Physical Oceanography* 6, pp. 925–930.

Gilleo, M. A. (1953). "Photoemission from Silver into AgCl, KBr, NaCl, and New Bands of Photosensitivity in AgCl". In: *Phys. Rev.* 91 (3), pp. 534–542. DOI: 10.1103/PhysRev.91.534. URL: https://link.aps.org/doi/10.1103/PhysRev.91.534.

Grassl, H. (1976). "The dependence of the measured cool skin of the ocean on wind stress and total heat flux". In: *Boundary Layer Meterology* 10, pp. 465–474. DOI: 10.1007/BF00225865.

Handler, R. A., I. Savelyev, and M. Lindsey (2012). "Infrared imagery of streak formation in a breaking wave". In: *Phys. Fluids* 24. DOI: 10.1063/1.4769459.

Handler, R. A., G. B. Smith, and R. I. Leighton (2001). "The thermal structure of an air–water interface at low wind speeds". In: *Tellus* 53, pp. 233–244. DOI: 10.1034/j.1600-0870.2001.00158.x.

Harriott, P. (1962). "A random eddy modification of the penetration theory". In: *Chem. Eng. Sci.* 17, pp. 149–154. DOI: 10.1016/0009-2509(62)80026-8.

Haynes, W.M. (2016). *CRC Handbook of Chemistry and Physics, 97th Edition*. CRC Press. ISBN: 9781498754293.

Herzog, Alexandra (2010). "Imaging of Water-sided Gas-Concentration Fields at a Wind-Driven, Wavy Air-Water Interface". Dissertation. Institut für Umweltphysik, Fakultät für Physik und Astronomie, Univ. Heidelberg. URL: http://www.ub.uni-heidelberg.de/archiv/11220.

Hiby, J. W. (1968). "Eine Fluoreszenzmethode zur Untersuchung des Transportmechanismus bei der Gasabsorption im Rieselfilm". In: *Wärme und Stoffübertragung* 1, pp. 105–116. DOI: 10.1007/BF00750793.

Hiby, J. W., D. Braun, and K. H. Eickel (1967). "Eine Fluoreszenzmethode zur Untersuchung des Stoffübergangs bei der Gasabsorption im Rieselfilm". In: *Chemie-Ing. Techn.* 39, pp. 297–301. DOI: 10.1002/cite.330390517.

Higbie, R. (1935). "The rate of absorption of a pure gas into a still liquid during short periods of exposure". In: *Trans. Am. Inst. Chem. Eng.* 31, pp. 365–389.

Huhn, Florian (2008). "A Simple Instrument for the Measurement of the Slope and Height Distributions of Small Scale Wind-Driven Water Waves". Diplomarbeit. Institute for Environmental Physics, University of Heidelberg.

Jessup, A. T., C. J. Zappa, and H. H. Yeh (1997). "Defining and quantifying microscale wave breaking with infrared imagery". In: *Journal of Geophysical Research* 102.C10, pp. 23145–23153. DOI: 10.1029/97JC01449.

Jessup, A T et al. (1997). "Infrared remote sensing of breaking waves". In: *Nature* 385.6611, pp. 52–55. DOI: 10.1038/385052a0.

Jähne, B. (1980). "Zur Parametrisierung des Gasaustauschs mit Hilfe von Laborexperimenten". IUP D-145, Link Nationalbibliothek http://d-nb.info/810123614. Dissertation. Institut für Umweltphysik, Fakultät für Physik und Astronomie, Univ. Heidelberg. DOI: 10.5281/zenodo.10443. URL: http://www.ub.uni-heidelberg.de/archiv/16796.

— (1986). "Bildfolgenanalyse in der Umweltphysik: Wasseroberflächenwellen und Gasaustausch zwischen Atmosphäre und Gewässern". In: *Proc. 8. DAGM-Symposium Mustererkennung 1986*. Informatik-Fachberichte 125. DAGM award. Berlin, pp. 201–205. DOI: 10.1007/978-3-642-71387-3_36. URL: http://www.ub.uni-heidelberg.de/archiv/18103.

Jähne, B. and H. Haussecker (1998). "Air-water gas exchange". In: *Ann. Rev. Fluid Mech.* 30, pp. 443–468. DOI: 10.1146/annurev.fluid.30.1.443.

Jähne, B., G. Heinz, and W. Dietrich (1987). "Measurement of the diffusion coefficients of sparingly soluble gases in water". In: *Journal of Geophysical Research* 92.C10, pp. 10,767–10,776. DOI: 10.1029/JC092iC10p10767.

Jähne, B. et al. (1987). "On the parameters influencing air-water gas exchange". In: *Journal of Geophysical Research* 92, pp. 1937–1950. DOI: 10.1029/JC092iC02p01937.

Jähne, B. et al. (1989). "Investigating the transfer process across the free aqueous boundary layer by the controlled flux method". In: *Tellus* 41B.2, pp. 177–195. DOI: 10.1111/j.1600-0889.1989.tb00135.x.

Jähne, B. et al. (2007). "The influence of intermittency on air/water gas transfer measurements". In: *Transport at the Air Sea Interface — Measurements, Models and Parameterizations*. Ed. by C. S. Garbe, R. A. Handler, and B. Jähne. Springer-Verlag. DOI: 10.1007/978-3-540-36906-6_18.

Jähne, Bernd (1983a). *Messung des Gasaustausches und der Turbulenz an der Oberfläche durch Sichtbarmachung der Grenzschicht*. Technical Report. Institut für Umweltphysik, Universität Heidelberg. DOI: 10.5281/zenodo.12201.

— (1983b). "Optical water waves measuring techniques". In: *Talk, 1st International Symposium on Gas Transfer at Water Surfaces, Cornell University, Ithaca, New York, June 13–15, 1983*. DOI: 10.5281/zenodo.14008.

— (1985). "Transfer processes across the free water interface". IUP D-200. Habilitation thesis. Institut für Umweltphysik, Fakultät für Physik und Astronomie, Univ. Heidelberg. DOI: 10.5281/zenodo.12202. URL: http://www.ub.uni-heidelberg.de/archiv/16798.

Kern, D. M. (1960). "The Hydration of Carbon Dioxide". In: *Journal of Chemical Education* 37, pp. 14–23. DOI: 10.1021/ed037p14.

Kiefhaber, D. et al. (2014). "High-speed imaging of short wind waves by shape from refraction". In: *J. Europ. Opt. Soc. Rap.* 9, p. 14015. DOI: 10.2971/jeos.2014.14015.

Kolmogorov, A. N. (1941). "The local structure of turbulence in compressible turbulence for very large Reynolds numbers". In: *Compt.Rend.Akad.Nauk SSSR* 30, p. 301.

— (1962). "A refinement of previous hypotheses concerning the local structure of turbulence in a viscous incompressible fluid at high reynolds number". In: *Journal of Fluid Mechanics* 13, pp. 82–85. DOI: 10.1017/S0022112062000518.

Krah, Nils (2014). "Visualization of air and water-sided concentration profiles in laboratory gas exchange experiments". Dissertation. Institut für Umweltphysik, Fakultät für Physik und Astronomie, Univ. Heidelberg. URL: http://www.ub.uni-heidelberg.de/archiv/16895.

Krall, Kerstin Ellen (2013). "Laboratory Investigations of Air-Sea Gas Transfer under a Wide Range of Water Surface Conditions". Dissertation. Institut für Umweltphysik, Fakultät für Physik und Astronomie, Univ. Heidelberg. URL: http://www.ub.uni-heidelberg.de/archiv/14392.

Kropp, Marvin (2015). "Untersuchung des Wärmetransfers an der Wasseroberfläche in Abhängigkeit von der Wirklänge des Windes (Fetch) am Heidelberger Aeolotron". Bachelor thesis. Institut für Umweltphysik, Fakultät für Physik und Astronomie, Univ. Heidelberg.

Kräuter, C. et al. (2014). "High resolution 2-D fluorescence imaging of the mass boundary layer thickness at free water surfaces". In: *J. Europ. Opt. Soc. Rap.* 9, p. 14016. DOI: 10.2971/jeos.2014.14016.

Kräuter, Christine (2015). "Visualization of air-water gas exchange". Dissertation. Institut für Umweltphysik, Fakultät für Physik und Astronomie, Univ. Heidelberg. URL: http://www.ub.uni-heidelberg.de/archiv/18209.

Kubo, R (1966). "The fluctuation-dissipation theorem". In: *Reports on Progress in Physics* 29.1, p. 255. URL: http://stacks.iop.org/0034-4885/29/i=1/a=306.

Kundu, P. K. (2008). *Fluid Mechanics*. 4th. San Diego, CA: Academic Press, Elsevier.

Kunz, Jakob (2017). "Active Thermography as a Tool for the Estimation of Air-Water Transfer Velocities". PhD thesis. Institut für Umweltphysik, Fakultät für Physik und Astronomie, Univ. Heidelberg. DOI: 10.11588/heidok.00022903.

Langmuir (1938). "Surface Motion of Water Induced By Wind". In: *Science* 87, pp. 119–124.

Le Quéré, Corinne et al. (2017). "Global carbon budget 2017". In: *Earth System Science Data Discussions*, pp. 1–79. ISSN: 1866-3591. DOI: 10.5194/essd-2017-123. URL: http://mfkp.org/INRMM/article/14477849.

Leibovich, S. (1983). "The form and dynamics of langmuir circulations". In: *Ann. Rev. Fluid Mech.* 15, pp. 391–427.

Libbrecht, Kenneth George (2016). *Ken Libbrecht's field guide to snowflakes*. Voyageur Press.

Liss, P. S. and P. G. Slater (1974). "Flux of gases across the air-sea interface". In: *Nature* 247, pp. 181–184. DOI: 10.1038/247181a0.

Lu, Guan-hung, Wu-ting Tsai, and Bernd Jähne (unpub.). "Decomposing thermal images at a wind-driven, wavy surface for quantitative separation into characteristic flow processes". In: *unpublished*.

Maslowska, J and J Janiak (1996). "Voltammetric and Spectrosphotometric Studies on Tartrazine - a Food Colorant". In: *Chemia analityczna* 41.5, pp. 855–864.

McCready, M. J., E. Vassiliadou, and T. J. Hanratty (1986). "Computer simulation of turbulent mass transfer at a mobile interface". In: *AIChE Journal* 32, pp. 1108–1115. DOI: 10.1002/aic.690320707.

Melville, W. K. (1996). "The role of surface-wave breaking in air-sea interaction." In: *Ann. Rev. Fluid Mech.* 28, p. 279.

Melville, W. K., R. Shear, and F. Veron (1998). "Laboratory measurements of the generation and evolution of Langmuir circulations". In: *Journal of Fluid Mechanics* 364, pp. 31–58. DOI: 10.1017/S0022112098001098.

Mischler, Wolfgang, Kerstin E. Krall, and Bernd Jähne (2015). "Experimental studies of the parameters controlling bubble-induced air-sea gas exchange". In: *7th International Symposium on Gas Transfer at Water Surfaces, Seattle, May 18–21, 2015*. abstract, accepted as poster. DOI: 10.5281/zenodo.17671.

Möller, U. and G. Schumann (1970). "Mechanisms of Transport from the Atmosphere to the Earth's Surface". In: *Journal of Geophysical Research* 75, pp. 3013–3019. DOI: 10.1029/JC075i015p03013.

Münsterer, T. and B. Jähne (1998). "LIF measurements of concentration profiles in the aqueous mass boundary layer". In: *Experiments in Fluids* 25, pp. 190–196. DOI: 10.1007/s003480050223.

Münsterer, T., H. J. Mayer, and B. Jähne (1995). "Dual-tracer measurements of concentration profiles in the aqueous mass boundary layer". In: *Air-water Gas Transfer, Selected Papers from the Third International Symposium on Air–Water Gas Transfer*. Ed. by B. Jähne and E. C. Monahan. Hanau: AEON, pp. 637–648. DOI: 10.5281/zenodo.10406.

Nagel, Leila (2014). "Active Thermography to Investigate Small-Scale Air-Water Transport Processes in the Laboratory and the Field". Dissertation. Institut für Umweltphysik, Fakultät für Chemie und Geowissenschaften, Univ. Heidelberg. URL: http://www.ub.uni-heidelberg.de/archiv/16831.

Pearson, K. (1905). "The problem of the random walk". In: *Nature* 72.294. URL: http://www.nature.com/physics/looking-back/pearson/index.html.

Peirson, W. L. (1997). "Measurement of surface velocities and shears at a wavy air-water interface using particle image velocimetry." In: *Experiments in Fluids* 23, pp. 427–437.

Peirson, W. L. and M. L. Banner (2003). "Aqueous surface layer flows induced by microscale breaking wind waves". In: *Journal of Fluid Mechanics* 479, pp. 1–38. DOI: 10.1017/S0022112002003336.

Peirson, William L., James W. Walker, and Michael L. Banner (2014). "On the microphysical behaviour of wind-forced water surfaces and consequent re-aeration". In: *Journal of Fluid Mechanics* 743, pp. 399–447. DOI: 10.1017/jfm.2013.681.

Platt, Tanja (2011). "Weiterentwicklung einer hochauflösenden LIF-Methode zur Messung von Sauerstoffkonzentrationsprofilen in der wasserseitigen Grenzschicht". started 11.04.2011. Bachelor thesis. Institut für Umweltphysik, Fakultät für Physik und Astronomie, Univ. Heidelberg.

Pope, S. B. (2009). *Turbulent Flows*. 6th ed. Cambridge University Press.

Prandtl, L. (1957). *Strömungslehre*. Vieweg.

Rashidi, M. and S. Banerjee (1990). "The effect of boundary conditions and shear rate on streak formation and breakdown in turbulent channel flows". In: *Phys. Fluids* 2, pp. 1827–1838. DOI: 10.1063/1.857656.

Reichardt, H. (1951). "Vollständige Darstellung der turbulenten Geschwindigkeitsverteilung in glatten Leitungen". In: *Zeitschrift für angewandte Mathematik und Mechanik* 31, pp. 208–219.

Rhein, M. et al. (2013). "Observations: Ocean". In: *Climate Change 2013: The Physical Science Basis. Contribution of Working Group I to the Fifth Assessment Report of the Intergovernmental Panel on Climate Change*. Ed. by T.F. Stocker et al. Cambridge, United Kingdom and New York, NY, USA: Cambridge University Press. Chap. 3, 255316. ISBN: ISBN 978-1-107-66182-0. DOI: 10.1017/CBO9781107415324.010. URL: www.climatechange2013.org.

Richter, K. (2009). *Technische Daten des Aeolotron nach dem Umbau 2007/2008*. Tech. rep. AG Bildverarbeitung Interdisziplinäres Zentrum für Wissenschaftliches Rechnen und Institut für Umweltphysik, Universität Heidelberg.

Rocholz, Roland et al. (2011). "Combined visualization of wind waves and water surface temperature". In: *Gas Transfer at Water Surfaces 2010*. Ed. by S. Komori, W. McGillis, and R. Kurose, pp. 496–506. DOI: 10.5281/zenodo.14957. URL: http://hdl.handle.net/2433/156156.

Roedel, Walter (2000). *Physik unserer Umwelt: die Atmosphäre*. 3rd ed. Springer-Verlag. URL: http://books.google.com/books?id=SD7p-lYBJQcC.

Sander, R. (2015). "Compilation of Henry's law constants (version 4.0) for water as solvent". In: *Atmospheric Chemistry and Physics* 15.8, pp. 4399–4981. DOI: 10.5194/acp-15-4399-2015. URL: https://www.atmos-chem-phys.net/15/4399/2015/.

Saunders, P. M. (1967). "The temperature at the ocean-air interface". In: *Journal of Atmospherical Sciences* 24.3, pp. 269–273. DOI: 10.1175/1520-0469(1967)024<0269:TTATOA>2.0.CO;2.

Schimpf, U. (2000). "Untersuchung des Gasaustausches und der Mikroturbulenz an der Meeresoberfläche mittels Thermographie". Dissertation. Heidelberg, Germany: Institut für Umweltphysik, Fakultät für Physik und Astronomie, Univ. Heidelberg. URL: http://www.ub.uni-heidelberg.de/archiv/545.

Schimpf, U., C. Garbe, and B. Jähne (2004). "Investigation of transport processes across the sea surface microlayer by infrared imagery". In: *Journal of Geophysical Research* 109.C8, C08S13. ISSN: 0148-0227. DOI: 10.1029/2003JC001803.

Schimpf, Uwe, Leila Nagel, and Bernd Jähne (2011). "The 2009 SOPRAN active thermography pilot experiment in the Baltic Sea". In: *Gas Transfer at Water Surfaces 2010*. Ed. by S. Komori, W. McGillis, and R. Kurose, pp. 358–367. DOI: 10.5281/zenodo.14956. URL: http://hdl.handle.net/2433/156156.

Schnieders, J. et al. (2013). "Analyzing the footprints of near surface aqueous turbulence - an image processing based approach". In: *Journal of Geophysical Research* 118, pp. 1272–1286. DOI: 10.1002/jgrc.20102.

Scott, Nicholas V, Robert A Handler, and Geoffrey B Smith (2008). "Wavelet analysis of the surface temperature field at an air–water interface subject to moderate wind stress". In: *International Journal of Heat and Fluid Flow* 29.4, pp. 1103–1112. DOI: 10.1016/j.ijheatfluidflow.2007.11.002.

Shaw, Dudley A. and Thomas J. Hanratty (1977). "Turbulent mass transfer rates to a wall for large Schmidt numbers". In: *AIChE J.* 23, pp. 28–37. DOI: 10.1002/aic.690230106.

Sommer, Christoph et al. (2011). "Ilastik: Interactive learning and segmentation toolkit". In: *Biomedical Imaging: From Nano to Macro, 2011 IEEE International Symposium on*. IEEE, pp. 230–233.

Stokes, G. G. (1847). "On the theory of oscillatory waves". In: *Trans. Camb. Philos. Soc.* 8, p. 441.

Thorpe, S. A. (2004). "Langmuir Circulation". In: *Ann. Rev. Fluid Mech.* 36.1, pp. 55–79.

Trofimova, Darya (2015). "Towards Four Dimensional Visualization of Air-Water Gas Exchange". Dissertation. Institut für Umweltphysik, Fakultät für Physik und Astronomie, Univ. Heidelberg. URL: http://www.ub.uni-heidelberg.de/archiv/19066.

Tsai, W.-T. (1998). "A numerical study of the evolution and structure of a turbulent shear layer under a free surface". In: *Journal of Fluid Mechanics* 354, pp. 239–276.

— (2007). "Using Numerical Simulation to Help Understand Transport Processes at the Air-Sea Interface".

Tsai, W.-T., S.-M. Chen, and C.-H. Moeng (2005). "A numerical study on the evolution and structure of a stress-driven, free-surface turbulent shear flow". In: *Journal of Fluid Mechanics* 545, pp. 163–192. DOI: 10.1017/S0022112005007044.

Tsai, W. T. and K. K. Liu (2003). "An assessment of the effect of sea surface surfactant on global atmosphere-ocean CO_2 flux". In: *Journal of Geophysical Research* 108, pp. 3127–3142. DOI: 10.1029/2000JC000740.

Tsai, W.-T. et al. (2013). "Characteristics of interfacial signatures on a wind-driven gravity-capillary wave". In: *Journal of Geophysical Research* 118, pp. 1715–1735. DOI: 10.1002/jgrc.20145.

Turney, D. E. (2016). "Coherent motions and time scales that control heat and mass transfer at wind-swept water surfaces". In: *Journal of Geophysical Research: Oceans* 121.12, pp. 8731–8748. ISSN: 2169-9291. DOI: 10.1002/2016JC012139. URL: http://dx.doi.org/10.1002/2016JC012139.

Turney, Damon E. and Sanjoy Banerjee (2013). "Air-water gas transfer and near-surface motions". In: *Journal of Fluid Mechanics* 733, pp. 588–624. DOI: 10.1017/jfm.2013.435.

Veron, F. and W. K. Melville (2001). "Experiments on the stability and transition of wind-driven water surfaces". In: *Journal of Fluid Mechanics* 446, pp. 25–65. DOI: 10.1017/S0022112001005638.

Veron, Fabrice, W Kendall Melville, and Luc Lenain (2011). "The Effects of Small-Scale Turbulence on Air-Sea Heat Flux". In: *Journal of Physical Oceanography* 41.1, pp. 205–220. DOI: 10.1175/2010JPO4491.1.

Warken, Pius (2010). "Hochauflösende LIF-Methode zur Messung von Sauerstoffkonzentrationsprofilen in der wasserseitigen Grenzschicht". Diplomarbeit. Institut für Umweltphysik, Fakultät für Physik und Astronomie, Univ. Heidelberg.

Whitman, W. G. (1923). "The two-film theory of gas absorption". In: *Chemical and Metallurgical Engineering* 29.4, pp. 146–148.

Wiberg, N, E Wiberg, and AF Holleman (2007). *Lehrbuch der anorganischen Chemie, 102. ed*.

Williams, Richard M (1982). "A model for the dry deposition of particles to natural water surfaces". In: *Atmospheric Environment (1967)* 16.8, pp. 1933–1938. DOI: 10.1016/0004-6981(82)90464-4.

Winter, Rene (2011). "Fluorescent Tracers for air-sided Concentration Profile Measurements at the Air-Water Interface". Dissertation. Institut für Umweltphysik, Fakultät für Physik und Astronomie, Univ. Heidelberg. URL: http://www.ub.uni-heidelberg.de/archiv/12105.

Woolf, D. K. and E. C. Monahan (1993). "Bubbles and the air-sea transfer velocity of gases". In: *Atmosphere-Ocean* 31, pp. 517–540. DOI: 10.1080/07055900.1993.9649484.

Yaglom, A. M. and B. A. Kader (1974). "Heat and mass transfer between a rough wall and turbulent fluid flow at high Reynolds and Peclet numbers". In: *Journal of Fluid Mechanics* 62, pp. 601–623. DOI: c.

Yang, Chao, Zengyou He, and Weichuan Yu (2009). "Comparison of public peak detection algorithms for MALDI mass spectrometry data analysis". In: *BMC Bioinformatics* 10.1, p. 4. ISSN: 1471-2105. DOI: 10.1186/1471-2105-10-4. URL: https://doi.org/10.1186/1471-2105-10-4.

Zappa, C. J., W. E. Asher, and A. T. Jessup (2001). "Microscale wave breaking and air-water gas transfer". In: *Journal of Geophysical Research* 106.C5, pp. 9385–9391. DOI: 10.1029/2000JC000262.

Appendix A

Spectroscopic Analysis of Tracer Particles

Studies of the tracer particles under a scanning electron microscope were possible thanks to the support of NIKON Metrology. The histograms show the quantity of specific elements obtained by the energy spectrum of the scattered electrons at the denoted pixel.

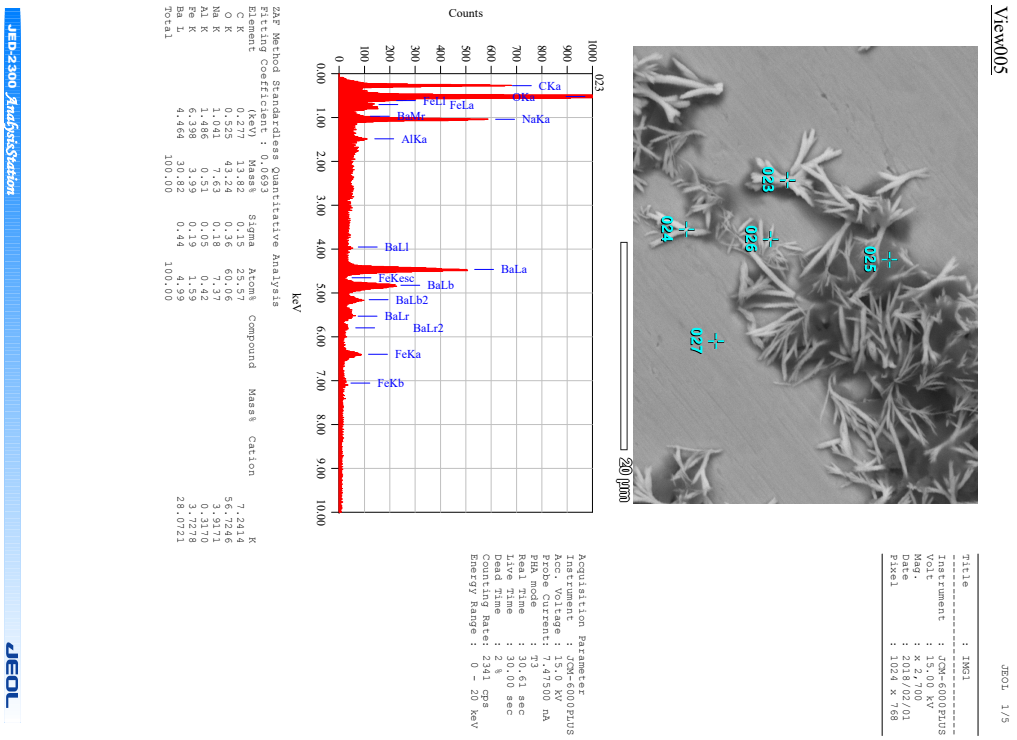

FIGURE A.1: $BaCO_3$

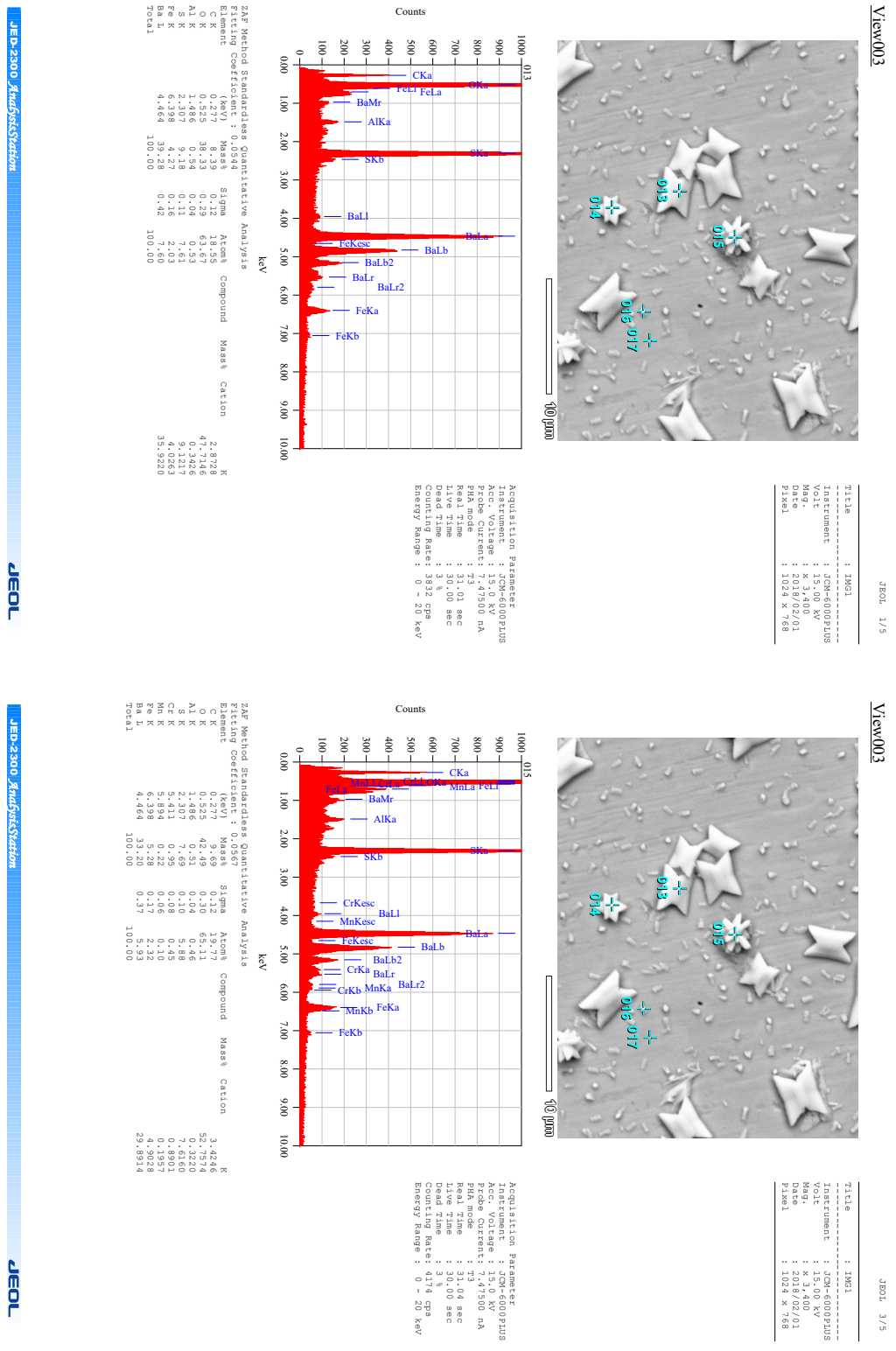

FIGURE A.2: $BaSO_3$

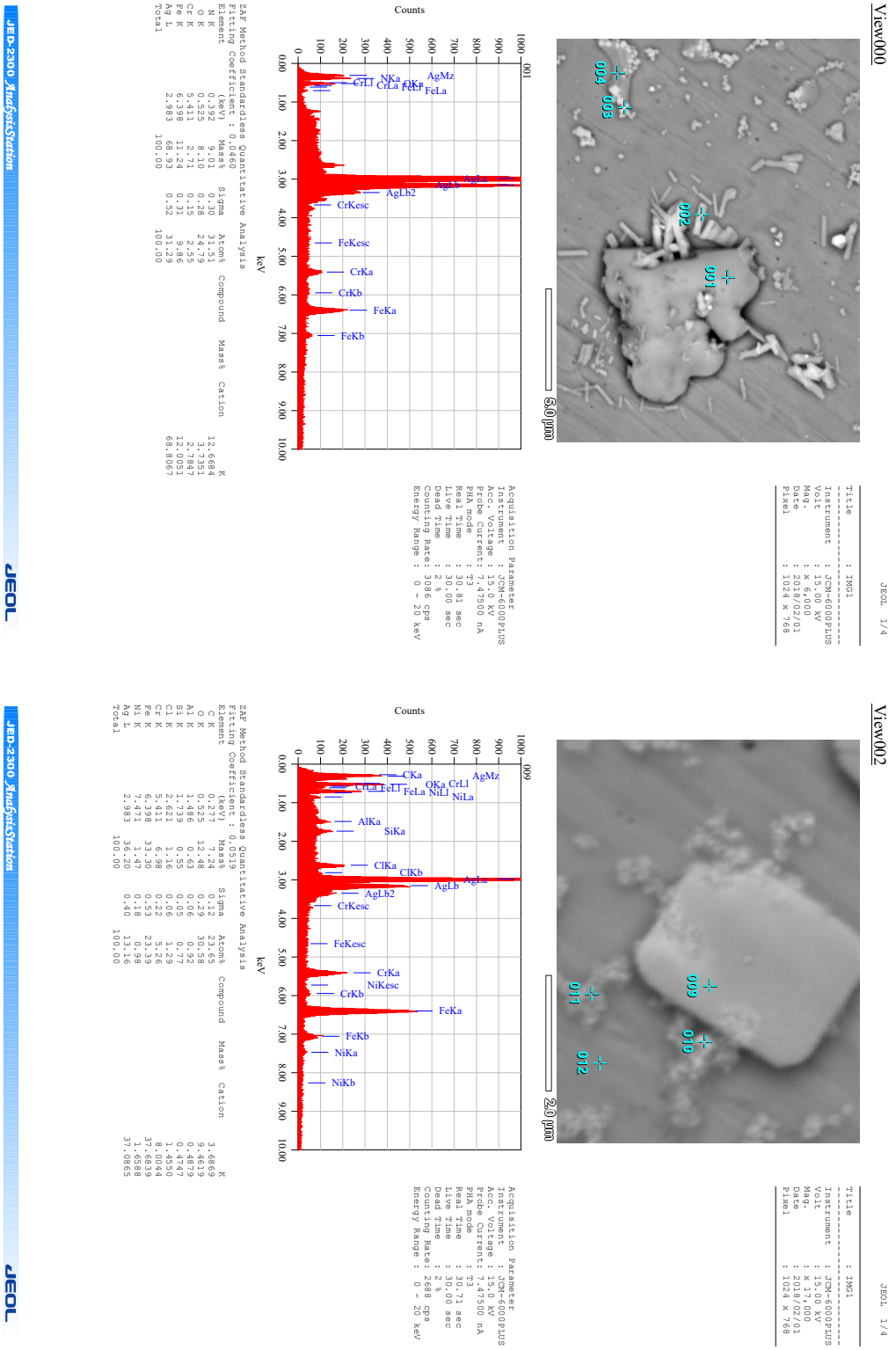

FIGURE A.3: AgCl

Acknowledgements

First of all, I want to give many thanks to Prof. Dr. Bernd Jähne who kindly offered me this interesting and truly interdisciplinary project at the intersection of environmental physics and image processing. His work ethics and wealth of ideas were a big motivation throughout the time I spent in his working group. Especially, I appreciate the numerously opportunities for advanced training in form of the multiple *Heidelberger Bildverarbeitungsforen*, the *European Machine Vision Forum* and schooling in image processing and sensors.

Special thanks is due to PD Dr. Ullrich Köthe for his willingness to act as referee and his keen interest in the topic of small-scale air-sea interactions.

Of course, many thanks goes to the whole *windis*-group for making the time in the lab passing way to fast. In particular, I want to thank Sonja Frieman for her active support, Angelika Klein for kindly providing streak data and the fruitful discussions about it, Max Bopp for his unfailing support with any kind of hardware and beautiful explanatory drawings, Dr. Kerstin Krall for her guidance in the lab and her abilities as a human library, and Dr. Günther Balschbach for the as enjoyable as constructive lunch&coffee breaks (and his mother for the generous cake supply).

I also (kind of) want to thank my beloved friends who did their best in trying to convince me to stay in Heidelberg for one semester more – but eventually still supported me in writing this thesis.

Erklärung:

Ich versichere, dass ich diese Arbeit selbstständig verfasst habe und keine anderen als die angegebenen Quellen und Hilfsmittel benutzt habe.

Heidelberg, den 28.03.2018 .....